ABSTRACT

MUKHOPADHYAY, ROUNAK. Development of Autonomous Truss Modules Utilizing Shape Memory Alloys for Actuation/Sensing Functionalities. (Under the direction of Dr. Fuh-Gwo Yuan).

Shape Memory Alloys (SMAs) inherently show a unique thermo-mechanical behavior that can be used in a variety of engineering applications. SMAs have been verified as actuators in multiple disciplinary fields and also show promise as strain and temperature sensors. Although SMAs have already been proven as effective actuators and sensors, the novel SMA mechanism designed in this study will be a multifunctional agent capable of providing both actuation and sensing to validate an autonomous truss module. The broad range of temperatures that SMAs can operate in allow the alloys to be used in extreme environments such as space. The integration of SMAs into a novel autonomous truss module for space structures is inspired by the Persistent Asset (PA) paradigm. The PA paradigm aims to eliminate waste in space missions and allows for a cheaper and more efficient alternative to the single launch and single use method. In this study, the aspects of the PA paradigm that are represented by the novel SMA truss modules are modularity, minimization of parasitic mass, and autonomy. SMAs aid in achieving these goals by providing a single source of autonomous actuation and self-sensing that replaces massive and voluminous alternatives on each module, thus reducing mass and volume across the entire PA. The structure of a PA's unit truss modules is based on previous studies that have narrowed down specific designs to two main truss geometries. This study will explore both geometries, but focus on a single geometry to validate the concept. The specific SMA that is used in this study is Nitinol which is the most commonly used commercial SMA due to its strong Shape Memory Effect (SME), good processibility, and excellent mechanical properties. The Nitinol will be actuated using Joule heating by a Pulse-Width Modulated (PWM) current, which will be

controlled using the SMA's intrinsic temperature sensing capabilities. This paper will explore the basis of the PA paradigm, the properties and compositions of different SMAs, the capabilities of SMAs in both actuator and sensing applications, the development of packaging and deployment concepts for unit truss modules, and finally will introduce validation tests designed to characterize the Nitinol and prove the multifunctional use of a novel SMA mechanism in an autonomous truss module.

Development of Autonomous Truss Modules Utilizing Shape Memory Alloys for Actuation/Sensing Functionalities.

by
Rounak Mukhopadhyay

A thesis submitted to the Graduate Faculty of
North Carolina State University
in partial fulfillment of the
requirements for the degree of
Master of Science

Aerospace Engineering

Raleigh, North Carolina
2020

APPROVED BY:

_____	_____
Dr. Fuh-Gwo Yuan Committee Chair	Dr. William R. Doggett External Member
_____	_____
Dr. Matthew Bryant	Dr. Jingyan Dong

DEDICATION

I dedicate this thesis to my friends and family who never stop believing in me.

BIOGRAPHY

Rounak Mukhopadhyay was born in Houston, Texas to Sangeeta Bhattacharya and Krishnendu Mukhopadhyay. He moved multiple times until his family settled in New Jersey. After high school, he pursued a degree in Aerospace Engineering at the University of Maryland, College Park. He graduated with a Bachelor's in Aerospace Engineering in May of 2017 and a few weeks later began as an intern at NASA Langley Research Center (LaRC). He continued his work at NASA LaRC as a contractor and began pursuing a Master of Science degree at North Carolina State University, Raleigh in 2018.

ACKNOWLEDGMENTS

I would like to thank Dr. Fuh-Gwo Yuan for his guidance through my time at North Carolina State University. He has supported and mentored me since the moment that I reached out with an interest to be under his tutelage.

I would like to thank Dr. William R. Doggett for being my mentor during my time at NASA LaRC. Dr. Doggett has always pushed me to reach for greater heights and showed me how to think like an engineer.

I would like to thank the many peers I have interacted with during my time at NASA LaRC. We have invested our blood and sweat into our projects, and my passion for our work is the same passion I see in each and every one of them.

My special thanks to my family and friends who supported me while I worked on my classes and thesis, and gave me a multiple homes on my many trips between North Carolina, Virginia, and New Jersey. Their love and belief in me is the reason I strive to be better every day.

TABLE OF CONTENTS

LIST OF TABLES

LIST OF FIGURES

CHAPTER 1: Motivation and Objective

The current paradigm for space mission launches is to design the mission to the payload fairing being used so that all the components can be sent up as a complete package in a single launch. The use of a single launch puts constraints on the mass and volume of the mission which can limit the performance of the tools being used. For example, the Hubble Space Telescope (HST) was launched in 1990 on the Space Shuttle Discovery. The telescope itself was held within the space shuttle, and therefore had to meet the interior volume constraints. The next generation and successor for the HST is the James Webb Space Telescope (JWST) which is currently planned to launch in 2021. The JSWT will be packaged in a single launch configuration, which means the space telescope will fit within a payload fairing with a maximum 4.57 meter static diameter and length of 16.19 meters ("The Launch – Webb/NASA", n.d.). The primary mirror on JWST has a diameter of 6.5 meters, while HST had a primary diameter of 2.4 meters ("Comparison: Webb vs Hubble, n.d.). In order to fit this large mirror within the Ariane 5 rocket, the engineers working on JSWT devised a clever packaging method for the primary mirror to be folded within the payload fairing. Even if the most optimal packaging technique and the largest payload fairing available are used, there is still a volume and mass constraint on any space telescope, satellite, spacecraft, etc. for a single launch mission that limits the size and potential for future space missions.

One proposed solution to this problem is to use modular building blocks that are sent up on multiple launches to create Persistent Assets (PAs) in situ using robotics aids in order to build the mission to whatever size is necessary. These modular building blocks come in the form of trusses which repeat their geometry within the finished structure, to create persistent platforms on which large space structures can be built. These modular building blocks will be validated and

produced in batches on Earth, which will reduce their development cost and time as more are built, and then efficiently packaged within a payload fairing using novel deployment methods to send large batches of modules into space on frequent and inexpensive commercial launch vehicles (Doggett et al., 2018). The recent success of SpaceX's repeated Falcon 9 rocket launches is a great motivator for this new proposed paradigm of space mission launches because the reuse of rockets allows for launch costs to be decreased.

The use of robotic aids in deployment has been utilized since the Space Shuttle era, and for the deployment of these modular trusses and construction of PAs, robotic arms will be employed to forgo the need for human interaction. An alternative method of deployment for the modular trusses is to use a class of material called Shape Memory Alloys (SMAs) which have a unique thermo-mechanical coupling that can be applied to deploy the trusses without the need of motors. SMAs have been tested and applied in space flight applications as deployment methods and have also been used as sensors for structural health monitoring. The utilization of SMAs will be more thoroughly reviewed later in this paper.

1.1 Persistent Asset Overview

A PA is defined as "any zero-g or planetary surface system that benefits from in-space assembly (ISA) or multiple visits for servicing, repairs, and upgrades." The PA term is derived from the term "persistent platform" which was used by the Defense Advanced Research Projects Agency (DARPA) in their vision for a geosynchronous Earth orbiting platform. PA's have been proposed for use as telecommunication platforms, Earth observing science platforms, Department of Defense (DOD) platforms, scientific telescope systems, and planetary surface systems that can include human outposts, science stations, and in-situ resource utilization systems. As opposed to the current state of the art, which involves a single unit launched and

operated without any further physical intervention, the PA paradigm is defined by the following attributes:

- Provides rapid emplacement of capabilities followed by planned upgrades and enhancement
- Benefits from multiple visits
- Can be anywhere in space including zero-G or planetary surfaces
- Incorporates modular systems and connectors
- Enables modules to be integrated and tested prior to launch
- Modules can be assembled, serviced, repaired, exchanged, etc.
- Emphasizes robotic interactions as opposed to crew interactions
- Modular components are launch vehicle agnostic
- Space operations make use of a standard toolbox of technologies, capabilities, and infrastructure tools
- Modules can be reused for multiple missions

The new paradigm involves the simplification and standardization of parts which allows a single or group of modules to adapt to a multitude of mission specifications. These standardized modular structures will remain competitive within the in-space industry due to their ability to be reconfigured and augmented to allow for rapidly changing customer specifications over a long lifetime, thus the term ‘persistent’ which is used to emphasize the longevity of the structures and systems. Due to the nature of ISA, the modular components can be optimized for packaging within multiple launches without sacrificing operational constraints on their final location in-situ. The aforementioned system attributes are possible due to the new commercial launch capabilities which allow for frequent and inexpensive launches, the emergence of robotic integration into

commercial spacecraft which enables frequent servicing missions, and advances in electronics and autonomous systems which allow robotics to perform reliably for a longer period of time (Dogget et al., 2018).

Table 1.1: Persistent Asset Attributes of Current Missions (Doggett et al., 2018).

Persistent Asset Attribute	Example Mission		
	International Space Station	**Hubble Space Telescope**	**James Webb Space Telescope**
1) Provides rapid emplacement of capabilities followed by planned upgrades and enhancements	√	√	
2) Benefits from multiple visits	√	√	
3) May be located anywhere in space			
4) Incorporates modular systems and connectors	√	√	
5) Modules are full integrated and tested on the ground before launch	√	√	
6) Modules can be assembled, serviced, repaired, exchanged, etc	√	√	
7) Emphasis is placed on robotics, as opposed to crew, interactions			
8) Modular components are launch-vehicle agnostic allowing multiple launch vehicle options	Initial assembly required Space Shuttle.		
9) Space operations make use of a standard toolbox of technologies, capabilities and infrastructure	√		
10) Modules reused in multiple missions			

The International Space Station (ISS), HST, and JSWT are a few examples of large space systems that could be accomplished using a PA approach. Table 1.1 shows each mission and their applicability to the aforementioned PA attributes. It can be seen that the ISS and HST both have a few PA attributes, however they required astronaut assistance for assembly and repair due to the available technology, and thus were locked to LEO for accessibility and mission specifications. JWST has no PA attributes and is dependent on both launch and deployment to be fully successful otherwise the mission is a failure. All three missions are single mission systems and were not designed to be modular to the degree that they can be repurposed for future missions. The ISS will eventually be deorbited like other outdated satellites have been in the past, however some satellites are pushed into a graveyard orbit where they are out of the path of

current operational orbits. Both of these methods keep valuable materials from being reused for future missions. The PA paradigm will focus on recycling components from missions which will ultimately minimize the waste in orbit around our planet.

A key feature of the PA paradigm is the modularity of the components. Modularity is used to simplify PA design by using common features and interfaces to create units that are not mission specific, that reduce overall mission risk, that allow for replacement on the ground and in-situ, and that enable reconfiguration of units and augmentation of systems through the substitution of present modules with newer modules that incorporate different or improved functionalities. Since these modules will be created in batches, as they are standardized the associated costs with design, development, and manufacturing will drop with each iteration. In order to maximize the benefits of modularity, any spacecraft system that will be assembled and revisited should be modularized including structure, power, propulsion, communication, etc. (Doggett et al., 2018). These systems can be modularized by inserting the existing technology within a structural module with a predefined geometry to create a unit that when combined with similar units will provide the resources needed for the specific mission. An example of a power module could be a solar panel array attached to a truss unit that when combined, through standardized connections with the necessary number of similar units, provides the proper power for the mission specifications.

Another important feature of the PA paradigm is the incorporation of autonomous robotic agents; autonomous to increase efficiency and robotic to eliminate the need for in-situ crewed operations. Currently crewed operations are limited to low Earth orbit (LEO) mainly in the ISS, whereas robotic capabilities are advancing in both LEO and geostationary orbit (GEO). The robotic agents used for ISA can vary from semi-stationary jigs that assist in aligning and

assembling structures to fully mobile arms that can traverse the assembly space to provide actuation where necessary. The most common archetype of space robotic agents are the arms such as Canadarm and its derivations, which were used on the Space Shuttles as the Shuttle Remote Manipulator System (SRMS) and on the International Space Station (ISS) within the Mobile Servicing System (MSS). In past and current space applications, the Canadarm was and is used to aid astronauts in assembly, however the future goal of ISA of PA's is to create an autonomous robotic system with zero human interaction.

The PA paradigm makes major changes to traditional spaceflight requirements that change the driving factors for design. Using frequent and inexpensive launches means the typical payload fairing mass and volume restrictions are not as important and the design can focus more on mission cost, risk, and test time. The modularization of the spacecraft provides more efficient packaging schemes which will minimize the effect of launch loads on the structure, thus allowing for more optimization for zero-G loads. If the PA is used as a base for a system that requires high stability and precision, such as a large-area telescope, the stiffness of the support structure will be a driving factor for design. In order to meet the structural requirements, verification and validation of the structure will be necessary. Onboard metrology will be used to monitor and measure structural parameters of the spacecraft; the performance parameters will be verified using pre-launch predictions, and the verification will occur during both assembly and operation. In order to confirm the structural parameters are set during operation, onboard systems will be used to monitor structural health as well as spacecraft and hosted payload system health. The structural health sensors will warn when strain measurements fall outside the nominal values which will signify if repair or replacement of the modular elements is necessary (Doggett et al., 2018).

A fundamental feature of incorporating modularity in a design is the minimization of parasitic mass, volume, and power requirements on the whole system. These parasitic components normally result from features that are used to support on-orbit operations that are not required for the specified mission of the spacecraft. These components can be deployment mechanisms and aids, grapple points, active vision targets, etc. (Doggett et al., 2018). For example, any feature that is added to aid in deployment and packaging on one module will have its mass multiplied by the total number of modules necessary for the full system. This also applies to the modular structure as well, so a lightweight truss is a viable solution for minimizing the mass of both the module and, multiplicatively, the entire system.

The ISA lab at NASA Langley Research Center (LaRC) has been focusing on two truss geometries as potential modular building blocks for the PA's. The two truss geometries are referred to as the Tri-Truss and the Cubic Truss and can be seen in Figure 1.1. The preliminary prototypes of these trusses were created using aluminum tubes and joints, however the final designs will use all composite components to take advantage of the light weight, high stiffness,

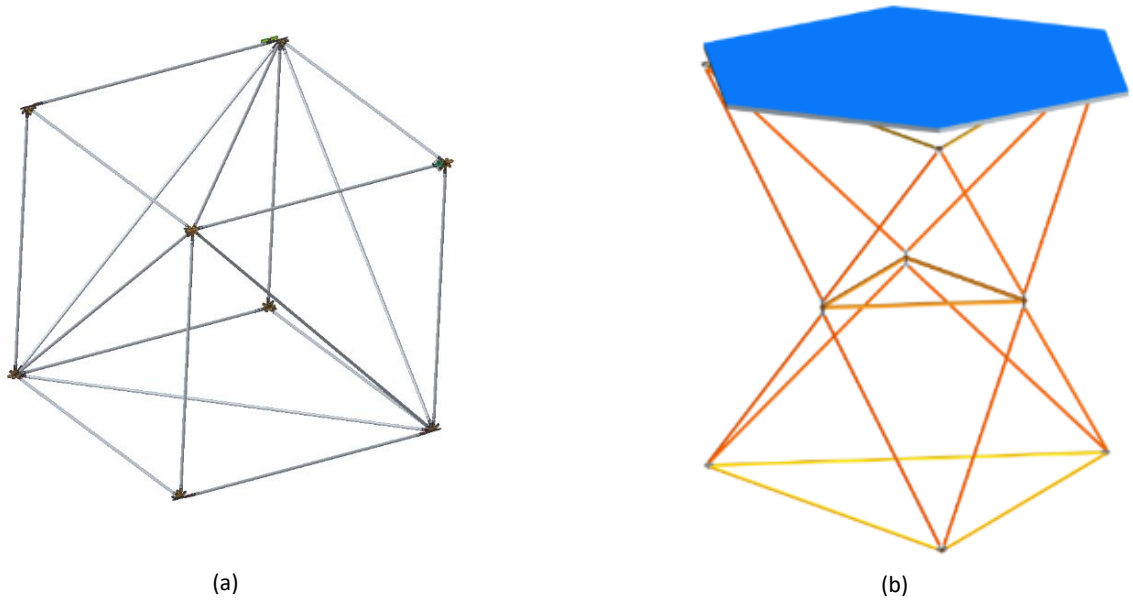

Figure 1.1: (a) Cubic Truss (b) Tri-Truss with integrated mirror.

and low coefficient of thermal expansion (CTE). Each truss is designed to integrate with similar modules to create larger structures to build a base for a PA. The cubic trusses can be used to create long beams or platforms, whereas the tri-trusses assemble into ring-like structures which are nominal for reflectors.

The cubic truss modules can be assembled to create PA's that resemble beams or platforms. These structures can potentially be the backbone for communication arrays, refueling/servicing depots, science stations, solar electric propulsion tugs, etc. Since the module is made up of truss members, there is adequate space within the module to house instruments, fuel tanks, or any component that is needed for the specific mission. Figure 1.2 shows the integration of components within a cubic truss based system. The components within the module are sub-systems that support module operations or payloads that must be transferred. One example of a module is the propulsion system which includes tanks, thrusters, and gimbals. The components can be any size or shape as long as they fit the geometric constraints of the PA (Doggett et al., 2018).

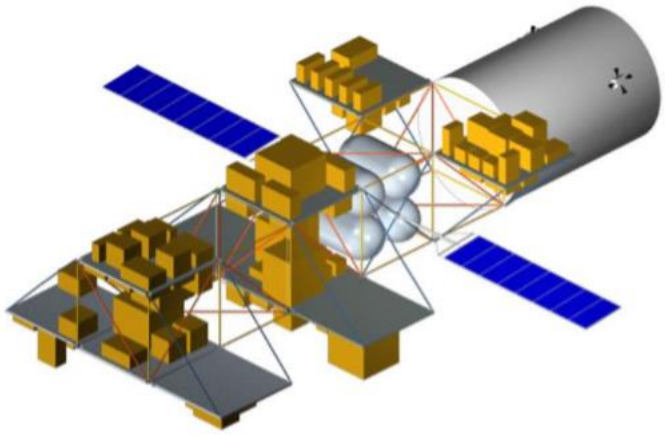

Figure 1.2: Cubic truss based PA with integrated components (Doggett, et al., 2018).

The tri-truss module was developed by researchers at NASA LaRC and due to its unique geometry it can be the basis for planar or curved area PA's. The different geometry PA's can be utilized for platform or reflector applications respectively. Some important features of the tri-truss module are:

- the module is statically determinate,
- when connected to other modules, there are no repeated structural members at the interface,
- the primary load paths along the top and bottom faces of the connected modules pass through the center of the struts and nodes,
- the tri-truss can be collapsed and packaged, and
- mirrors, payloads, and any supporting systems can be pre-integrated on specific tri-truss packaging schemes.

The tri-trusses can be assembled in groups of three using a multi-nut that can either allow for a flat or curved platform. When the tri-trusses are assembled together, the modular structural system behaves like a honeycomb sandwich structure, where the axially stiff top and bottom layers are connected by core structural members that provide shear stiffness through the thickness (Doggett et al., 2019).

Applications of these PA's include both zero-G and planetary surface concepts. Some concepts include a Solar Electric Transport Vehicle (SETV), a Large Precision Reflector, and an Erectable Support Structure for planetary surface solar array modules. A potential SETV design includes a deployable truss and solar array with propulsion and a backbone of truss segments, similar to the system shown in Figure 1.2. NASA has had interest in developing a 20 meter-class precision reflector since the 1980s, however a major technology barrier for a reflector of this size

is reliable and affordable on-orbit deployment and assembly. The tri-truss module was designed to break through this barrier, and is currently being investigated as a potential unit module for a Large Precision Reflector. One concept for a solar array structure on Mars involves reducing mass and improving the packing efficiency of high power solar arrays through the use of PA modules. However, there is predicted to be a limitation on the module size that limits the power range to 200 to 300 kW; the solution to expanding power capabilities would require modular construction, similar to what was done on the ISS (Doggett et al., 2018).

PA's are a viable solution for the expansion of missions beyond the current capabilities in space and on planetary surfaces. Modular expansion through truss units can be used to augment a variety of missions and redefine the current paradigm of single launch systems. Through unique packaging and deployment designs, light-weight structures and SHM systems, and state-of-the-art robotic assembly agents, PA's open up a new scope of possibilities for in-space and planetary missions.

1.2 Packaging and Deployment of Truss Modules

The truss modules proposed to be used as a basis for PA's were designed to be light-weight yet voluminous to allow for the integration of subsystems and payloads. Although some subsystems may be pre-integrated into the truss modules prior to launch, there will be modules that will not have components within and will serve simply as part of the backbone structure. These backbone truss modules will have to be packaged in order to allow for a high number of modules to be launched in the payload fairing.

The tri-truss has undergone the most design review regarding packaging and deployment due to the iSAT project which is a Large Precision Reflector that utilizes the tri-truss modules as unit structures. For the iSAT project, the tri-trusses are proposed to be launched within a Falcon

Heavy which has a payload fairing with a 4.6 m dynamic envelope interior diameter and a length of 6.7 m. In order to fit within this payload fairing but also be the proper size to serve as the backbone for a 20-meter diameter, the proposed tri-truss has a height (H) of 3 m and a base (a) of 3 m. The H/a = 1 ratio was chosen as a parameter of the overall structures stiffness, since the sandwich structure's stiffness is proportional to the truss depth.

A tri-truss trade study team was organized to analyze different concepts for packaging and deployment of the tri-truss module. There were many proposed designs for tri-truss packaging, however the two concepts that were analyzed for this paper were the Telescoping Middle Tri-Truss and the Camping Chair Tri-Truss. Figure 1.3 shows an example of the Telescoping Middle concept in both the deployed and packaged states. For this concept the

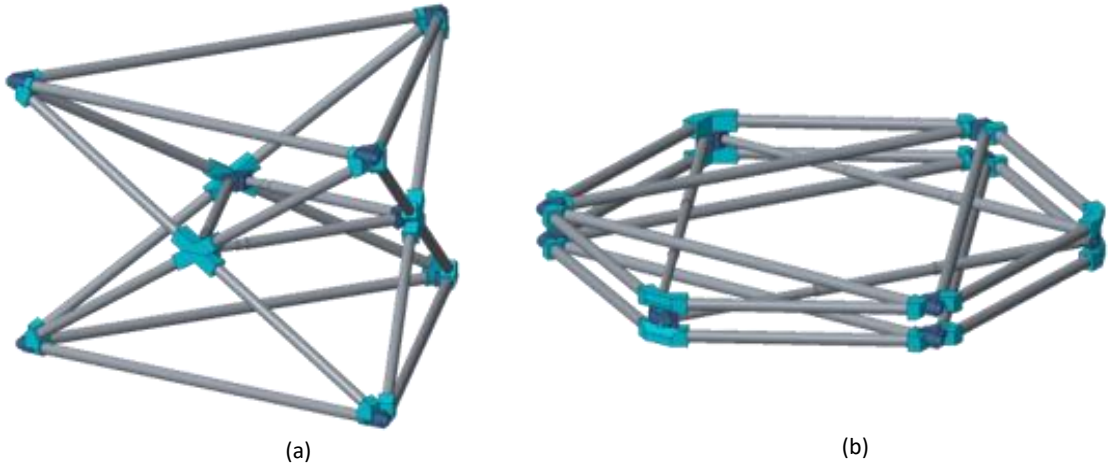

Figure 1.3: Telescoping Middle Tri-Truss Design (a) Deployed (b)

horizontal inner triangle within the middle plane actuates and expands while the vertical side faces of the tri-truss fold onto themselves in order for the module to fold flat into a hexagon profile. This specific design has an H/a = $\sqrt{3}/3$ because the H/a = 1 concept would exceed the payload fairing dimensions when packaged. This reduction in depth was the main reason why the Telescoping Middle design concept was not considered for continuation by the tri-truss trade study team. Figure 1.4 shows an example of the Camping Chair concept in both the deployed and

packaged states. This design uses hinges in every horizontal member and a scissor hinge at the middle plane for the diagonal members to hinge up to a more vertical configuration, the

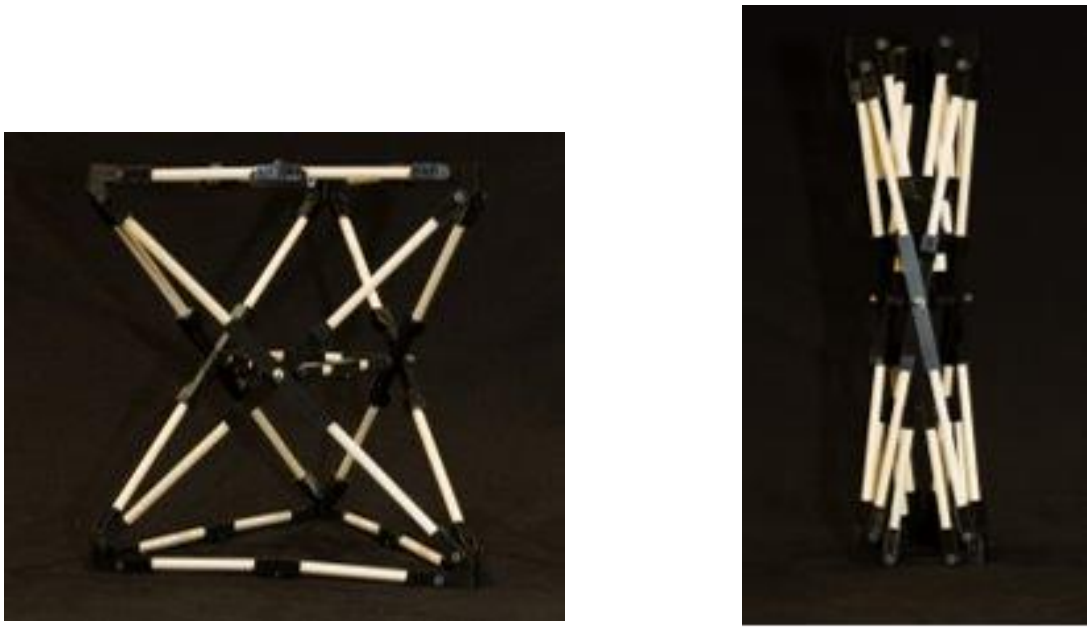

Figure 1.4: Camping Chair Tri-Truss Design (a) Deployed (b) Packaged.

packaged state resembles that of a camping chair, thus explaining the name of the concept. The Camping Chair design cannot have components pre-integrated before launch, however the packaging efficiency within the payload fairing makes it a viable option for a backbone unit structure.

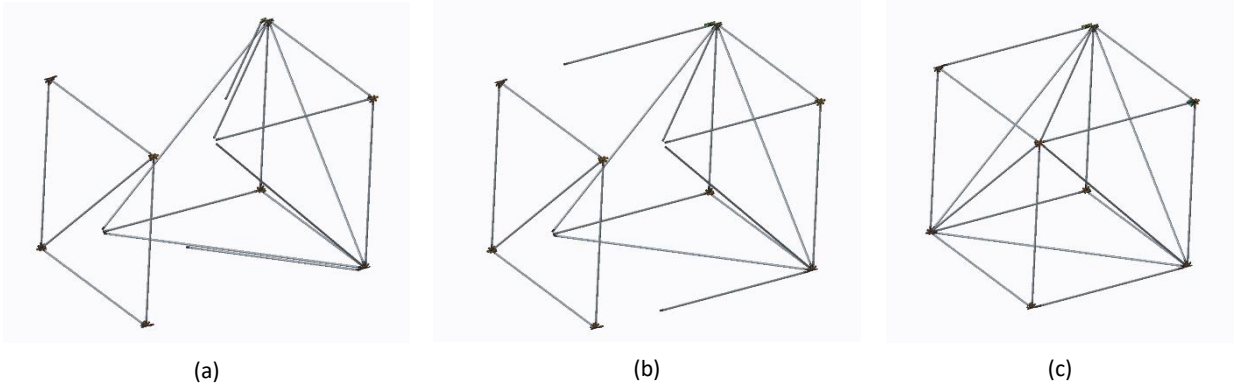

Figure 1.5: Cubic Truss Assembly Process (a) Active end approaching passive end (b) Active end deploying stowed members (c) Full cubic truss connection.

The cubic truss has not had as robust of a design review for packaging and deployment as the tri-truss, however the deployment concept that exists will be used in this paper. The packaging and deployment of the cubic truss is not of the whole truss, but rather of the ends which act as an adapter to the next chain of cubic trusses. Figure 1.5 shows a representation of cubic truss assembly, where the trusses shown would be attached to longer chains of cubic trusses on their respective sides and the shown procedure is for connection the two chains. In Figure 1.5 (a), what is referred to as the active end adapter is on the right and the passive end adapter is on the left. The active end adapter represents the end of an incoming chain of cubic trusses, and the passive end represents the cubic trusses that are already part of the system. In Figure 1.5 (b) the two stowed members on the active end are deployed and in Figure 1.5 (c) the two end adapters are assembled to create a cubic truss connection.

The aforementioned designs will be used to develop a concept for packaging and deployment using SMAs that utilize the materials unique properties to complete not only actuation but also strain sensing to monitor the structural health of the respective modules. Although the SMAs are to be applied to both the tri-truss and cubic truss modules, the two member deployment of the cubic truss adapter provides a simple joint concept that can be used to verify the use of SMAs as a deployment actuator and strain sensor across the joint. In this paper, the cubic truss joint will be the main focus of tests and analysis for the integration of SMAs.

1.3 Applications of SMAs to Truss Modules

The multi-functional use of SMAs helps in the endeavor to minimize parasitic mass across modules. Using both the actuator and sensing functions of a single SMA mechanism can negate the need for separate mechanisms for deployment and structural health monitoring. The SMA mechanism eliminates the need for a conventional bulky actuator for deployment which

greatly reduces the mass of the system. Although a robotic arm could be used for deployment, the SMA mechanism forgoes this need until the assembly stage; this would allow for the removal of certain grapple points necessary for truss deployment, and thus reduce the robotic arms travel distance and energy usage. Due to the SMA's unique properties, the SMA can be used to self-sense during the deployment phase to monitor the health of the truss or verify the position of the SMA actuator during the deployment process. After the deployment process, the SMA would remain on the truss to serve as a strain sensor for structural health monitoring.

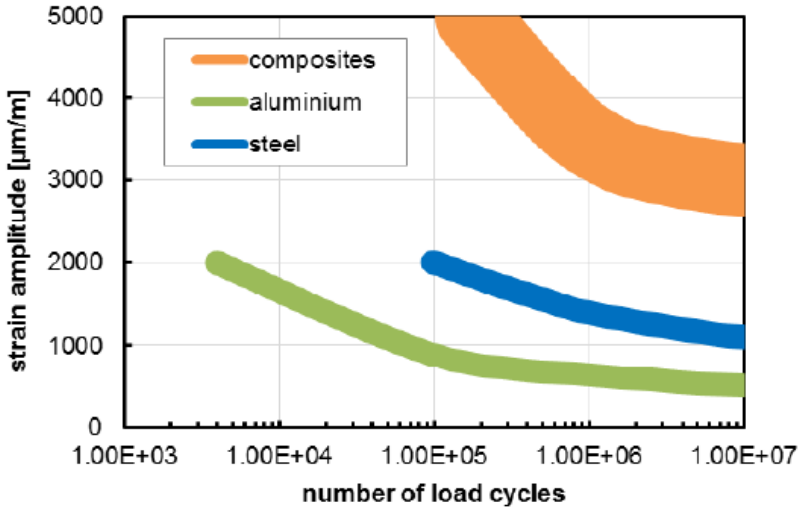

Figure 1.6: Fatigue behavior of various materials (Mäder et al., 2017).

In comparison to conventional actuators and sensors, SMAs have both a higher force-to-weight ratio and gauge factor than its typical counterparts. For example, in order to produce 500 N of force and a travel length of 5 mm a SMA wire of 6 g (2 Oz) would be required, whereas a solenoid would require almost two to three orders of magnitude more mass to achieve the same function (Pick, n.d.). In theory the mass of the SMA wire is much less than conventional actuators; in practice the shielding and necessary batteries for SMA heating adds the majority of the mass for the mechanism. The power required to actuate the SMA can be pulled from a central battery which would primarily be used by a mounted subsystem within the truss module. The

SMA shielding will not exceed the mass of a conventional motor, overall the mass necessary for SMA actuation will be less than a conventional actuator.

For sensing, pseudoelastic SMA wires can have gauge factors that exceed 6 which are higher than most conventional metallic strain gauges. Conventional strain gauges have fatigue strengths higher than most metals, and thus do not break before aluminum or steel in fatigue tests or under cyclic loading. However as can be seen in Figure 1.6, composite materials have higher fatigue strengths compared to the aluminum and steel, and conventional strain gauges would break before the composite under cyclic loading (Mäder et al., 2017). Due to the material's high elasticity and fatigue strength, SMAs are a viable substitute to conventional strain gauges to monitor composite structures.

This project investigates the use of one SMA mechanism to fulfill both actuation and sensing requirements. SMAs have the potential to provide more efficient actuation and sensing, however the multi-use functionality has not been duly verified. By taking advantage of both functionalities, the PA paradigm can be more accurately realized through the minimization of parasitic mass and automation of modular truss structures.

CHAPTER 2: SMA Background

2.1 SMA Overview

In this section the author will discuss two unique thermomechanical properties of SMAs which are the Shape Memory Effect (SME) and Pseudoelasticity. The importance of the material specific transformation temperatures will be highlighted through relationships that govern the physical properties of the SMA. Different variants of SMAs will be introduced and the changes in thermomechanical properties depending on the composition of the alloy will be discussed.

2.1.1 Thermomechanical Relationship

SMAs have a unique thermomechanical relationship due to changes in the crystal structure of the material under different temperature and stress conditions. The SMA molecular structure has two main phases: the martensitic phase and the austenitic phase. Martensite is present as a low temperature phase with a tetragonal or monoclinic crystal lattice whereas austenite is present as a high temperature phase with a symmetric cubic crystal lattice (Hartl & Lagoudas, 2007). There are 4 material property temperature parameters that dictate the phase transformations of an SMA. These material properties are defined as A_s, the austenite start temperature, A_f, the austenite finish temperature, M_s, the martensite start temperature, and M_f, the martensite finish temperature. For most SMAs the following relationship is valid: $M_f < M_s < A_s < A_f$. The transformation is due to the free energy of the material phases, where cooling an SMA in the austenitic phase will produce a normal thermal contraction until a critical temperature is reached at which the martensitic phase has less free energy than the austenitic phase and the crystal lattice abruptly changes. The equilibrium temperature where the free energy of the both phases is equal is given by Equation (2.1).

$$T_0 = (M_s + A_f)/2 \qquad \text{Eq. (2.1)}$$

The phase transformation can be induced by both temperature and stress changes. The most unique quality of this material is that the SMA can be strained to a state that may seem like plastic deformation, however when heated the material will return to its original shape, hence the term ‘memory’. Typically, unrestrained SMAs can recover strains up to 8% when deformed axially. When the SMA is blocked from returning to its original shape after being heated, the phase transformation can generate a large tensile stress up to 800 MPa; this is called constrained recovery and is the basis for SMA actuators (Angioni et al., 2010).

SMAs can be fabricated in a single crystal or polycrystalline form, however the majority of SMAs are polycrystalline. The phase transformation occurs in each crystal grain, so in poly-crystals the total macroscopic response of the crystallographic effects is an average of all the transformations within every grain. This micromechanical averaging produces a smooth material response, as opposed to a single crystal form, because the different grains transform at different times due to the variation in the crystal orientation and differing local stress concentrations (Hartl & Lagoudas, 2007).

The difference in temperature transformation regions, A and M, causes a hysteresis curve that can be modelled using the martensite fraction, ξ, which varies from 0 for fully austenitic to 1

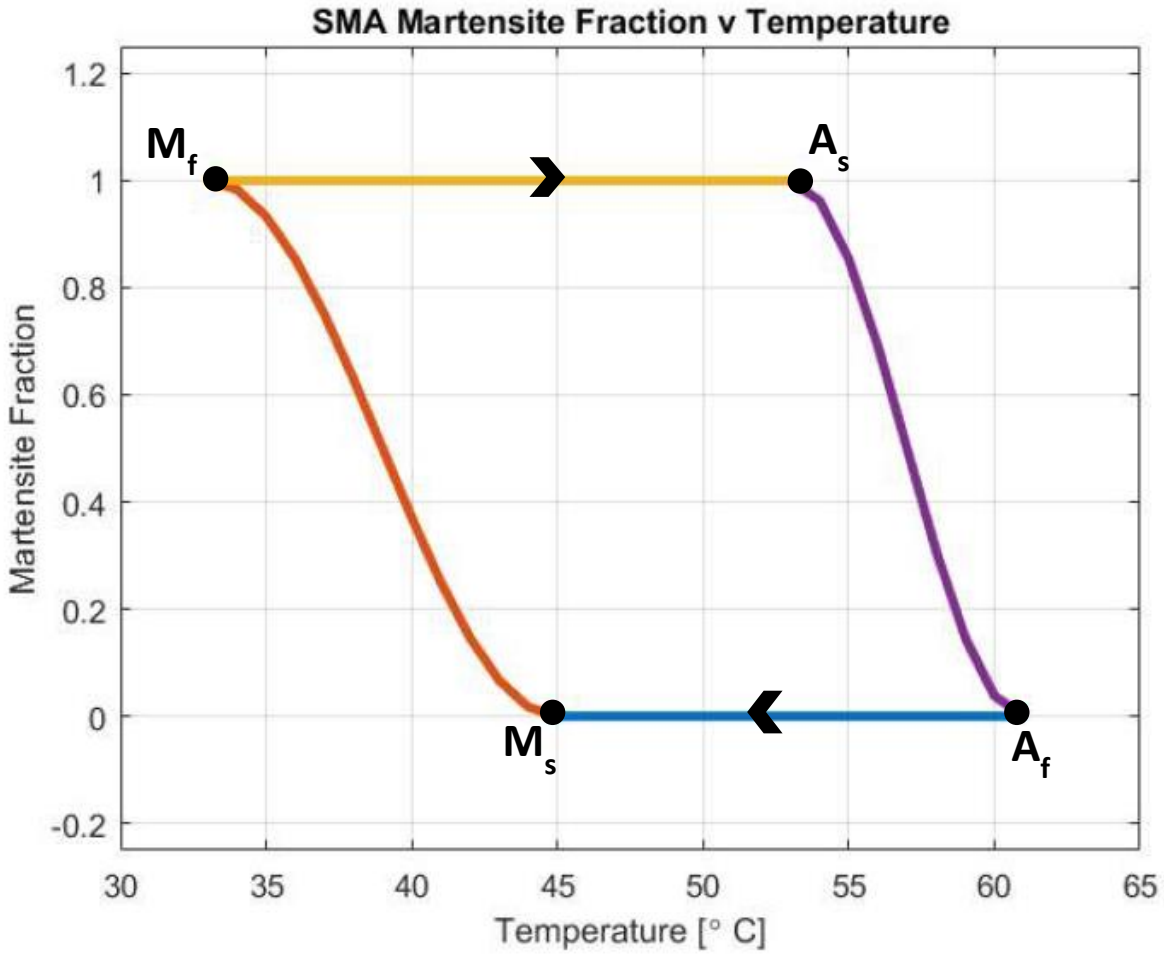

Figure 2.1: Martensite Fraction vs Temperature.

for fully martensitic. A typical martensite fraction vs temperature graph can be seen in Figure 2.1, where the transition temperatures are labelled along the curve. Numerically, the martensite fraction can be calculated using the following equations where θ is temperature of the SMA:

1. A_f to M_s: $\xi = 0$
2. M_s to M_f: $\xi(\theta) = \frac{1}{2}\{\cos[a_M(\theta - M_f)] + 1\}$

   where: $a_M = \frac{\pi}{(M_s - M_f)}$

3. M_f to A_s: $\xi = 1$
4. A_s to A_f: $\xi(\theta) = \frac{1}{2}\{\cos[a_A(\theta - A_s)] + 1\}$

   where: $a_A = \frac{\pi}{(A_f - A_s)}$

Eq. (2.2)

The code used to create Figure 2.1 can be found in Appendix A.

Although the equations for region 2 and 4 are not exact models, the cosine functions are a viable fit for the relationship. Another note to make is that these relationships are valid when there is zero stress applied to the SMA. When stress is applied to the SMA the transformation temperatures vary almost proportionally, and although the relationship is not strictly linear, the overall slope of the transformation temperature vs applied stress is referred to as the stress rate or stress influence coefficient. The equivalent transition temperatures can be calculated using the following equations where T is applied stress and C_M and C_A are material properties of the specific SMA:

$$M_f^* = M_f + \frac{T}{C_M}$$

$$M_s^* = M_s + \frac{T}{C_M}$$

Eq. (2.3)

$$A_s^* = A_S + \frac{T}{C_A}$$

$$A_f^* = A_f + \frac{T}{C_A}$$

2.1.2 Shape Memory Effect

The martensitic phase is comprised of twinned and detwinned compositions. The application of stress above a certain threshold causes twinned martensite to deform in shear into

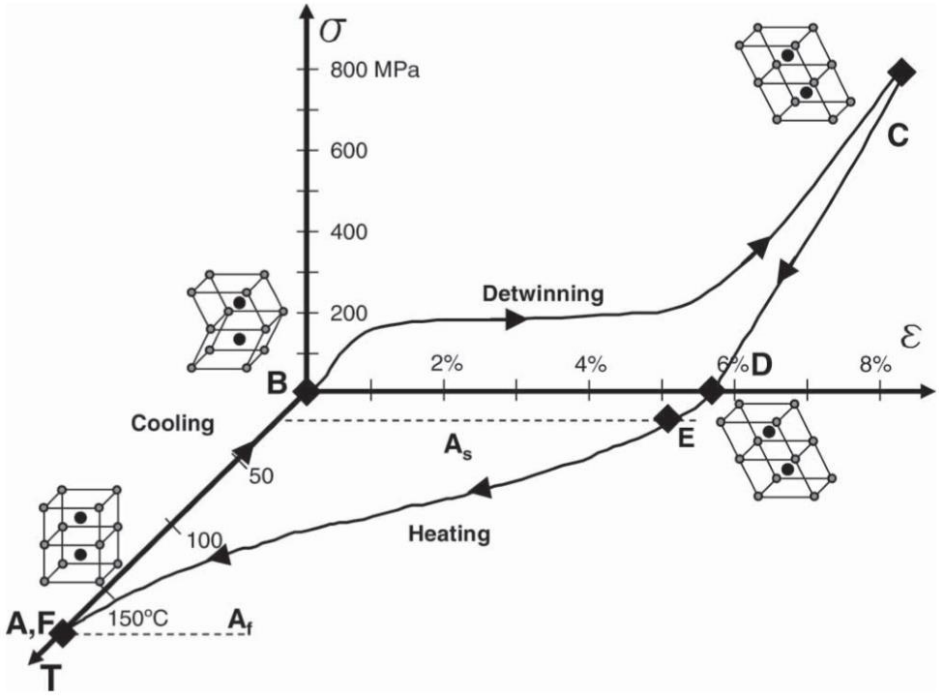

Figure 2.2: Loading path of NiTi wire with regards to stress, temperature, and strain (Hartl & Lagoudas, 2007).

detwinned martensite. This process is not reversible by mechanical means, so when the detwinning load is removed, the SMA remains in the deformed state and the structure remains detwinned. The process of recovering the strains produced by the detwinning process is known as the stress-free SME and is produced through the heating of the wire such that the SMA returns to the austenitic phase. Figure 2.2 shows the SME in action through the loading path in regards to the temperature, stress, and strain of a Nickel-Titanium (NiTi) wire that was tested at Texas A&M University. The crystal structure of each phase can also be observed at the different points

along the graph. Following the points along the graph, the process starts at point A where the SMA is in the austenitic phase and has a symmetric cubic crystal lattice. Upon cooling of the SMA, the phase transforms to twinned martensite; the crystal structure of which can be observed

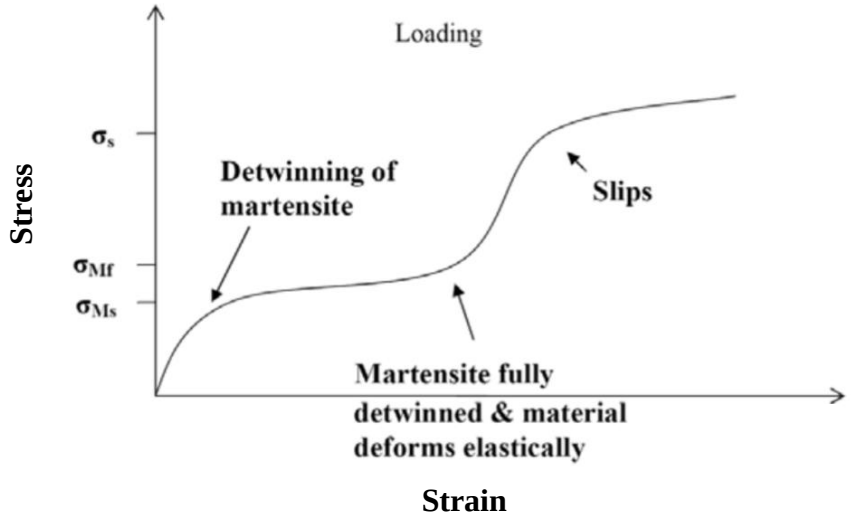

Figure 2.3: Stress-strain curve showing the detwinning of martensite and onset of plastic slip (Hartl & Lagoudas, 2007).

at point B. Stress is applied to the twinned martensite which transforms the SMA into detwinned martensite and large strains are observed at point C. When unloaded, the elastic strains of the SMA are recovered however the inelastic strains from the detwinning process remain at point D. As the SMA is heated to A_s, the reverse transformation the austenite begins at point E. This reverse transformation continues until the SMA is fully austenitic at point F. In this experiment, plastic strains were neglected so point F and point A coincide (Hartl & Lagoudas, 2007).

SMAs can deform up to a certain point, and although the seemingly plastic strain caused by the detwinning process can be recovered, there is a maximum deformation the SMA can take before entering actual plastic deformation. Figure 2.3 shows a stress-strain curve of an SMA as it transforms from twinned martensite to detwinned martensite, and then after a certain stress threshold, σ_s, which would be above point C in Figure 2.2, plastic slip occurs. This is a truly irreversible process that dislocates the crystals within the SMA and reduces the apparently yield

strength. If the applied stress on the SMA is too high during heating, the shape recovery will not take place; the maximum stress is known as the blocking stress and is important for SMA actuators. The SME is an important property that is utilized in many SMA actuator designs, however it is important to note the potential for plastic slip through over-loading.

The aforementioned SME is referred to as the One-Way SME, whereas the Two-Way SME can be achieved through proper material training. Transformation-induced plasticity (TRIP) occurs when plastic strains are generated during transformation; these strains are generated more quickly during initial material cycling, but stabilize as the number of cycle's increases. The repetitive transformation cycling is referred to as 'training' the material, and sufficient training can eliminate the production of twinned martensite which causes the austenite

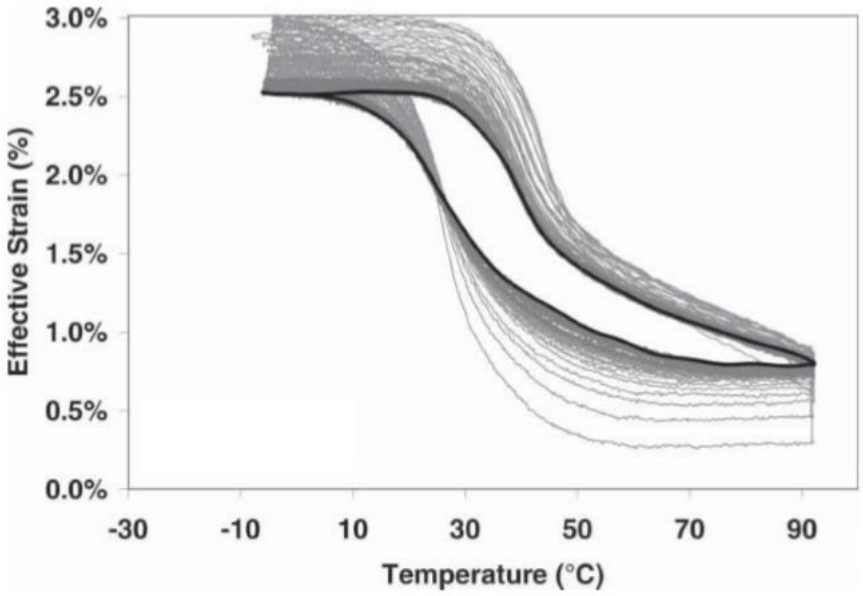

Figure 2.4: Training cycles of an SMA at 300 MPa with varying temperature (Hartl & Lagoudas, 2007).

to transform directly to detwinned martensite, thus driving the minimum stress for shape recovery to zero. This direct transformation from austenite to detwinned martensite is referred to as the Two-Way SME. The training process can be seen in Figure 2.4, which shows the strain response while temperature cycling under constant stress until the material stabilizes in the final cycle which is shown in bold (Hartl & Lagoudas, 2007).

2.1.3 Pseudoelasticity

Another phenomenon of SMAs is called pseudoelasticity, also referred to as superelasticity, where the process begins in the austenitic phase, enters a stress-induced detwinned martensitic (SIM) phase, and then returns to the austenitic phase upon unloading. This effect occurs when the SMA is above A_f for the entirety of the loading process. As will be seen in Section 2.1.4, SMAs come in many forms with various transition temperatures, some which have an A_f below room temperature. Choosing an SMA such that the operating temperature is

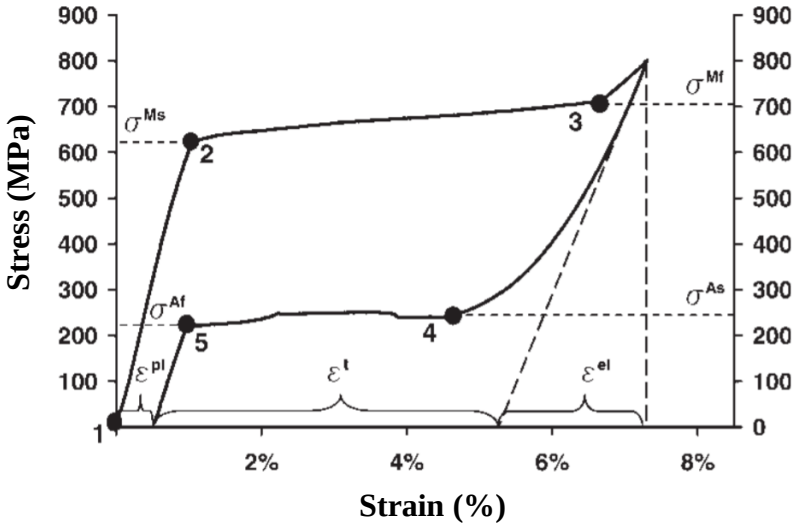

Figure 2.5: Pseudoelastic stress-strain curve at 80°C (Hartl & Lagoudas, 2007).

always above A_f allows the use of the pseudoelastic effect, however there is a temperature to note, M_d, at which SIM can no longer be produced and the SMA will be permanently deformed (Jani et al., 2014).

The pseudoelastic response of an SMA under stress is similar to that of the SME, however the recovery of elastic and transformation strains is possible without a change of temperature. Figure 2.5 shows a stress-strain curve of a pseuedoelastic material at isothermal conditions that was tested at Texas A&M University. While the stress is kept below the transformation stress, σ^{Ms}, the material reacts elastically, however once the transformation stress

is passed the austenite starts transforming into detwinned martensite. This transformation creates the SIM as well as large inelastic strains until the critical stress, σ^{Mf}, is reached; any loading above this point creates an elastic response of the detwinned martensite. When unloaded, the material recovers some strain until it reaches the critical stress, σ^{As}, and the detwinned martensite begins the transformation back to austenite without the addition of heat since the ambient temperature is already above A_f. When the material becomes fully austenitic, the elastic and transformation strains, ε^{el} and ε^{t} respectively, have been recovered and only the residual plastic strain, ε^{pl}, remains, which in this case is approximately 0.6% (Hartl & Lagoudas, 2007).

2.1.4 SMA Materials

SMAs are part of a larger subset of Shape Memory Materials (SMMs). A smart or intelligent material is a material which has intrinsic sensing, actuating, or controlling capabilities in its microstructure. Some of these materials that exhibit multifunctionality or couplings are piezoelectrics, fiber-optics, magneto- or electro-strictive materials, magneto- or electro-rheological fluids, and other functional polymers; however SMMs specifically exhibit functions such as the SME, pseudoelasticity, high damping capacities, and adaptive properties due to reversible phase transformations. SMMs can tune physical parameters such as strain, stiffness, position, natural frequency, etc. and most commonly can recover their original shape after seemingly plastic deformation using thermal, mechanical, magnetic, or electrical stimuli (Wei et al., 1998) (Huang et al., 2010). SMMs can be found in the form of alloys, ceramics, polymers, and gels, however SMAs are the most widely used of the SMMs and is the focus of this paper.

SMAs can be produced in a variety of molecular compositions and physical configurations such as fibers/wires, short fibers/whiskers, particles/particulates and foils/sheets/films. The different molecular compositions and physical forms of SMAs allow for

the implementation in a variety of applications. The SME was initially found in an AuCd alloy in 1932 by Arne Ölander, however the term "shape memory" was not coined until 1941 by Vernon. In 1962, Buehler and Wang found the SME in a NiTi alloy which was then observed to have a significant recoverable strain in 1971 at the Naval Ordinance Laboratories (NOL) in the USA (Jani et al., 2014). The term Nitinol was coined as a combination of the composition of the material, NiTi, and the location NOL (Huang et al., 2010).

Many more alloys were discovered over the following decades, however the most commercially important alloys are NiTi-based, Cu-based, and Fe-based. All these alloys show a thermal response, however NiTi-based alloys show have high performance, whereas Cu-based and Fe-based alloys show an instability, brittleness, and poor thermo-mechanical performance that exclude them from many engineering applications (Huang et al., 2010) (Van Humbeeck, 1999). Some advantages of Cu-based alloys are that they are low in cost and fabrication complexity in comparison to NiTi alloys and some of the alloys such as CuZnAl and CuAlNi have been extensively studied. Some Cu-based alloys such as CuZnAl alloys are a candidate for high temperature SMAs, however their processibility and thermal stability must be improved before they are a more viable option. Fe-based alloys are also relatively low cost and recently have attracted more attention due to the ability of alloys, such as FePt and FePd, to produce phase transformation through the application of a magnetic field, however achieving two-way SME requires complex thermal treatments (Wei et al., 1998).

The near stoichiometric NiTi alloy known as Nitinol is the most used commercial SMA due to its shape memory performance, good processibility, and excellent mechanical properties. The material has very good biocompatibility which enables it to be widely used in the biomedical field, and due to the various physical forms, the alloy can be readily used as an active

component in composites as well as microelectromechanical systems, intelligent materials, and structural systems. Slightly changing the alloy composition can have interesting effects on the SMAs characteristics, some of which include changes in transformation temperatures and width of the transformation hysteresis loop. Both of these characteristics are important for dictating the applications and operating range of the SMA. The temperature hysteresis is defined as the difference in transformation temperatures for heating and cooling, i.e. $\Delta T = A_f - M_s$, and is an important parameter for the SMA application. A small hysteresis is desired for fast actuation in microelectromechanical systems and robotics and a large hysteresis is desired to hold a predetermined shape for a large temperature range such as deployable structures (Jani et al., 2014).

Narrow-hysteresis SMAs can be produced from NiTi alloys by adding copper, however excessive addition of copper can cause a decrease in the shape-recovery rate and cause the alloy to become too brittle to process. The ternary alloy NiTiCu can reduce the transformation hysteresis from a normal 30 K to below 10 K, increase the damping capacity, and create a larger difference in toughness between austenite and martensite. These qualities can make NiTiCu viable in an actuator application. Wide hysteresis SMAs can be produced by adding niobium to NiTi, creating a difference of up to 150 K between the A_s and the M_s ; as the Nb content increases the M_s decreases (Xu et al., 2003). The wide hysteresis SMAs can be used in couplings and fixing applications, and are available commercially as $Ni_{47}Ti_{43}Nb_9$ (Wei et al., 1998).

The substitution of Ni with palladium, platinum, and gold within the NiTi alloy can increase the transformation temperatures to up to 873 K while still exhibiting the SME. This effect can also be achieved with the substitution of Ti for hafnium and zirconium in NiTi alloys.

These alloys are in a class called High-Temperature SMAs (HTSMAs), and despite the high cost, they allow for SMA applications in very hot environments. HTSMAs are defined as any SMAs that can exhibit the SME at temperatures above 373 K. HTSMAs are difficult to process and train due to their poor performance at room temperature, so currently the only useful alloys operate at a range from 100-300°C and include the alloys TiNiPd, TiNiPt, NiTiHf, NiTiZr, and CuAlMnNi (Jani et al., 2014).

There is an intermediate phase known as the R-phase which exhibits a rhombohedral crystal structure and only appears in special cases due to the specific alloy composition and temperature parameters. The R-phase is often absent from SMAs, however it can appear during cooling before transformation to martensite and during heating prior to transformation to austenite. Titanium rich alloys and fully annealed conditions prevent the R-phase from forming. The R-phase is more pronounced with the addition of iron, cobalt, and chromium, and is suppressed by the addition of copper, platinum, and palladium. The recoverable strain for the R-phase is on the order of 0.5% whereas for the martensitic transformation it is on order of 6.5-8.5%. Some attractive properties of the R-phase include stability to thermal cycling and ageing, very small thermal hysteresis, and very high fatigue life (Uchil, 2002) (Nagai & Oishi, 2006).

There have been many alloys discovered that exhibit the SME, however the alloys have not all been investigated in enough depth to allow them to be commercially available or even viable in engineering applications. A full list of known SMAs and their given transformation temperatures can be found in work of Zarinejad & Liu, (2010).

2.2 SMA Applications

In this section the author will discuss the many applications of SMAs that are possible due to the SME and piezo-resistive effect. Most of the past applications of SMAs are as actuators

in deployment, self-rehabilitation, and damping of structure. These applications are due to the high recovery stresses that are created from the SME. SMAs have also been used as sensors in both self-sensing during actuation and as strain gauges in structures. This is possible due to the piezo-resistive effect which is a component of the gauge factor, the principle by which strain gauges operate. The author will explore these applications and compare them respectively to their conventional alternatives.

2.2.1 Sensors

2.2.1.1 Temperature Sensors

SMAs have a limited set of sensing functions, however clever use of their unique couplings can result in sensors that have more applications than traditional options. Temperature changes will be converted to physical shape changes when the SMA is within the proper temperature range, and this can be used to adapt the material to a particular environment or to signify a crossing of a specific temperature threshold. The use of electrical resistance (ER) change due to phase transformation changes can be used to indicate temperature variations. Cu-based alloys can show a change in ER on the order of 2% during phase transformation, and by measuring the rate of change of ER, a circuit can indicate when a certain temperature value has been crossed (Van Humbeeck, 1999).

Conventional temperature sensors show the current temperature, and do not provide an indication of out-of-range temperatures without additional equipment. A SMA temperature sensor could indicate when a certain temperature threshold was crossed, and provide a permanent recording of the event. A patent was filed in 2001 for a temperature sensor that comprises of an SMA element in tandem with a restraining element; the SMA within the sensor remains hardened and at a length that is lower than necessary to engage a restraining element. When the

temperature falls below a critical threshold, the SMA softens and engages the restraining element which then makes a permanent change in the structure of the sensor system. This makes sure that if the temperature does rise above the critical threshold, the sensor is still in the restrained position and will provide a persistent indication of the event (Shahinpoor, 2005).

Due to the unique thermomechanical coupling, SMAs are intrinsic temperature sensors which change shape depending on the specific SMA's temperature parameters. The change in shape allows the SMA to act as a latch, indicator, actuator, etc. when a certain temperature is reached and this provides a multifunctional benefit that eliminates the need for additional sensors or recording systems.

2.2.1.2 Strain Sensors

SMA wires can be used as strain sensors by using their piezo-resistive relationship of the variation of ER with strain. Supplementing the actuator functionality, the ER can be measured during actuation of the SMA to keep track of the strain acting on the material. This application has been investigated many times before, and it has been shown that it is viable to measure the position of the SMA as it is being actuated. This relationship can also be utilized to use the SMA as a static strain sensor. If the pseudoelastic effect is utilized, the SMA strain sensor can be strained up to 80,000 μm/m, and in cyclic loading conditions the strains can reach around 20,000 μm/m. The SMA sensors can also be embedded into fiber-reinforced plastics through injection molding, laminating, and infiltrating processes (Mäder et al., 2017).

The strain sensing capabilities have been shown to have an easily measureable correlation between the position of the actuator, through strain, and the ER. An experiment was conducted with a NiTi wire to show this relationship. Figure 2.6 shows two sets of data from electrical

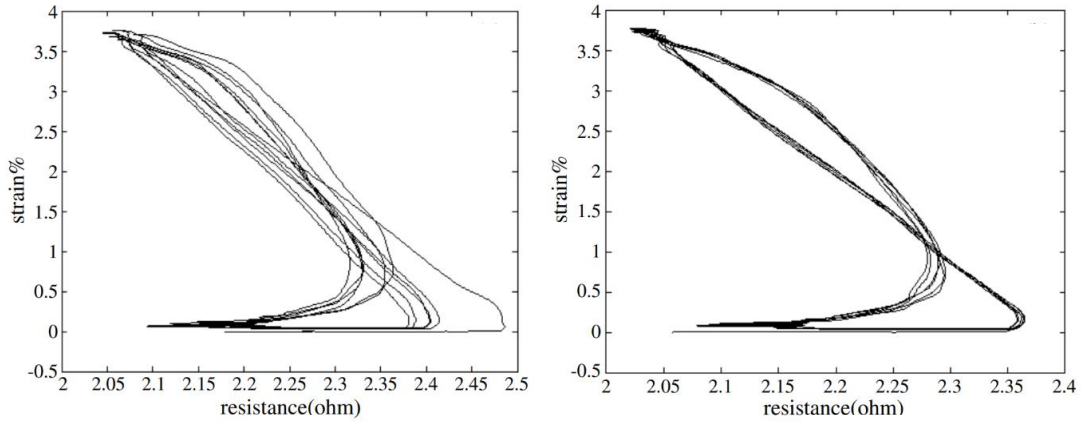

(a) (b)

Figure 2.6: Strain vs Resistance of NiTi wire (a) 360 s cycling (b) 900 s cycling (Ma et al., 2004).

activation cycles of the SMA wire. The first set in Figure 2.6 (a) is from 360 seconds of cycling and the second set, Figure 2.6 (b) is from 900 seconds of cycling. It can be seen that after repeated cycling the response becomes more consistent, most likely due to the residual strain decreasing to zero after repeated activation cycles. The ER relationship with strain changes depending on if the cycle is in a heating or cooling stage, and this creates a hysteresis loop (Ma et al., 2004). Using this correlation, the strain can be monitored for SMA actuators during heating or cooling cycles.

For a static SMA wire, the material has been proven to be a viable replacement for strain gauges. The ER of an SMA wire is given in Equation (2.4) as a function of the wire length, L and cross section, S, where ρ is the electric resistivity which is typically 50 x 10^{-6} Ω cm for NiTi (Nagai & Oishi, 2006).

$$R = \rho \frac{L}{S} \qquad \text{Eq. (2.4)}$$

The variation of ER is not strictly linear, however can be approximated from Equation (2.5) as a function of the strain, where ν is Poisson's ratio and is typically 0.33 for NiTi.

$$\frac{\Delta R}{R} \approx (1 + 2\nu)\frac{\Delta L}{L} \qquad \text{Eq. (2.5)}$$

This relationship from Nagai & Oishi (2006) shows the correlation between the variation in ER and the strain with respect to Poisson's ratio, however this does not take into account the piezo-resistive effect which is present for SMAs. This is important to remember during sensing tests as

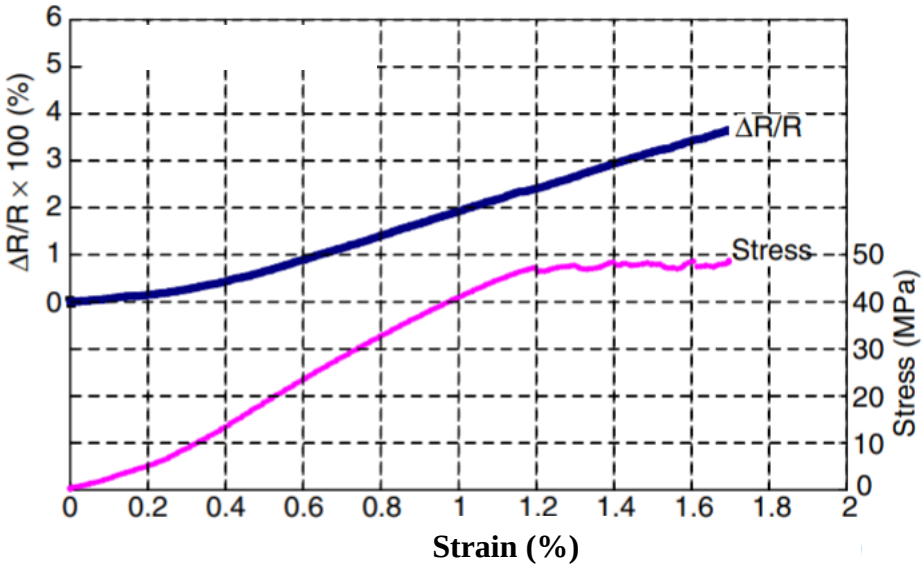

Figure 2.7: ER Variation vs Strain and Stress vs Strain curve of a pre-strained NiTi wire after 2.2% pre-strain (Nagai & Oishi, 2006).

a source of error when comparing to simulations. Equation (2.5) can be used by measuring the change in ER to calculate an approximate strain. Figure 2.7 shows a stress-strain curve and ER-strain curve of a NiTi wire, and shows a measurable variation of about 2% ER change per 1% strain.

It is important to note that the ER varies with the temperature of the material, especially near temperatures that induce phase transformation. To use the SMA as a strain sensor, the temperature dependence must be almost negligible or the relationship must be compensated for by including a reference wire that has the same SMA composition as the sensor, is at the same

ambient temperature, but is under no strain. The ER variation with respect to temperature is given in Equation (2.6), where β is the temperature coefficient, and ΔT is the temperature variation.

$$\frac{\Delta R_T}{R_T} = \beta \Delta T \qquad \text{Eq. (2.6)}$$

Using this relationship, the overall ER variation of the strained wire taking into account strain variation and temperature variation is given by:

$$\frac{\Delta R_{sw}}{R_{sw}} = \frac{\Delta R_T}{R_T}\frac{\Delta R_L}{R_L} = (\beta \Delta T)\frac{\Delta R_L}{R_L} \qquad \text{Eq. (2.7)}$$

The reference wire will only have an ER variation with temperature so the relationship is simply:

$$\frac{\Delta R_{rw}}{R_{rw}} = \beta \Delta T \qquad \text{Eq. (2.8)}$$

Finally, the compensated ER variation takes into account the ER variations from both the strained wire and reference wire to produce the following relationship:

$$\frac{\Delta R_c}{R_c} = \frac{\Delta R_{sw}/R_{sw}}{\Delta R_{rw}/R_{rw}} = \frac{(\beta \Delta T)\Delta R_L/R_L}{(\beta \Delta T)} \qquad \text{Eq. (2.9)}$$

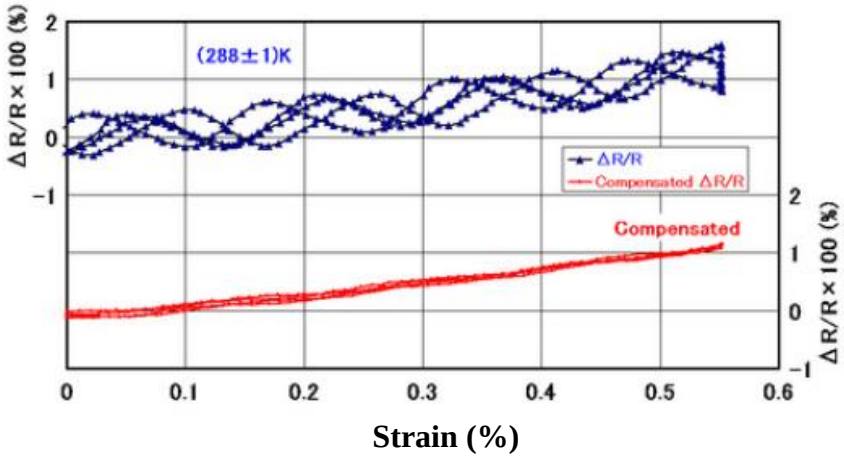

Figure 2.8: ER variation with changing strain and temperature with and without reference wire compensation (Nagai & Oishi, 2006).

An example of the compensated method can be viewed in Figure 2.8, where the top blue line shows the ER variation with changing strain under a couple degrees of variation of the ambient temperature, and the bottom red line shows the same ER variation using the compensation method with a reference wire (Nagai & Oishi, 2006). The addition of a reference wire that adds no strain sensing capability may seem like parasitic mass, however the function it adds to eliminating the temperature dependence term and the almost negligible mass of a single wire make it a viable supplement for sensing strain.

Another unique method of monitoring structural health is the use of acoustic emission (AE) signals, which are created by stress-induced phase transformation of an SMA, to measure deformed locations and strains in a composite. Measuring the variation in ER provides the amount of strain, however deformed areas are not located. The AE signals are observed as elastic waves, and elastic waves have a constant velocity, so using the known velocity the deformed area can be located through the difference in arrival times of the waves at different locations. The strain values are estimated using multiple AE signals. One of the downsides of this method is that it requires two additional AE sensors, however it provides more information than the SMA by itself. As the strain in the SMA wires increase, the AE signals indicate the stress-induced phase transformation and the location of the AE signal generation can be calculated using the following equation:

$$x = \frac{((t_1 - t_2) * v_s + L)}{2} \qquad \text{Eq. (2.10)}$$

In Equation (2.10), t_i (i = 1,2) refers to the time the signal reached the respective AE sensor, v_s is the speed of the elastic wave, and L is the distance between the two AE sensors. Figure 2.9 shows the correlation between strain and cumulative AE events, which for the specific

sample SMA is a linear relationship. In Figure 2.9 (a), the red dots show AE events and in Figure 2.9 (b) the dashed lines represent a statistical uncertainty band for the measurements. Using this

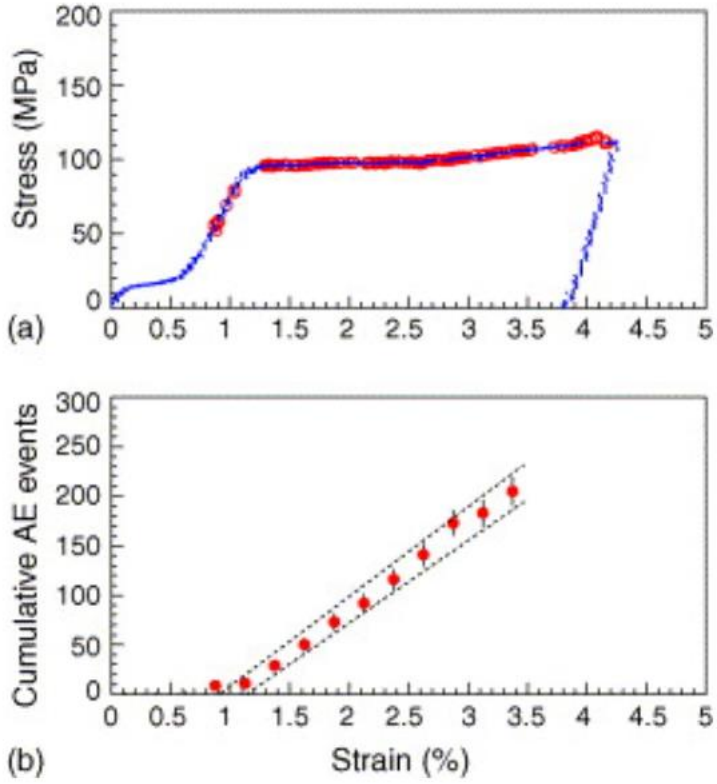

Figure 2.9: (a) Stress-strain curve for a sample SMA (b) Cumulative AE events vs strain in the SMA (Oishi & Nagai, 2005).

experimental correlation, the strain of the SMA within a composite can be estimated using the number of cumulative AE events (Oishi & Nagai, 2005).

2.2.1.3 Comparison to Conventional Sensors

Typically for strain sensing you would use AE sensors, digital image correlation and laser speckle extensometers, Fiber Bragg grating (FBG) sensors, strain gauges, etc. When working with composite materials, especially ones where an SMA is already integrated as an actuator, the addition of more sensors can cause a strength reduction in the composite due to the heterogeneous materials within the sensors (Nagai & Oishi, 2006). FBG sensors require additional complex, expensive, and voluminous measuring equipment which is not a viable option in a space structure where mass and volume within a module are a driving factor in

design. Using a non-contact method with laser speckle extensometers can only be applied in a lab setting. Carbon fibers can be used as strain sensors within composites, however their gauge factor is low and measurements have a high temperature dependence (Mäder et al., 2017). The most viable option is using a strain gauge, however typical strain gauges have their own disadvantages when working with composites.

Conventional strain gauges work well with steel and aluminum structures because the fatigue strength of the structure is lower than that of the strain gauge, however composites can have a higher fatigue strength than typical strain gauges which is not nominal. Under cyclic loading of a composite, the conventional electrical strain gauge would break before the composite, whereas SMAs can show elastic behavior under very large strain levels (Mäder et al., 2017). The gauge factor, k, which is defined using Equations (2.11), shows the relationship between the variations in ER to that in strain (Koncar, 2018). The piezo-resistive effect is defined by the first term in the gauge factor equation.

$$k = \frac{\frac{\Delta\rho}{\rho}}{\varepsilon} + 1 + 2\nu \qquad \text{Eq. (2.11)}$$

$$\varepsilon = \frac{l - l_0}{l_0} \qquad \text{Eq. (2.12)}$$

In these equations, ρ is original resistivity, Δρ is change in resistivity, ν is Poisson's ratio, l is the new length, and l_0 is the initial length. SMAs exhibit a piezo-resistive effect which is represented in the first term of Equation (2.11), this is the piezo-resistive term that was neglected in Equation (2.5). Most metallic strain gauges have a negligible piezo-resistive effect and therefore omit the respective term in gauge factor calculations. For some SMA sensors, the

gauge factor can exceed 6 and for most metal strain gauges the gauge factor is about 2 (Mäder et al., 2017) (Bao, 2005).

There are many options for strain sensing within structures, however many conventional options are more suited for metallic structures that use aluminum and steel. In composite structures, SMAs are a viable option due to their high gauge factor and elastic behavior under large strains. The simple method of measuring strain changes, small volume and mass requirements for implementation, and the multifunctional use as an actuator as well as a sensor make SMAs a viable option for strain sensing in composite space structures.

2.2.2 Actuators

2.2.2.1 Self-Rehabilitation of Structures

The main use of SMAs since their discovery has been in actuator applications, where pre-strains are applied to the SMA such that their strain can be recovered through heating of the material. This function can also be used in structural health monitoring and rehabilitation without the need of additional external features. Integrated SMAs can be used for self-rehabilitation of a

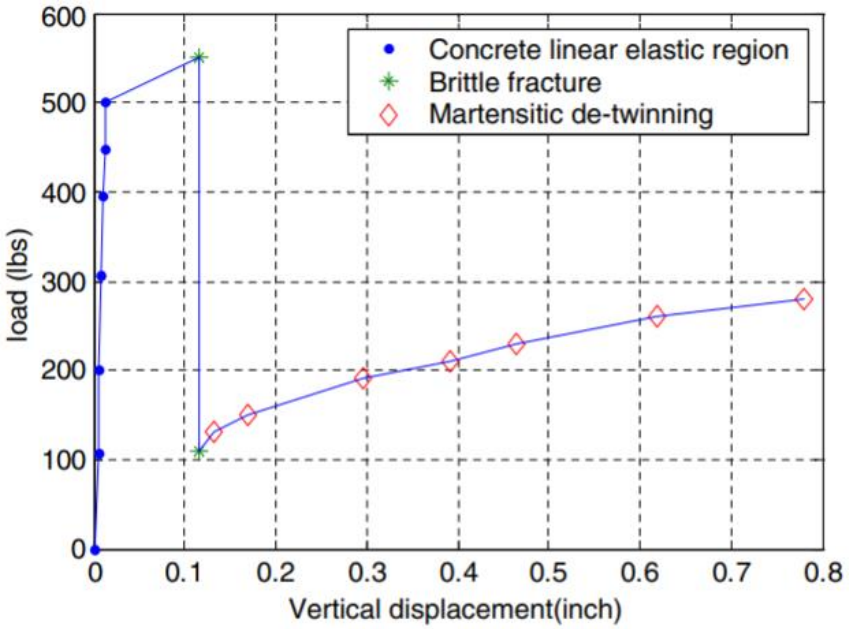

Figure 2.10: Load vs. displacement of the IRCS (Song et al., 2006).

structure, and in composites the SMA can apply compressive stresses to suppress damage from debonding, transverse cracks, delamination, etc. The integration of an SMA into a composite can improve creep and fatigue properties, strengthen the composite, improve damping capacity, and control the shape or vibration properties (Xu et al., 2003).

An example of the use of an SMA for self-rehabilitation is in the concept for an intelligent reinforced concrete structure (IRCS). The IRCS uses Nitinol wires embedded within the concrete to increase the concrete's damping properties and ability to handle large impacts. When the concrete structure becomes damaged and produces cracks, the martensitic Nitinol can be heated to the austenitic phase to recover the strain and close the cracks within the structure. Figure 2.10 shows the loading vs. the displacement of the IRCS structure. The brittle concrete structure exhibits elastic deformation until the brittle fracture point. Once the crack has been formed the loading continues and is mostly acting on the SMA, which undergoes martensite detwinning. As the SMA wires elongate they absorb external energy and increase the damping of the overall IRCS. The load continues until the SMA is strained to ~5%. The crack is then rehabilitated through the electrical heating, also known as Joule heating, of the SMA wire. Figure 2.11 shows the before and after states of the IRCS rehabilitation (Song et al., 2006).

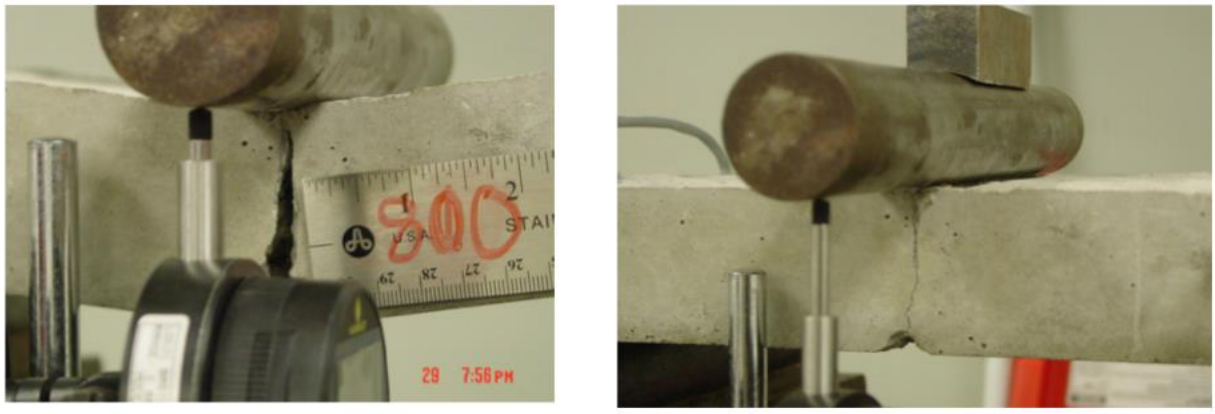

Figure 2.11: IRCS rehabilitation before (left) and after (right) (Song et al., 2006).

Carbon fiber reinforced plastics (CFRP) composites have many uses in aerospace technologies and the implementation of SMAs can be used to suppress any micromechanical damage growth. There have been many studies utilizing the pseudoelastic effect of SMAs in composite materials for damage suppression (Angioni et al., 2010). The pre-strain of embedded SMA/CFRP composites also allows the utilization of recovery stresses when the SMAs are heated, thus suppressing micromechanical damages. For aerospace applications, the damage suppression must be possible at or below room temperature. To achieve this, the M_s must be below room temperature and the transformation temperature must be above the curing

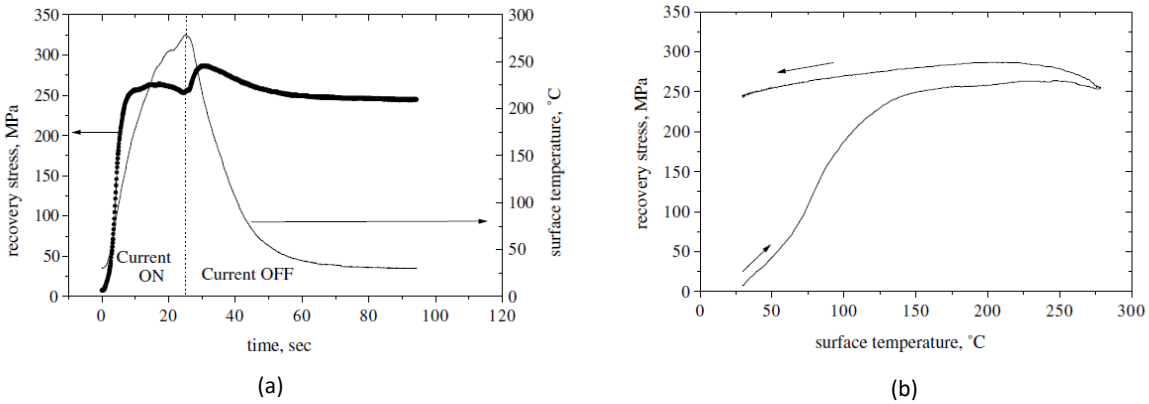

Figure 2.12: Recovery stress produced from Joule heating of a NiTiNb wire (a) Recovery stress vs time (b) Recovery stress vs surface temperature (Xu et al., 2003).

temperature of the CFRP such that the pre-strain that is built into the SMA is not lost when creating the SMA/CFRP composite. Such a large temperature range can be realized by adding Niobium to NiTi alloys, which is known to increase the transformation temperature hysteresis. Xu et al. (2003) created a SMA/CFRP composite using NiTiNb and proved the damage suppression effects of the composite. Figure 2.12(a) shows an example of the damage suppression properties of a NiTiNb wire, which simulates the same that was used to create the SMA/CFRP, under flash heating by electric current. The electric current that was used here was 24 A/mm^2 and the current was kept on for 25 seconds. From this graph it can be seen that a recovery stress of up to 280 MPa is produced when the wire is Joule heated. Figure 2.12(b)

shows the same recovery stresses as a function of the surface temperature of the NiTiNb wire. It can be seen that even after the current is turned off and the wire returns to room temperature, a recovery force of 250 MPa is retained. This is due to the wide transformation temperature hysteresis which is possible due to the composition of the alloy as well as the specific heat treating of the SMA. These recovery stresses are enough for damage suppression in hybrid composites (Xu et al., 2003).

2.2.2.2 Deployment Mechanisms

The deployment of appendages on spacecraft is a common feature in the current era of space missions due to the limited space within the payload fairing of launch vehicles. This need started with the first orbital spacecraft, Sputnik I, and since then deployment operations have become of a greater importance due to increasing power and reliability requirements. Pyromechanisms are still the most commonly used devices for micro-satellites, however nonexplosive deployment mechanisms are available and have been investigated for some time. Some of these options include paraffin-actuated, burn wire, and Nitinol actuated release mechanisms (Fragnito & Vetrella, 2002). These options add some complexity to the system, however the use of SMAs adds more than just actuator advantages. Through unique mounting, the SMAs can be used for deployment of any packaged spacecraft parts, including solar arrays, antennas, and antenna booms. Due to the unique SME of SMA poly-crystals, the transition from detwinned martensite to austenite can provide smooth deployment which is necessary since impulsive deployment can harm fragile solar panels or shift satellite attitude due to quick inertia changes (Van Humbeeck, 1999).

An example of an SMA based deployment mechanism is shown in Figure 2.13, where a

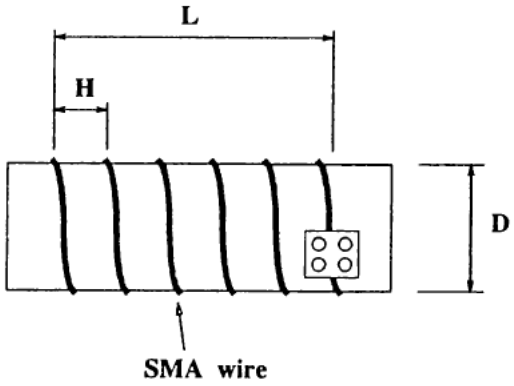

Figure 2.13: Rotary SMA Actuator design (Huang et al., 1996).

Nitinol SMA is pre-strained and wrapped around a shaft of diameter D with one end of the wire mounted to the shaft and the other end is free. In the actuator design, H is the pitch and L is therefore the number of turns, n, multiplied by H. When the wire is heated, the pre-strain is recovered and the shaft turns. The rotation of the free end is given by the following equation where ε is the pre-strain:

$$\theta = 2\pi n\varepsilon \qquad \text{Eq. (2.13)}$$

The rotation angle that is possible from this orientation is dependent not only on the pre-strain and the number of turns, but also the total length, L, of the SMA actuator since the strain is a function of length. This geometric relationship can be seen in Figure 2.14. The deployment angle for a length up to 50 mm is upwards of 200°, whereas in most space packaging schemes, the maximum angle of deployment needed would be somewhere between 90°-180°. For lower deployment angles, lower pre-strains can be used which keeps the strain limits away from the plastic slip limits of the SMA (Huang et al., 1996).

A rotary application of SMAs is in torque tube actuators. This mounting design of an SMA involves using the actual twisting of an SMA rod as the ‘pre-strain’ and heating the SMA such that the twist is recovered, thus producing rotary motion to any object mounted to the rod.

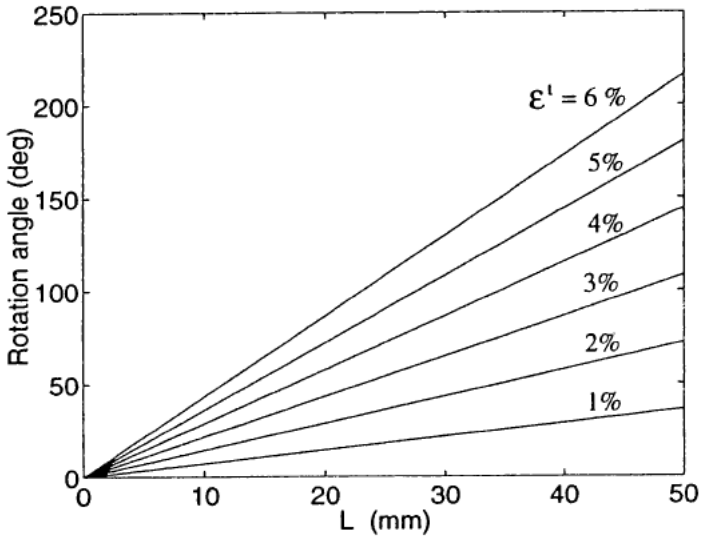

Figure 2.14: Geometric relation between rotation angle, length, and pre-strain (Huang et al., 1996).

The SMA torque tubes produce rotation about the longitudinal axis when heated, and can produce work output of about 30 J cm^{-3} which is comparable to conventional rotary actuators. The benefit of SMA torque tube actuators is that the material itself is providing the actuation thus reducing the mass and volume in comparison to typical motors needed for rotary actuation. NiTiHf torque tubes can provide torque as high as 175 N m (1549 in lbf), and exhibit two way SME (Benafan & Gaydosh, 2019). Although this application of SMAs provides high torques in a low mass and volume package, the mounting of the torque tube actuators is completely perpendicular in the longitudinal axis to the load path along a structure. This is undesirable for using the SMA as a sensor as well as an actuator.

Another concept for deployment mechanisms is using strain energy members which are light-weight and flexible, yet provide high levels of deployment torque. An example of this is a tape spring hinge (TSH) which has high cost effectiveness and reliability as well as low volume and mass requirements. The TSH can be designed to have a high deployed stiffness, however if the stiffness is too high the kinetic energy of the TSH deployment can create a catastrophic deployment which can cause damage to the hinge or the deployable. In order to mitigate this problem, a SMA can be integrated in order to smooth the deployment and act as a damper. Figure 2.15 shows a TSH with a SMA damper module in the stowed and deployed configurations that was designed by Jeong et al. Here the SMA is in martensite in the stowed

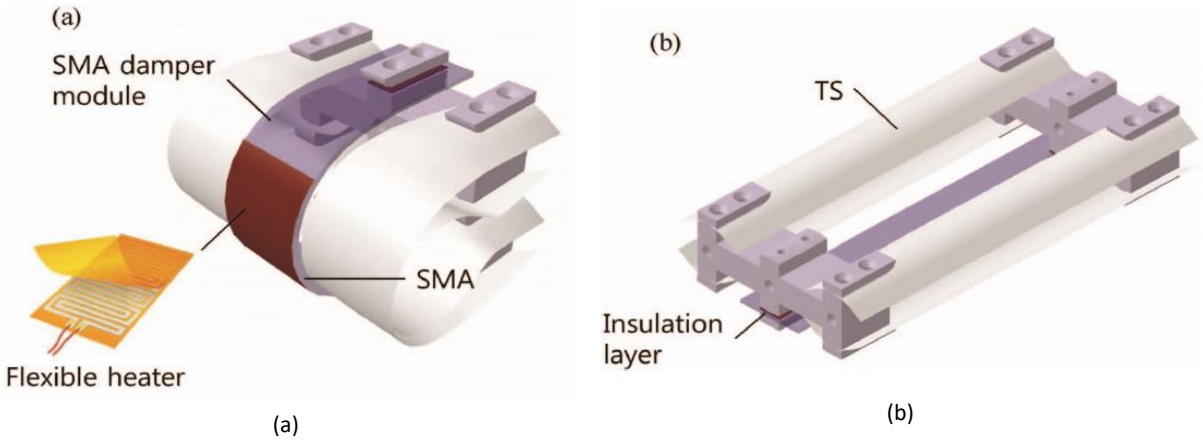

Figure 2.15: TSH with SMA damper (a) Stowed (b) Deployed (Jeong et al., 2014).

position and is heated to start a transformation to austenite. As the phase transforms, the original straight SMA shape is recovered and the plastic moment of the SMA controls the deployment of the SMA as both TS and SMA deploy to the straight deployed position. In order for the SMA damper to be successful, the plastic moment of the damper module must be larger than the average deployment torque of the TSH. Figure 2.16 shows a graph of the plastic moment of the SMA damper, in black, in relation to the deployment torque of the TSH. The TSHs behavior shows high torque at the beginning and end of deployment, however for the majority of the time

the torque is below that of the plastic moment of the SMA damper. The mean of the TSH deployment torque falls below the plastic moment of the SMA damper, so this qualifies as a successful damping system. Another metric for a successful damper can be seen in a shock

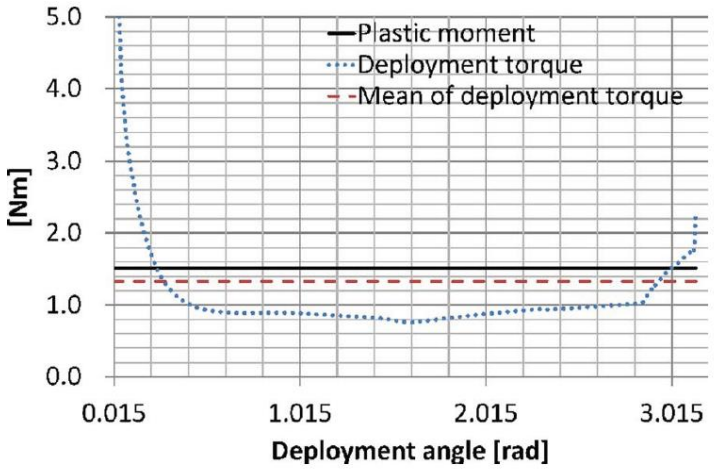

Figure 2.16: Torque vs deployment angle of the TSH and SMA damper (Jeong et al., 2014).

response spectrum (SRS) of the SMATSH device. Figure 2.17 shows a SRS with a threshold that is obtained from an empirical rule-of-thumb containing a 6 dB margin, shown in Equation (2.14).

$$Threshold = 0.8\left[\frac{G}{Hz}\right] * Natural\ Frequency\ [Hz] \qquad \text{Eq. (2.14)}$$

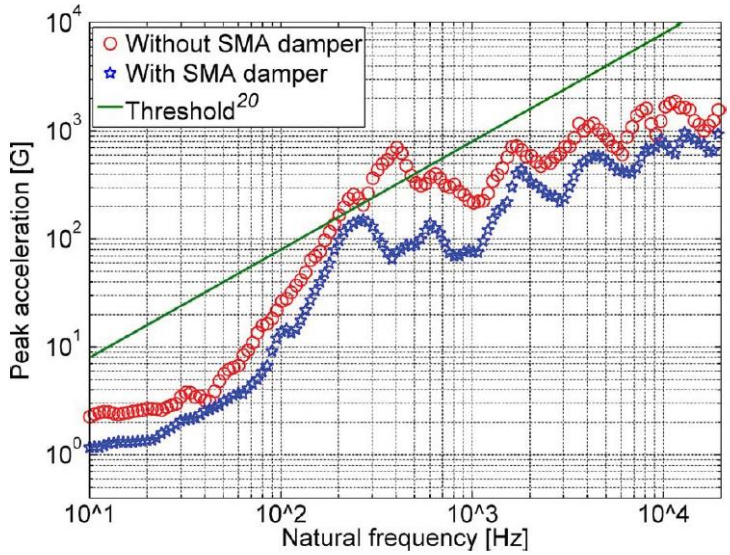

Figure 2.17: SRS of TSH with SMA damper and without (Jeong et al., 2014).

It can be seen from the SRS that the TSH with the SMA damper stays below the threshold while the TSH without the SMA damper crosses the threshold. From these results it was shown that the minimum safety factor without the SMA damper was 0.48 at 380.5 Hz and with the SMA damper was 1.37 at 239.7 Hz, which confirms the viability of the SMATSH mechanism (Jeong et al., 2014).

2.2.2.3 Comparison to Conventional Actuators

SMAs provide many benefits in comparison to conventional actuators such as electrical motors, pneumatics, and hydraulics. The most obvious advantages are the mass and volume saving properties due to the fact that the material itself is providing the actuation and its ability to react directly to stimulus from the surrounding environment. This also provides a significant reduction in mechanical complexity of the actuator as well as the system it is within. NiTi SMAs can display a work density of 10 J cm^{-3} which is 25 times higher than that of electric motors. A NiTi SMA can also lift more than 100 times its own weight. Table 2.1 shows a performance comparison of a NiTi SMA with a variety of actuators (Jani et al., 2014).

The material has multiple uses such as an actuator and as a vibration damper, and has already been shown to be useful as a sensor. The shape and mounting of the SMA also provides flexibility of the actuator and allows it to actuate in all three dimensions. The SMA can be fabricated to extend, bend, and twist, both in isolation and in combination; and can be shaped into springs, wires, torque tubes, and cantilever strips. This differs from conventional actuators

Table 2.1: Actuator performance comparison (Jani et al., 2014).

Actuator type	Stress (MPa)	Strain (%)	Efficiency (%)	Bandwidth (Hz)	Work per Volume (J/cm^3)	Power per Volume (W/cm^3)
NiTi SMA	200	10	3	3	10	30
Piezoceramic	35	0.2	50	5000	0.035	175
Single crystal piezoelectric	300	1.7	90	5800	2.55	15,000
Human Muscle	0.007–0.8	1–100	35	2–173	0.035	0.35
Hydraulic	20	50	80	4	5	20
Pneumatic	0.7	50	90	20	0.175	3.5

such as linear actuators and servo motors which are designed to actuate in one dimension using much more mass and power.

Some downsides of SMAs include the low response time, relatively small usable strain, and low efficiency. The heat transfer rate of the SMA causes the cooling of the actuator to occur very slowly, causing repeatable actuations to be on the order of minutes depending on the size of the SMA wire. There are methods of increasing the rate of cooling of an SMA, however for an application where a single actuating motion is needed, such as the deployment of a PA module, the response time of the SMA does not have as much significance. Using the SMA actuator function once with onboard batteries for heating the SMA does not pull too much power that it comprises other onboard systems. Unique mounting of an SMA can use small strains to produce larger motions, like the rotary deployment of a structural appendage using a recoverable strain of about 5-6%.

In comparison to conventional actuators, SMAs provide many benefits for space flight such as low mass and volume, high work-to-volume ratio, and a multitude of options for mounting and directional actuation. Coupled with the multiuse functionalities, SMAs are a viable choice for actuators in structural deployment.

2.2.3 SMA Mounting Mechanisms

In this section the author will discuss the methods for integrating SMAs into a structure. This includes both embedding within and mounting on the surface of the host material. Carbon composite laminates are created by embedding fibers into a matrix, and a similar method can be used to embed SMA wires, however due to the thermal dependencies of the SMA properties, precautions must be taken not to accidently cause a phase transformation during the curing process. Mounting externally is found more commonly in SMA applications as it is simpler and

the actuation can be more customized by different mounting schemes. The benefits, difficulties, and procedures for embedding and external mounting will be explored.

2.2.3.1 Matrix-SMA Embedment

Composite materials have high mechanical properties, lightness, and durability which makes these materials a great candidate for aerospace structures. Smart materials, like SMA based actuators and sensors, allow for an intelligent structure that provides shape and vibration control, acoustic control for noise reduction, and inherent structural health monitoring. The marriage of composites and smart materials through embedding of SMAs within the structure can provide advantages such as actuation and sensing in hardly accessible locations, protection of the SMA from environmental effects, and can create smart composites which improve strength, creep and fatigue properties, and damping capacity (Xu et al., 2003) (Bettini et al., 2009).

A few points to keep in mind when embedding SMAs into a CFRP is that the curing temperature of the epoxy matrices are often higher than the transformation temperatures which can cause phase transformation during the curing process, electrical insulation between the SMA and the CFRP is needed when using Joule heating, and a good bond between the resin and the SMA is necessary for high load transfer between the actuator and the structure (Bettini et al., 2009). A direct free embedding process is not possible due to the curing temperature being higher than the austenitic transformation temperatures. One solution is to use sheaths within the composite that the SMA wires would enter after the curing process had finished, and then connecting the wires externally to provide load transfer. This solution is highly invasive and increases the necessary volume of the laminate due to external features.

A solution proposed by Bettini et al. (2009) was to constrain the SMA such that no strain is recovered due to phase transformation during the curing process, there would be a transient stress created during heating, however when the material cooled back down this would vanish and the SMA would be bonded directly to the matrix without the use of external features. A Quick-Pack (QP), glass fiber reinforced plastic (GFRP) insulating sub-laminate, was used to create an electrical insulation barrier between the SMA and the host matrix. A very thin QP pre-preg was used with high resin percentage to reduce cross section dimension changes and improve adhesion of the SMAs to the plies. The thermal processes necessary for the embedment of the QP into the CFRP could create residual stresses due to the difference in CTEs, however fatigue tests of the material did not show a degradation due to the presence of the QP.

The interface analysis of these embedded SMA wires was performed using pull-out tests. The maximum interfacial shear stress (IFSS) gives the interface failure, and the average value of maximum shear stress (τ_{IFSS}), given in Equation (2.15), is obtained from the maximum recorded force corresponding to debonding (F_{max}) the fiber diameter (d), and the embedded length of the fiber (L).

$$\tau_{IFSS} = \frac{F_{max}}{\pi * d * L} \qquad \text{Eq. (2.15)}$$

The pull-out tests were performed on austenite, martensite, and martensite with hydrofluoric acid (HF) surface treatment wires. The pull-out curves are shown in Figure 2.18, where the sudden drops represent where debonding occurred.

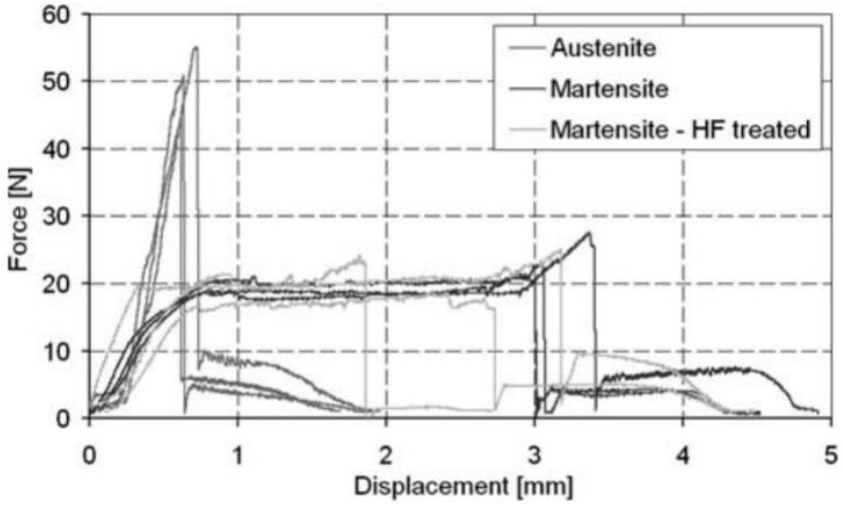

Figure 2.18: Pull-out curves for debonding of SMA in austenite, martensite, and HF treated martensite (Bettini et al., 2009).

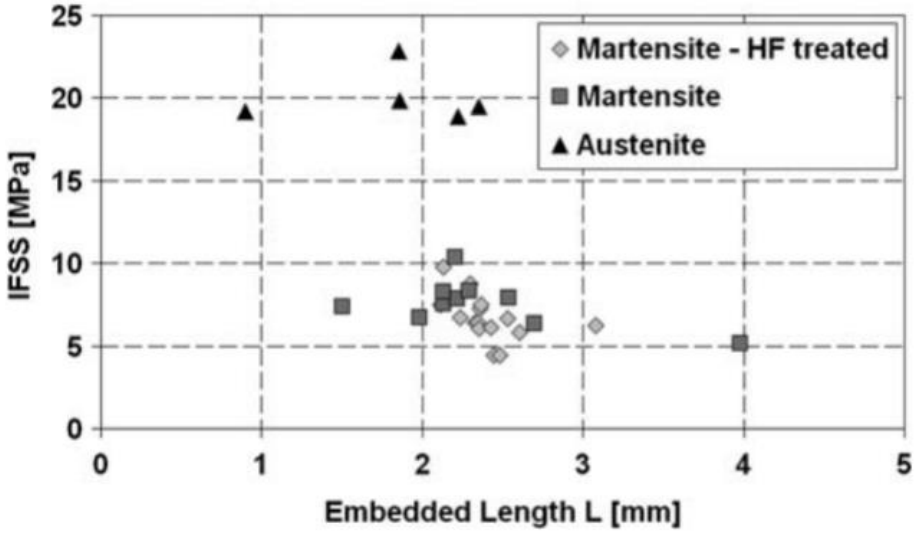

Figure 2.19: IFSS from pull-out tests of SMA in austenite, martensite, and HF treated martensite (Bettini et al., 2009).

From these results it can be seen that for martensite, the debonding occurs at higher loads than those that produce SIM, thus the plateau on the graph, and the debonding loads for austenite are much higher than for martensite. The HF treatment of martensite does not show any significant changes in results.

Figure 2.19 shows the IFSS from the pull-out tests, where the average IFSS for austenite was 20.05 MPa, for martensite was 7.59 MPa, and for HF treated martensite was 6.67 MPa. The debonding loads and IFSS show that austenite has a better bond to the host matrix than both martensite wire, and thus three times higher load transfer capability than embedded martensite for this QP embedding technique (Bettini et al., 2009).

The SMA/CFRP hybrid that was introduced in Section 2.2.2.1 did not use any special jig or equipment to embed the SMA into the CFRP matrix. Rather, Nb was introduced to NiTi to create a large transformation temperature hysteresis so that normal prepreg methods could be used to embed NiTiNb into the CFRP and still retain pre-strains after the curing process. The NiTiNb alloy had a M_s lower than -40°C and an A_s above 130°C (the curing temperature of CFRP) which was achieved through a heavy cold drawing process. Figure 2.20 shows SEM

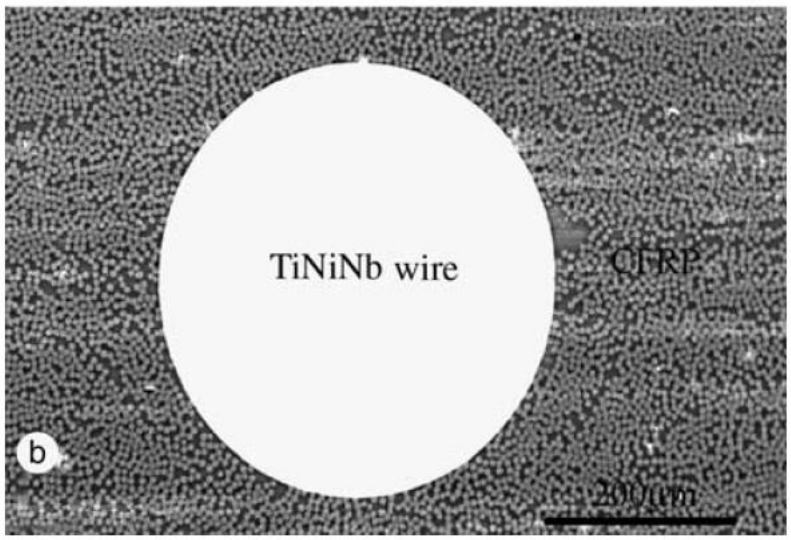

Figure 2.20: SEM image of the morphology of an SMA wire embedded in CFRP through prepreg (Xu et al., 2003).

images of the TiNiNb/CFRP composite that show no voids or pores which proves a strong bond between the SMA and the CFRP (Xu et al., 2003).

The use of embedded SMAs in composites provides benefits, however the process of embedding is difficult and requires specialized jigs, alloys, or heat treatment methods of the

SMA. The use of intelligent composite materials will be seen in the future of aerospace structures more when these embedding methods and alloys are researched and understood in more depth. Most of the current aerospace applications utilize external SMA mounting, rather than embedded SMAs.

2.2.3.2 External SMA Mounting

The definition of external mounting means not within the material of the structure as opposed to SMA embedment within a matrix, however shielding of the SMA is necessary in some applications where environmental changes may inadvertently cause phase transformations, which can lead to SMAs being mounted within a confined space. External mounting of SMAs for actuation and sensing can be seen in many of the previously mentioned applications. Although external mounting takes up more volume than embedment, SMAs still provide space saving over conventional actuators. They can be mounted as sensors, similar to strain gauges, on the surfaces of the material being monitored.

The temperature sensor example from Section 2.2.1.1 was mounted as an external feature within a mechanism. This allows the sensor to be relocated and used in many different locations. SMA wires as strain sensors, as described in Section 2.2.1.2, can act like strain gauges where they are mounted to the surface of a structure to feel the same strains as the structure. For a tube or hollow object, the SMA can be mounted on the inside surface of the structure if the outside must be smooth or unobstructed. Having the SMA be embedded within a composite can provide changes to the material property and provide a non-intrusive mounting when space saving is absolutely necessary, however the complex methods for embedding and insuring a proper load transfer can make the process infeasible especially if only the sensing function is necessary.

The most effective advantage of SMAs comes in their actuator design properties. For the actuators shown in Section 2.2.2.2, the rotary deployment device, SMATSH, and torque tube actuators are all externally mounted and provide major mass and volume saving benefits in comparison to conventional actuators. An embedded SMA actuator could be used for Active Property Tuning (APT) in the form of changing the stiffness of a composite structure through embedded SMA phase transformations, or Active Strain Energy Tuning (ASET) by utilizing the recovery stress of 'plastically' elongated SMA wires. Both APT and ASET are achieved by mounting within the composite along the neutral axis (NA), whereas mounting externally eccentrically to the NA will cause a bending moment and is referred to as Active Shape Control (ASC) (Angioni et al., 2010). ASC can be used for deployment as well as the shape control of structures that require deflections or could benefit from bending moments.

There are many examples of ASC in aerospace applications such as morphing smart wings that employ SMAs to morph the wing into the necessary shape during flight. One study achieved this through antagonistic SMA-actuated flexural structures that bend and twist to improve the aerodynamic performance of the wing. Boeing produced a variable geometry chevron (VGC) that was installed and tested on a GE90-115B jet engine. SMA actuators were used on the chevrons to change their deflection to reduce noise during take-off and increase cruise efficiency during flight. The VGC can be seen in Figure 2.21. The success of the VGC inspired the design of other ASC controlled aerospace applications such as variable engine inlet capabilities, reconfigurable rotor blades, and variable geometry fan nozzles (Jani et al., 2014).

SMA actuation has many advantages over conventional actuators, and ASC by external mounting can provide deflections and bending moments that can be utilized in deployment and variable geometry structures. The use of ASC through external mounting will be explored later in this paper as a means of deployment.

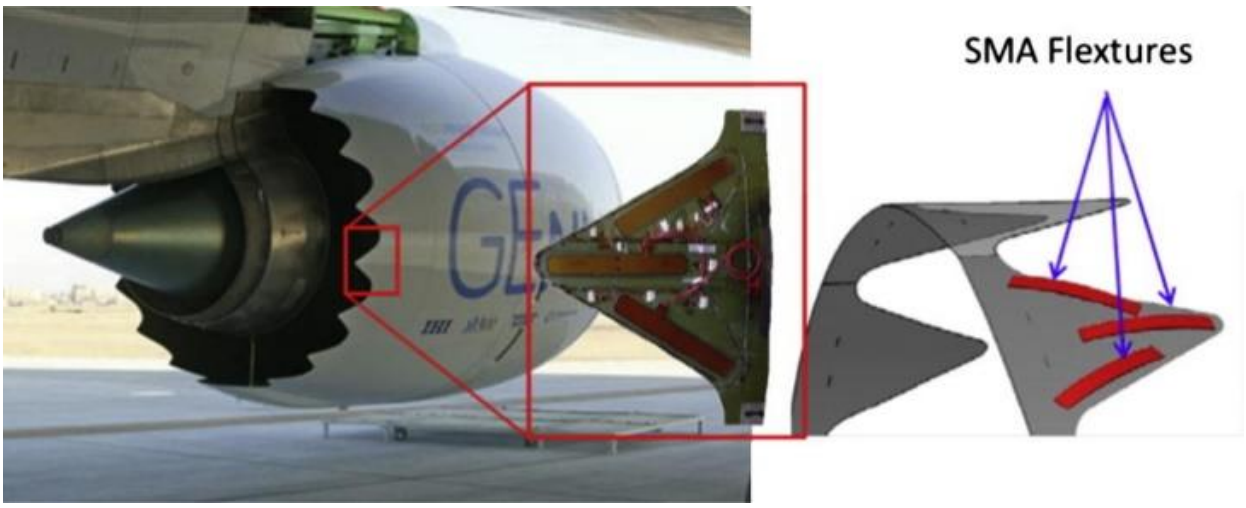

Figure 2.21: Boeing variable geometry chevron (VGC) (Jani et al., 2014).

2.3 SMA Activation

In this section the author will discuss the methods of inducing the SME through heating. Due to its alloy composition, the SMA conducts electricity and can be heated using its own ER. This method is called Joule heating and will be the main focus of this section. The electrical requirements for Joule heating will be outlined and methods for controlling the heating process will be explored. Alternative methods of heating such as conductive and radiative will also be touched on.

2.3.1 Joule Heating

In order to utilize the SME and produce a phase transformation, temperature control of the SMA must be possible. Normally for a SMA actuator, the material starts in de-twinned martensitic phase with a pre-strain which creates a recovery force when heated back into the

austenitic phase. There are multiple ways of heating, and one of the most common is using electrical heating of the alloy, also known as Joule heating. Due to the nature of SMAs, certain temperatures must be reached in order to start and finish phase transformations. The following equation can be used to calculate the estimated current needed to reach a specific temperature T within the wire:

$$I = \sqrt{\frac{T - T_{amb}}{4\rho} * (\pi^2 * d^3 * h)} \text{ Amps} \qquad \text{Eq. (2.16)}$$

In Equation (2.16), T_{amb} is ambient temperature, ρ is the resistivity of the wire, d is the diameter of the wire, and h is the heat transfer coefficient which varies due to orientation and environment. Rao et al., (2015) use a thermal web wizard ("M. Simulation", 2004) to approximate a heat transfer coefficient. The time to heat to this temperature can be estimated using the following equation:

$$\Delta t = \frac{\rho_m(C_p \Delta T + L)}{-\frac{4h(T_{avg} - T_{amb})}{d} + \frac{16I^2\rho}{\pi^2 d^4}} \qquad \text{Eq. (2.17)}$$

In Equation (2.17), ρ_m is the density, C_p is the specific heat, ΔT is the change in temperature, L is the latent heat, and T_{avg} is the average temperature. This equation makes many assumptions so it is more of an approximation on the order of magnitude of the time needed rather than exact. It is also important to note that the cooling process of the wire takes into account many more factors and this equation should only be used to approximate heating times (Rao et al., 2015).

SMAs can be heated very quickly with a sufficiently large current, however currents over a certain magnitude can easily overheat the SMA and cause permanent damage if left on for too long. Any application of Joule heating must take steps to avoid overheating. Most commercial

suppliers of SMAs will provide safe current values on their data sheets that can be used to safely heat and actuate the SMA for a given amount of time. A method to mitigate the overheating effect of constant current was defined by Kuribayashi where if the SMA is below a certain temperature threshold, use a high current, and if the SMA crosses above the threshold, use 0 current (Featherstone & Teh, 2004). This process simulates a pulse-width modulated (PWM) signal, which is another proposed option for controlling the heating of an SMA wire.

SMAs have already been shown to have differing ERs depending on strain, however the different phases can cause ER to change by about 20%. A model relating the electrical resistivity to the martensite fraction can be found in the work by Cui et al. (2010) which is based on a model using the rule of mixture of the martensite fraction by Ikuta et al. (1991). Due to thermal hysteresis, the actual temperature of the wire cannot be deduced, however a threshold ER can be defined. This R_{thresh} can be utilized similar to the threshold temperature used in the Kuribayashi

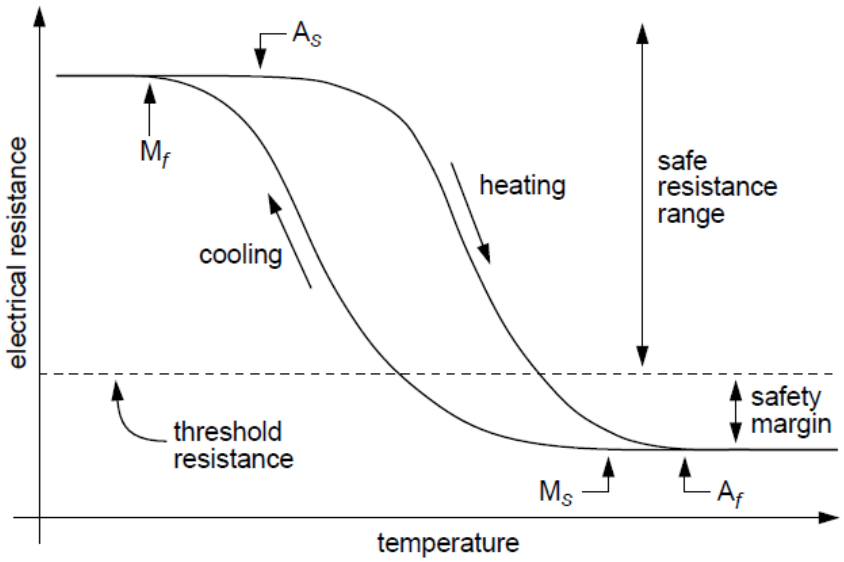

$$I_{max}(R) = \begin{cases} I_{high} & \text{if } R \geq R_{thresh} \\ I_{safe} & \text{otherwise.} \end{cases}$$

Figure 2.22: (above) ER vs Temperature (below) Electrical current relationship with ER (Featherstone & Teh, 2004).

method to control the applied current to the wire. A safety margin should be applied to account for measurement errors, strain-induced ER changes, and batch SMA variations. When ER is above or equal to $R_{thresh,}$ the current should be at $I_{high,}$ otherwise current should be at $I_{safe.}$ This concept can be visualized in Figure 2.22, where the heating and cooling of the SMA changes the ER as the phase transformations occur. The current applied to the wire, $I_{max,}$ is a function of ER and creates a step-wise graph as the temperature variation induces phase transformations. This step-wise graph, like the Kuribayashi method, is similar to a PWM signal (Featherstone & Teh, 2004).

Furst & Seelecke, (2012) proposed a PWM based power supply method to control the total power into the wire remains constant as the ER of the SMA wire changes. This is achieved by pulsing a current wave with ~1 kHz frequency while changing the duty cycle, depending on the measured ER, every millisecond. The heating and cooling effects of the wire take time to propagate so the millisecond pulses do not affect the wire directly, but rather the average of all the pulses does. The amplitude of the current pulse is kept constant, so the voltage is measured during each pulse and the ER of the SMA wire can be calculated. Depending on the ER, which tells the phase of the wire, the duty cycle of the current pulse is updated, thus ensuring the total power going into the wire stays constant (Furst & Seelecke, 2012).

The last Joule heating paradigm that will be discussed is using a capacitor to apply a significantly large current in a very short time, such as >3000A in ~10 ms, to heat the SMA wire. Traditional power sources would not be able to provide these currents so a capacitor is used. This impulsive current surge will also provide a shorter response time of the SMA actuator. The energy that is required in order to finish a phase transformation, E_t, is given in Equation (2.18). In this equation, E_h is the energy needed for raising the temperature, E_p is the energy needed for

phase transformation, m is the mass of the SMA, μ is the energy needed for phase transformation per unit mass, λ is specific heat, and ΔT is the temperature increment from ambient to A_f.

$$E_t = E_h + E_p = m * (\lambda * \Delta T + \mu) \quad \text{Eq. (2.18)}$$

The response time of the actuator, meaning the time it takes for full transformation, is given in Equation (2.19). This time is dependent on R, C, and V_0. R is the sum of the ER of the SMA, R_a, the ER of the capacitors, R_c, and the ER of the cables and joints, R_w. C is the total capacitance of the capacitors, and V_0 is the initially charged voltage of the capacitors.

$$\tau = -\frac{1}{2} RClog(1 - \frac{2RE_t}{R_a C V_0^2}) \quad \text{Eq. (2.19)}$$

Finally, the current from the discharged capacitors can be expressed by Equation (2.20) (Qiu et al., 2001).

$$I = \frac{V_0 e^{-\frac{t}{RC}}}{R} \quad \text{Eq. (2.20)}$$

2.3.2 Other Methods of Activation

Joule heating can be efficient because for a system that already incorporates a battery, a small portion of its storage can be used to actuate the SMA element without the need of external heating elements. However, as the SMA wire's diameter increases, the current required to cause phase transformation can become excessive so options like a heating patch, conductive fluid immersion, or solar heating can be more feasible (Rao et al., 2015).

Conductive and radiative heat transfer, such as heating patches and microwave or infrared light respectively, depend on a heat gradient which can be inefficient. These sources heat on the surface of the SMA, and causes thermal mismatches within the material. With a large enough conductive heat transfer power rate, the temperature gradient can become so large that the temperature on the surface of the actuator could exceed the melting point of the material

(Huang et al., 1996). Using the Sun's heat to induce a phase transformation in the SMA is an interesting and clever application of environmental stimuli, especially in space applications, however this requires control over the attitude of the PA and as the system orbits the Earth, the sun will not always be visible.

Some SMAs have the capability of being heated through oscillating magnetic fields, which induce eddy currents and simulates Joule heating. The magnetic field can penetrate metal so that the SMA actuator is uniformly heated. For paramagnetic materials, a very strong magnetic field is required to generate the necessary response. Increasing the frequency of the magnetic field can increase the heat generation, however this makes it more difficult for the magnetic field to penetrate the SMA. A major deterrent for this method of heating is the necessity for a large electromagnet and related equipment for the generation of the magnetic field (Huang et al., 1996). This mass addition contradicts the goals of the PA paradigm, and is therefore not viable for this application.

It is important to note that one major challenge in using SMAs is the low operational frequency and narrow bandwidth of SMA materials. These alloys have relatively high heat capacities and densities, so it is difficult to transfer heat rapidly into and more importantly out of the heated SMA. The most major concern in bandwidth limitation is the lengthy cooling process. SMA actuators with smaller diameters heat faster due to higher resistivity, and cool faster due to higher surface-to-volume ratio; so changing the wire diameter can drastically change the SMA bandwidth. Some additional methods for cooling include forced air, flowing liquids, thermo-electric modules, heat sinks, and other conductive materials (Jani et al., 2014). This may be a major concern for repeated actuations, however for an application where the actuation function is

only being used once, such as the deployment of a PA, the cooling process is not as significant of a concern.

CHAPTER 3: Development of Autonomous Truss Module

3.1 3D Printed Truss Models

Part of the work at the ISA Lab at NASA LaRC is designing and creating prototypes for truss module packaging and deployment. Although most of the work has been conducted on tri-truss modules, due to the simplicity of the cubic truss deployment, this paper will primarily focus on the integration of SMAs for deployment and sensing of the cubic truss joint. That being said, a short overview of some tri-truss designs will be given.

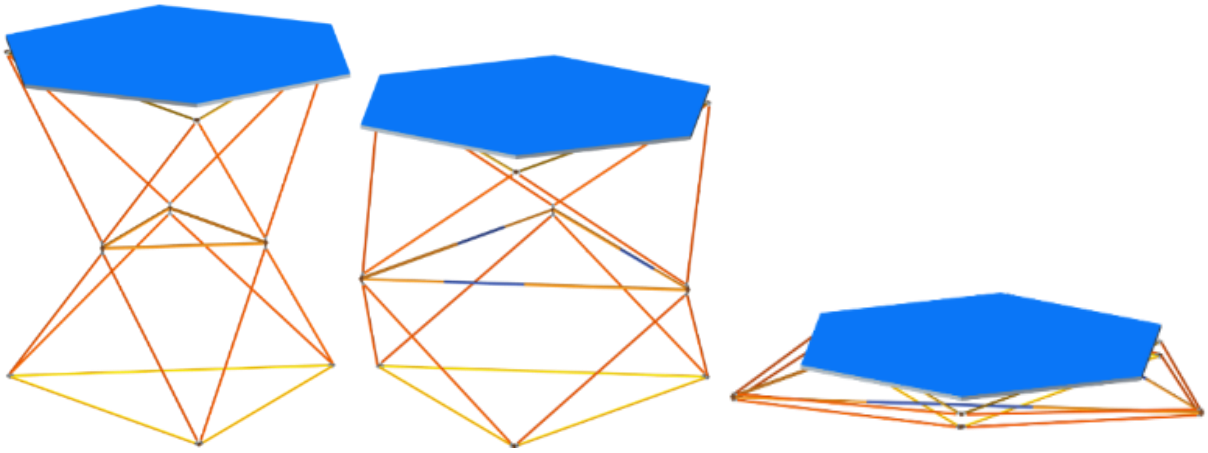

Figure 3.1: Telescoping Middle Tri-Truss Packaging Sequence from left to right.

The telescoping middle tri-truss, one of the first tri-truss packaging and deployment designs, is shown in Figure 3.1. A hexagonal mirror panel is included to show the pre-installation capability for telescope applications. The sequence shows the packaging concept from left to right, where the middle plane triangle expands to allow the side planes to fold in half. The resulting packaged module has a hexagonal shape and a ~95% height reduction. The initial idea was to run an SMA wire through a middle triangle plane member, however the length this member gains is much larger than any strain an SMA could handle. Most SMAs have a strain

recovery of ~4-10%, and the middle trangle plane member telescopes from 40 inches to 108 inches meaning a strain of 170%. This realization redirected the SMA integration to more of a hinge feature to monitor a small section of the truss, rather than an entire strut.

Another preliminary concept for the Telescoping Middle Tri-Trss is shown in Figure 3.2.

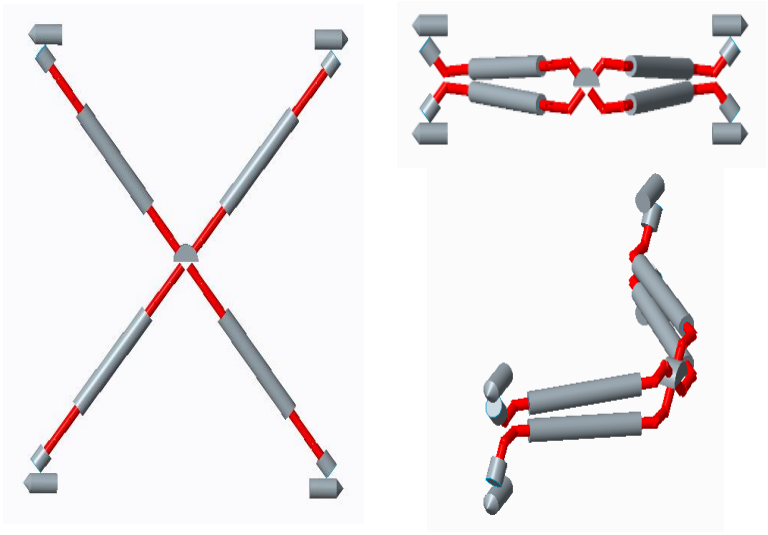

Figure 3.2: Representation of Side Plane of a SMA Tri-Truss.

This figure shows one side face of the the tri-truss and how it would fold when the middle triangle expands out. The red portions represent where the SMAs would be located. Unlike the hinges in the previous design, the SMAs can be bent in multiple dimensions allowing for a multi-DOF hinge. This means that the whole tri-truss can fold down more efficiently, with less expansion in the middle triangle, and thus fit within the payload fairing without sacrificing the depth of the structure. Placing the SMAs as such puts them in the load path of the side plane members, which is beneficial for the sensing application of SMAs, however the Young's modulus difference between the alloy and the adjacent truss material can greatly affect the stiffness of the structure. As was stated previously, the intent is to have each of the static truss components be made of a carbon fiber composite. Carbon fiber composites can have moduli on the order of ~350 GPa, whereas Nitinol in the low stiffness martensitic phase has a modulus of

~35 GPa and in the high stiffness austenitic phase had a modulus of ~80 GPa. The order of magnitude difference eliminates SMAs from being mounted as a primary load bearing member on the truss due to the need for high stiffness in-space telescope applications.

In early to mid-2020 a Tri-Truss trade study team analyzed and narrowed down deployment and packaging designs using comparison metrics such as geometric versatility, kinematic complexity, etc. The Telescoping Middle Tri-Truss was one of the contendors in this study, however it was eliminated from consideration primarily due to the necessary reduction in depth to fit inside of the proposed payload fairing. One of the designs that was chosen for further analysis was adopted as the main tri-truss for SMA integration. This tri-truss is called the Camping Chair. This concept was chosen for its packaging efficiency and lack of telescoping members. Instead of telescoping members, the Camping Chair design has 42 rotational single DOF hinge joints. These joints are great mounting locations for SMA actuators/sensors because

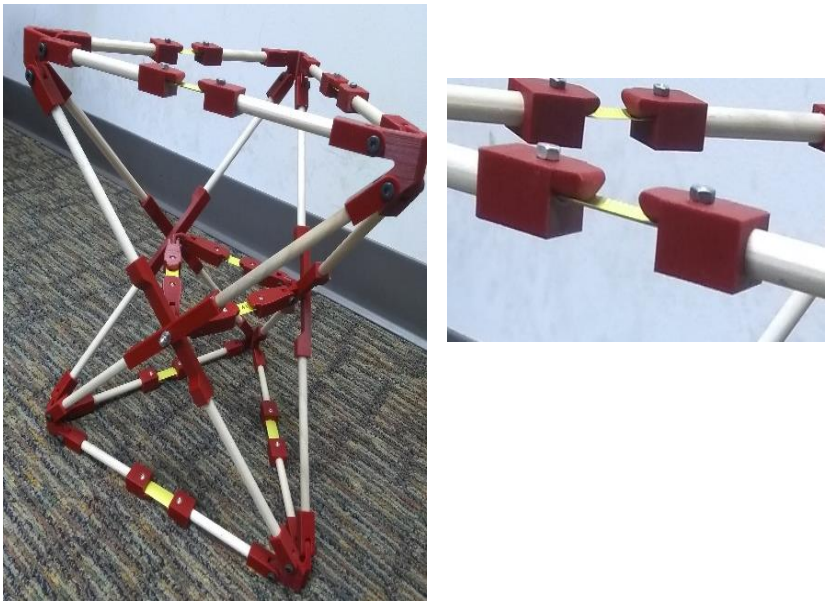

Figure 3.3: Camping Chair design with Strain Energy Hinges.

the SMAs can directly actuate on the hinge as well as monitor the weakest points on the

structure. The reason these are the weakest points are because of the addition of a degree of freedom from each hinge.

A second iteration of the Camping Chair design included strain energy members integrated in the hinges to help with deployment. A table-top model of this design concept is shown in Figure 3.3. Using SMAs in tandem with the strain energy hinges can create a similar mechanism as the SMATSH.

Table-top models of all the designs considered by the Tri-Truss Trade Study team were created, however the designs that were chosen by the Trade Study team will be scaled up to models created with more reliable materials. The original models were made using CAD designs and 3D printers for the joints and hinges, wooden dowel rods as static struts, and measuring tape and straws as the strain energy members. For the second Camping Chair design, a measuring tape was cut up and used as a tape spring strain energy member at each strut hinge. For the scaled up model, a novel carbon composite strain energy member that was developed at NASA LaRC is being considered for use. This carbon composite strain energy member was developed for the use as a coilable boom, which would be rolled up in the packaged state and have a high stiffness in the deployed state. This technology can be adapted to fit the high stiffness requirements of a space telescope truss module.

The cubic truss has a simplier deployment and packaging concept, however the hinge joint itself is analogous to the hinge of the Camping Chair design; the difference being the angle travelled during deployment. The Camping Chair design has hinges that must fold 90° or 180°, depending on their location on the truss, whereas the cubic truss hinge must fold 45°. Due to the similarity of the hinge joints, the mounting of the SMA actuators/sensors will be analogous as well. The slight differences in dimensions of the hinges will affect the pre-strain of the SMA,

however this will be tuned through the specific length and mounting of the SMA wires. A preliminary joint that was designed and manufactured can be seen in Figure 3.4. This cubic truss joint design incorporates a tape spring to provide strain energy to the deployment process. The

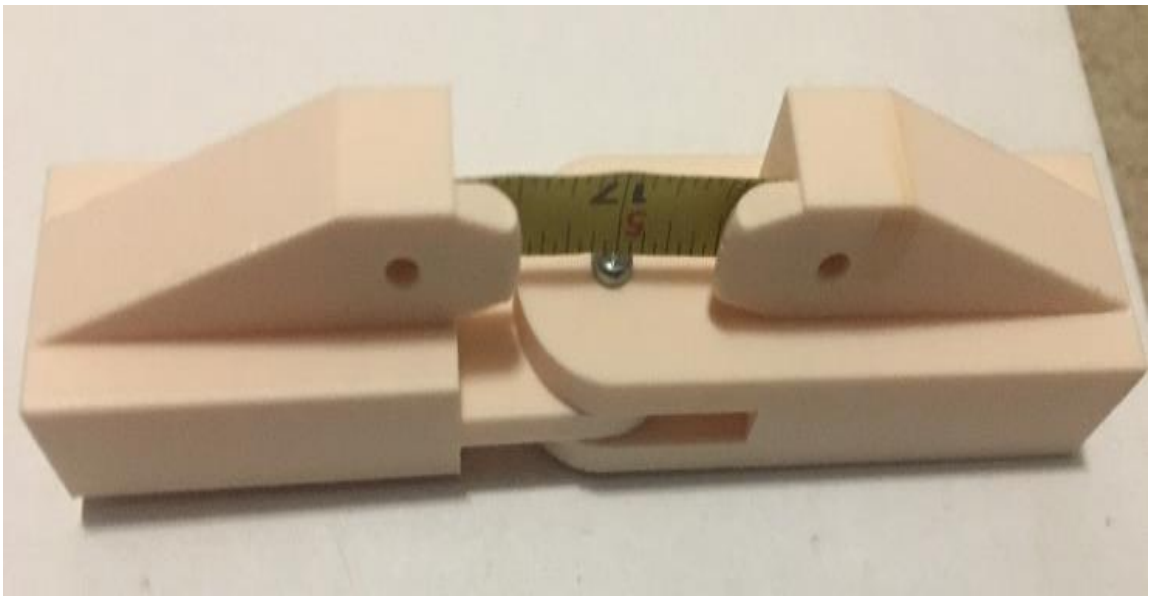

Figure 3.4: Preliminary Cubic Truss Joint with Strain Energy Member.

tape spring crosses right over the axis of rotation, signified by the silver screw head, and guides can be seen protruding from the tape spring mount to keep the tape spring from bending too sharply and damaging the material. The tape spring for the cubic truss joint was the same material used for the Camping Chair design.

3.2 Actuation Methods

In this section the author will introduce the design for a multi-functional SMA truss hinge joint. A method for tuning the pre-strain of the SMA will be explained, and the relationship between SMA mounting and pre-strain will be explored. An alternative design including a strain energy member will also be introduced, however this design is reserved in case the SMA wires are not capable of fully actuating the hinge joint. In the alternative design the SMA acts as more of a damping mechanism that provides control to the chaotic deployment of the tape spring.

3.2.1 SMA Actuation

The integration of the SMA into the cubic truss joint as an actuator and sensor was meant to negate the need for additional deployment mechanisms, such as strain energy members, and thus reduce the parasitic mass for each deployable joint. The SMA will deploy the hinge joint by using its axial pull force from the recovery stress produced by the martensitic to austenitic phase

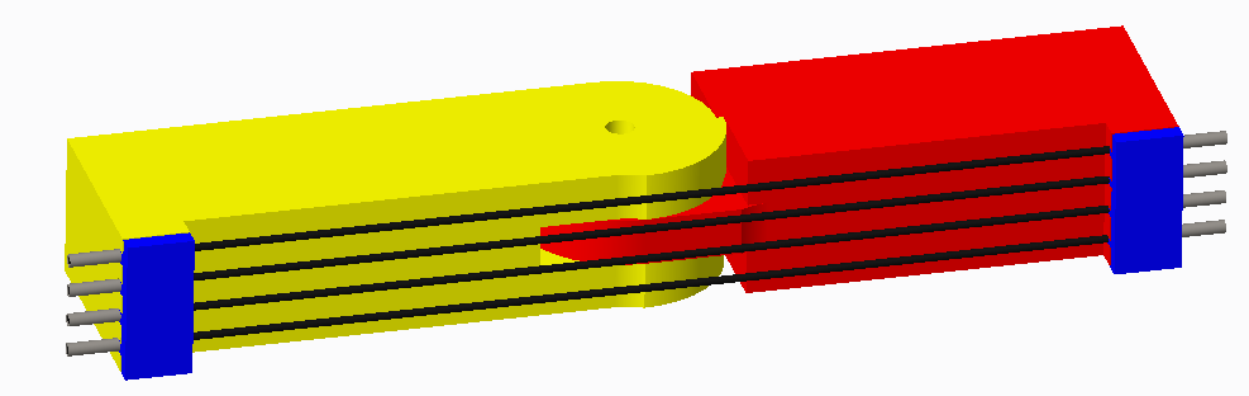

Figure 3.5: SMA Actuated Cubic Truss Joint.

transformation. Figure 3.5 shows the design for the SMA actuated cubic truss joint in the deployed configuration. The SMA wires are shown in black, and are mounted on the side of the joint in order to sense the strains across the joint as well as provide a deployment moment. The multiple wires were included to show the maximum number of wires that can be fit on this specific prototype. Multiple wires can be mounted to increase the pull force and therefore the deployment moment. The SMAs are mounted using ferrules at the ends of the wires which will be crimped. These crimps will provide an electrical connection and the ferrule will be locked into the slot using a friction fit from the ferrule cover shown in blue. Mechanical stops were built into the design to block the joint from rotating in the opposite direction of actuation, which may occur due to the existence of a pre-strain in the deployed configuration. The mechanical stops also act as rotation guides for the SMA, to guide the SMA in a circular path around the hinge axis. Teflon tubes or sheets can be used to act as an insulator between the SMA wires and the

structure. The insulation will be necessary for preliminary tests since the heated wires can cause damage to the 3D printed plastic parts. The distance of the wire from the central axis of the joint is used to determine the pre-strain of the SMA when in the packaged configuration.

Figure 3.6 shows a top view of the cubic truss joint in order to explain the pre-strain tuning due to SMA mounting. The blue point is the hinge axis, the green line is the NA through the joint, and r is the distance from the NA to the SMA. The elongation, ΔL, is a function of both

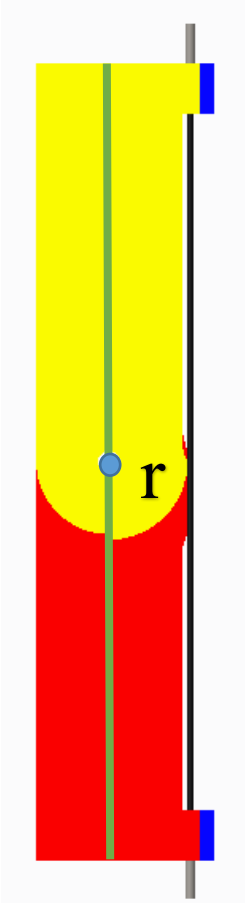

Figure 3.6: SMA Cubic Joint Top View.

r and the rotation of the hinge joint, θ, and this relationship is:

$$\Delta L = (2\pi r) * \frac{\theta}{360°} \qquad \text{Eq. (3.1)}$$

The strain % is then:

$$Strain\ \% = \frac{\Delta L}{L} * 100\% \qquad \text{Eq. (3.2)}$$

Where L is the original length of the SMA. For the cubic truss joint prototype, the SMA is designed to have a length of 200 mm and the rotation is 45°. For the analogous SMA tri-truss

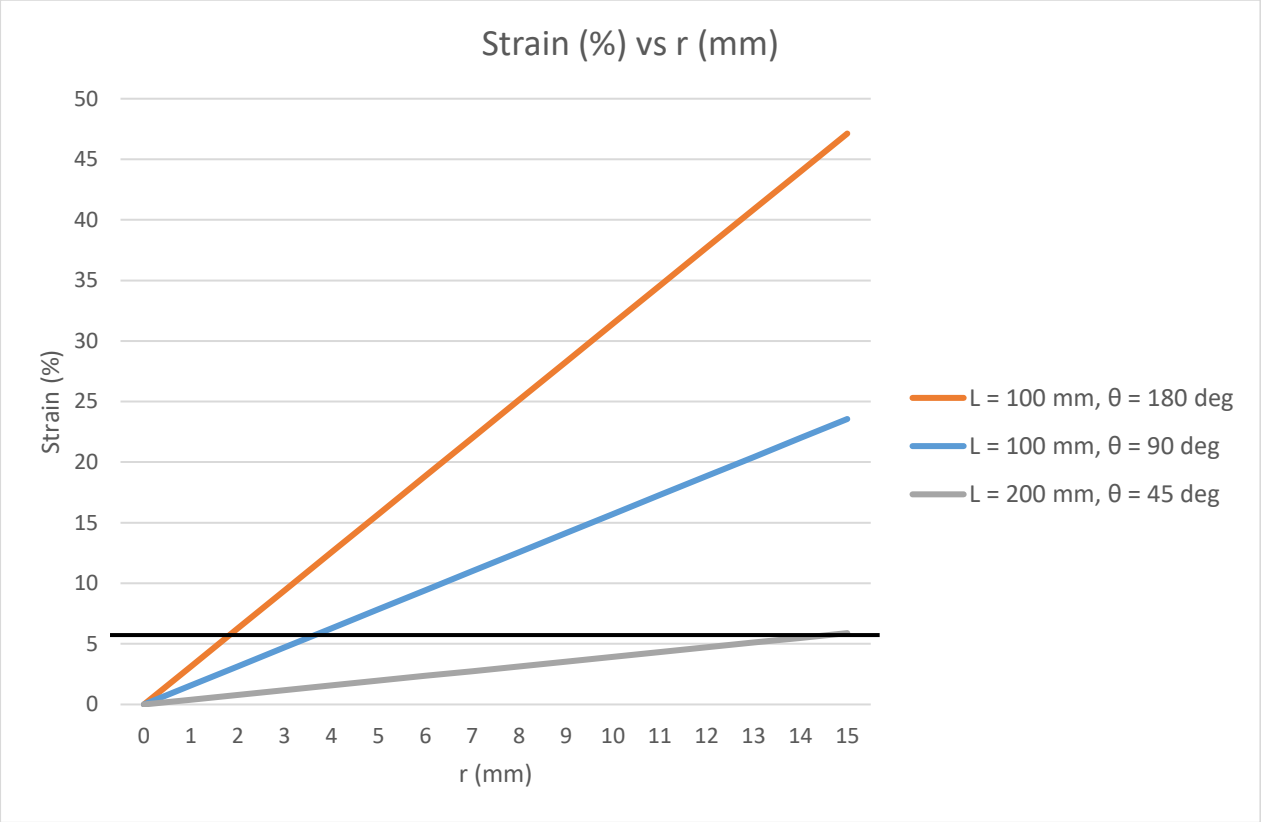

Figure 3.7: SMA Pre-strain vs r.

hinge joint, the SMA length is 100 mm and the rotation will be 90° and 180° depending on the location of the joint. Using these values, the pre-strains for each joint were graphed as a function of r and are shown in Figure 3.7. The black line signifies a pre-strain of 6%. For this specified pre-strain, r for the cubic truss joint must be ~15 mm. The reason the tri-truss SMA lengths are much shorter is because the current model is a table-top version, whereas the cubic truss joint is closer to the actual truss size. The size of r can be tuned by changing both the thickness of the joint and the distance the SMA is mounted from the center. For the current prototype, the 200 mm length of SMA is mounted 15 mm away from the NA of the joint to produce a pre-strain of

~6% when the joint is packaged at a 45° angle. As the tri-truss model is scaled up, the length of the SMA will increase, and the slope of the Strain vs r graphs will decrease. This will increase the necessary r value for 6% pre-strain and provide more flexible mounting options of the SMA.

This r value is also used to calculate the moment the SMA creates when heated. Due to the fact that the axial pull force is acting a distance r from the NA and the SMA is attached to a rigid member in line with the hinge axis, the moment can be calculated as the pull force multiplied by the distance r from the NA. The actual pull force of the SMA wire is currently unknown due to the lack of information about the specific SMA. This required parameter will be determined from a pull-force test that will be described in more detail in Section 3.4.

3.2.2 SMA Deployment Aid

Aside from being the sole method of deployment, the SMA can also work in tandem with a strain energy member, such as a tape spring, to control the deployment behavior. As was discussed before for the SMATSH, the SMA can control the chaotic deployment of a tape spring to reduce shocks introduced during deployment. Figure 3.8 shows the integration of a tape spring into the joint.

The tape spring, in green, is in line with the central axis of the joint, and the bending point of the tape spring is coincident with the hinge axis so that it does not feel any strains when packaged. The addition of the tape spring mount does change the cross-section of the joint, thus changing the strain response, however the tape spring is not able to be mounted on the side because it can not be strained like the SMA can.

This SMATSH design is an alternate option in the case additional deployment force is necessary, especially for the final leg of deployment where the SMA may not be able to fully straighten at the end of the phase transformation. The tape spring has a neglible mass, however the mounting features will add considerable mass and volume to each deployment hinge joint. Although this addition of parasitic mass is not desired for the PA paradigm, the cooperation of an SMA with a tape spring may be necessary for complete deployment.

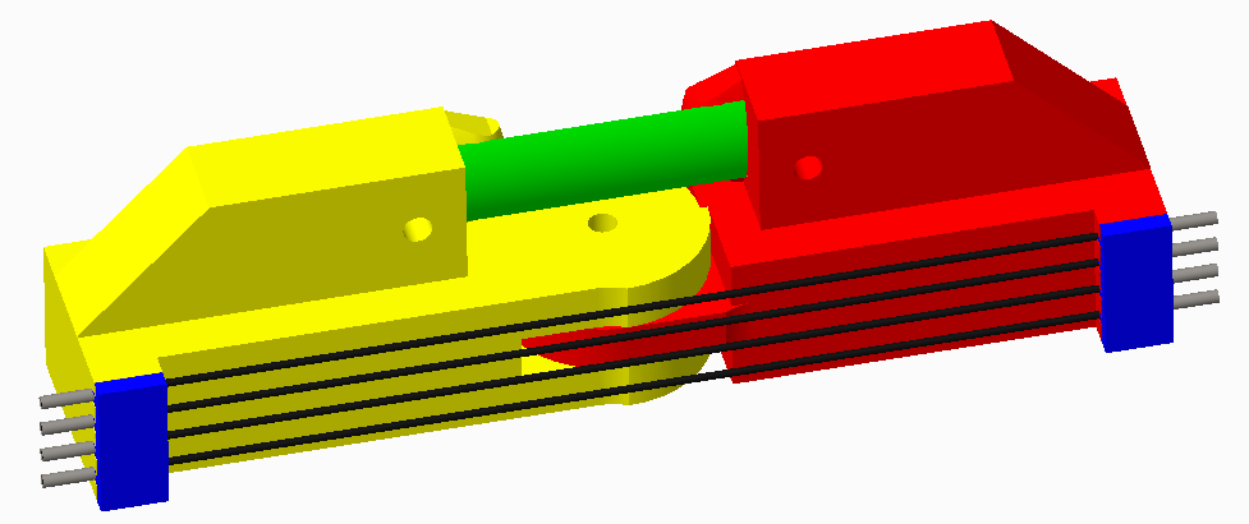

Figure 3.8: SMA Cubic Hinge Joint with Tape Spring.

3.3 Strain Sensing

In this section the author will discuss the sensing function of the SMA truss hinge joint through the piezo-resistive effect. The sensing function for composite materials will be validated using past studies. Wires have a poor performance under compression, the compressive buckling failure will make it difficult for an SMA wire to remain within the load path. A simple solution for the difficulty of sensing compressive strains using a wire will be introduced. The thermal dependency of SMA's ER can create noise that obscures the piezo-resistive effect. A method for compensating for this from previous literature will be applied to the SMA hinge joint.

3.3.1 SMA Electromechanical Sensing

Once the deployment of the structure has finished, the SMA will switch functions to a pure sensing element. The SMA is attached to both ends of the joint and will be able to sense strains across it. This will be done by measuring a baseline ER of a known strain and then monitoring the change in ER across the wire. Using multiple wires in parallel for the sensing function provides redundancy if one of the wires becomes damaged at any point in the truss modules lifetime. Equation 2.5 shows the relationship that will be used to calculate the strain, and Figure 2.7 portrays the viability of this method.

The carbon composites that are being considered for the truss modules have high moduli ranging from 91-270 GPa, and from preliminary tests they failed at only fractions of a percent of strain in both compression and tension. It is important to note that some of these loading tests had failures in the end fittings as well as issues with displacement measurements, so more reliable tests will have to be run with the carbon composite tubes in order to characterize their strain characteristics before failure. Even though the strains are at low values before failure, Figure 2.7 shows a 1% change in ER variation at a value of 0.6% strain. Although small, there is still a measureable change in ER which has an easily calculated linear relationship with the strain.

Since the SMAs are in the form of wires, they act much more reliabily under tension than compression. Buckling failure of the SMA wire would typically not allow the alloy to sense compression loads, however a solution to this is in the pre-strain of the SMA. By integrating a pre-strain of 1% into the SMA wire when it is in the sensing configuration, any compressive strains will decrease the pre-strain and cause a noticeable change in ER. The total pre-strain of

the SMA wire will be the sum of the strain needed for deployment and the strain included to measure compressive loads.

3.3.2 SMA Thermoelectrical Noise Elimination

The ER variation relationship with temperature variation can cause problems in the accuracy of readings from the SMA sensor. The ER variation noise that is created from temperature changes may mask the desired ER variations due to strain, especially for the small strains expected from carbon fiber composites, so this temperature dependent relationship must be accounted for. This will be accomplished by using the compensation method introduced in Equation 2.9.

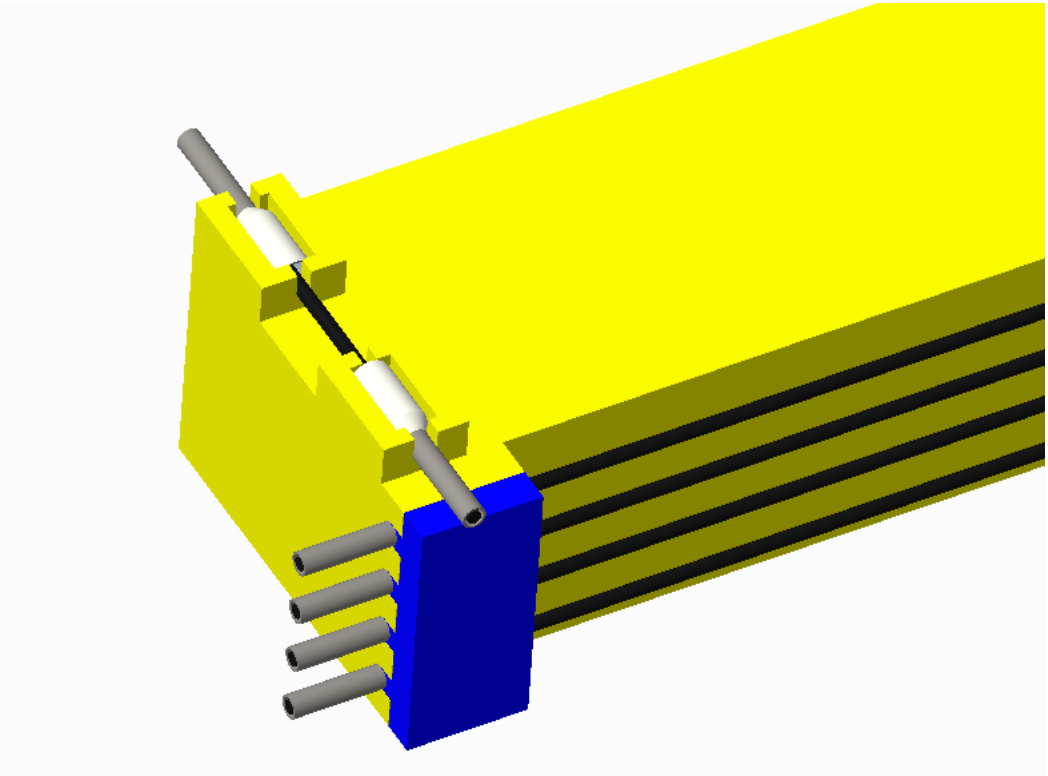

Figure 3.9: SMA Cubic Joint Reference Wire.

A smaller reference wire will be used along with the SMA actuator/strain sensor; this reference wire will be mounted such that it does not experience the strains across the joint, but will be at the same ambient temperature as the SMA sensor wires. If the ER is measured at a

baseline temperature, the ER variation in the reference wire can be used to quantify any changes in temperature and this data can be used to then compensate for temperature dependent ER variation in the SMA sensor. The reference wire will have to be mounted such that it is not parallel to the load path, and this can be achieved by mounting the wire perpendicularly on the joint. Figure 3.9 shows a potential mounting location of the reference wire. It can be observed that the reference wire is much shorter than the sensing wires, and although this does change the ER of the reference wire, the variation of ER due to temperature changes is the same for both sets of wires. The ferrule covers were left off in this image to show how the ferrules are mounted.

3.4 Tests and Simulations

As the SMA materials were being ordered, the COVID-19 pandemic caused the ISA lab, where these tests were meant to be run, to shut down indefinitely. Due to the lack of a workplace and necessary supplies, it was not possible to conduct the following tests. The specific SMA material ordered was 10 feet of 1.0 mm diameter Nitinol wire from Amazon.com, (2020). This SMA only provided a transition temperature of 80 °C, however did not specify if this was As or Af . The supplier was contacted for a technical data sheet for the SMA, however the supplier replied that no data sheet was available. After looking further into the manufacturer of the SMA, it was found that the temperature provided was “an approximation of where the alloy begins to undergo the crystalline transformation” which is also known as A_s (Nexmetal Co., 2020). An alternative Nitinol wire that is used in many academic papers is called Flexinol and is produced by Dynalloy, Inc. Dynalloy provides a data sheet with physical properties that can be used to more reliably predict the response of the Flexinol than the Nitinol sourced for Amazon.com (Dynalloy, Inc., 2020). This section will highlight some tests that have been designed for the

SMAs and the hinge joint prototypes. The 3D printed designs were created with PLA plastic, so their stress-strain behavior will differ greatly from the ultra-high modulus carbon composites, however as the concept is verified with less stiff materials, more robust prototypes will be created and tested.

3.4.1 SMA Material Properties

The first set of tests that are planned to be run are to characterize the SMA material. Due to the lack of a data sheet, many of the material properties needed for simulations and hypotheses are missing. For the sensing application, the ER must be measured in the martensitic phase of the SMA. This can easily be achieved using the Ohmmeter function on a Multimeter. Knowing the baseline ER will be useful in further tests which use the variation in ER as the sensing function.

Another important material property to know for the SMA is the stress-strain response. This data will provide important information about the strength of the material, as well as the apparent Young's moduli in each phase. This test can be performed using one of the MTS universal testing machines (UTMs) located in the lab at NASA LaRC along with a micro-load cell and a linear variable differential transformer (LVDT). One method of simulating the stress-strain curve is using the 1D constitutive model shown in Equation (3.3).

$$T_1 - T_1^0 = Y\ (S_1 - S_1^0) + \Omega(\xi - \xi^0) \qquad \text{Eq. (3.3)}$$

In this equation, $T_1 - T_1^0$ is the change in stress, Y is the Young's modulus, $S_1 - S_1^0$ is the change in strain, $\xi - \xi^0$ is the change in martensite fraction, and Ω is the transformation coefficient. The transformation coefficient can also be represented by Equation (3.4).

$$\Omega = S_L Y \qquad \text{Eq. (3.4)}$$

S_L is a material property known as the maximum residual strain. It is important to note that this model works for 1-D tensile stress along the axial direction, so it neglects all other strains as well as thermal expansion.

The Young's modulus of the SMA is different in the austenitic and martensitic phases; the high temperature austenite phase is stiffer and thus has a higher modulus. The modulus of the SMA is not well defined during the transition between martensite to austenite and vice versa. Two models that were defined as upper and lower bounds of the modulus are shown respectively in the following equations (Bhaskar et al., 2020):

$$Y(\xi) = \xi Y_M + (1 - \xi) Y_A \quad \text{Eq. (3.5)}$$

$$Y(\xi) = \frac{Y_A Y_M}{\xi (Y_A - Y_M) + Y_M} \quad \text{Eq. (3.6)}$$

The upper bound is known as the Voigt scheme (Auricchio & Sacco, 1997) and the lower bound was developed in the work of Auricchio et al., (2007). Each expression makes different assumptions of the crystal orientation of the austenite and martensite phases within the SMA, however for this paper the Voigt scheme, Equation (3.5), will be used for simplicity.

Using the previous Figure 2.1, shown here as Figure 3.10, the simulation of the stress-strain curve begins with the aforementioned initial conditions at the bottom of the graph between

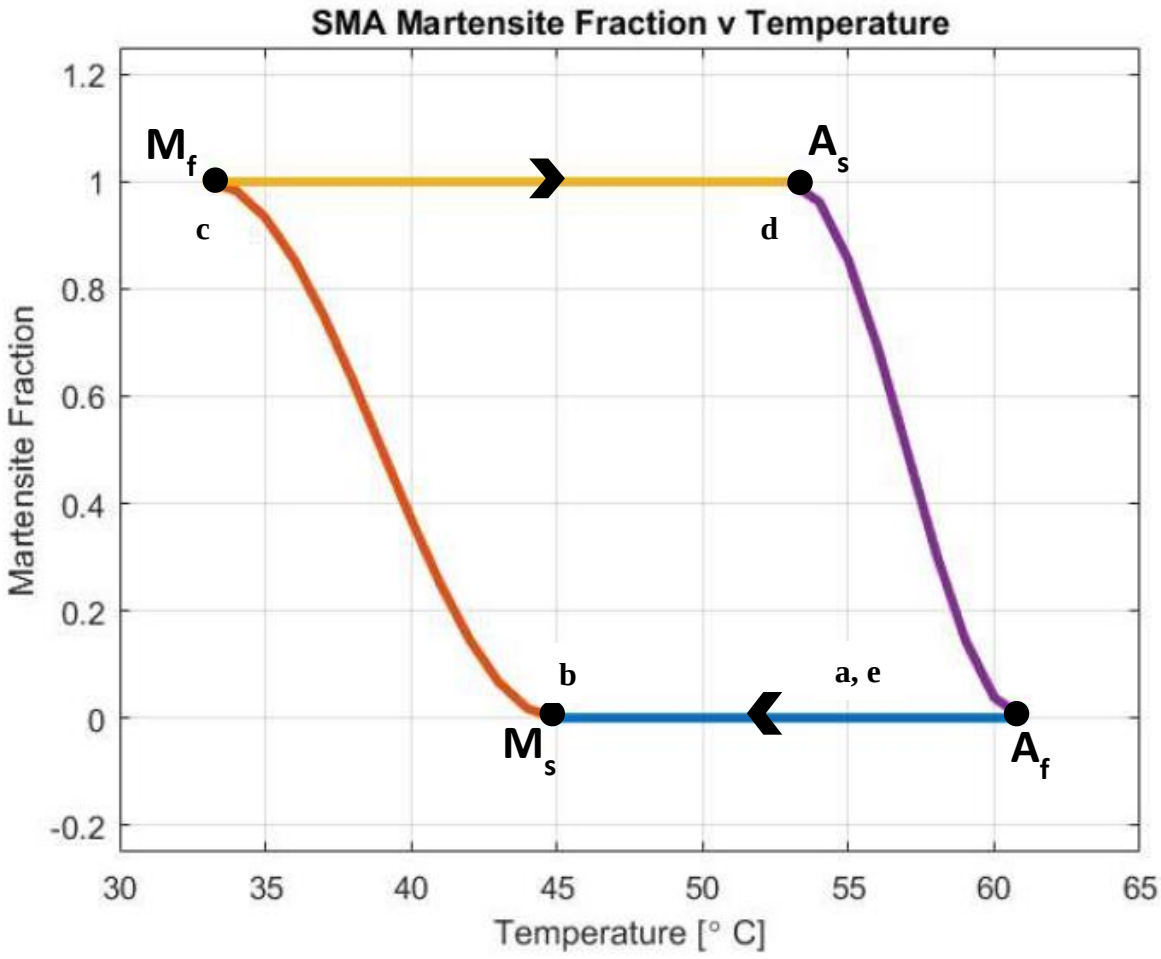

Figure 3.10: Martensite Fraction vs Temperature.

M_s and A_f. To start this simulation, the initial conditions are T=S= ξ=0 at point a, and the temperature of the SMA, θ, remains constant where: $M_s < \theta < A_f$. The transformation temperatures are all functions of stress, so as T varies, the new transformation temperatures, represented with an asterisk, e.g. M_s*, M_f*, etc., will equal θ at some point in the stress variation. This can be envisioned by placing a line at θ, and imagining the graph moving side to side in reference to the constant temperature as the stress varies. Now moving from the initial

conditions, a, to the start of the martensite formation, b, the stress-strain curve is a linear relationship where:

$$T^{a\to b} = Y_A S \quad \text{Eq. (3.7)}$$

The stress at which martensite starts forming, T^b, is calculated using the material property known as the martensitic stress rate or coefficient of stress influence, C_M, and is defined as:

$$T^b = C_M(\theta - M_S) \quad \text{Eq. (3.8)}$$

The strain at this point is:

$$S^b = \frac{T^b}{Y_A} = \frac{C_M}{Y_A}(\theta - M_s) \quad \text{Eq. (3.9)}$$

The new martensite start temperature at stress T^b, M_s*, is:

$$M_s^* = \theta = M_s + \frac{T^b}{C_M} \quad \text{Eq. (3.10)}$$

Moving from point b to point c is where things become more complicated. Due to the change in martensite fraction, the stress-strain curve is no longer linear and must be iteratively calculated to properly simulate the relationship. As was seen in the Voigt expression, the Young's modulus changes with martensite fraction. The martensite fraction is calculated as a function of the stress and is defined as:

$$\xi^{b\to c} = \frac{1}{2}\{\cos\left[a_M(\theta - M_f) - \frac{a_M}{C_M}T^{b\to c}\right] + 1\} \quad \text{Eq. (3.11)}$$

Here a_M is defined as:

$$a_M = \frac{\pi}{M_s - M_f} \quad \text{Eq. (3.12)}$$

The stress and strain in this region are defined as:

$$T^{b\to c} = Y^{b\to c}S^{b\to c} - S_L Y^{b\to c}\xi^{b\to c} \quad \text{Eq. (3.13)}$$

$$S^{b\to c} = \frac{1}{Y^{b\to c}}T^{b\to c} + S_L\xi^{b\to c} \quad \text{Eq. (3.14)}$$

The stress is limited to the stress at the beginning of martensitic transformation, T^b, and the stress at the end of martensitic transformation, T^c. These stress values are then used to calculate the strains at the same points, S^b and S^c. Due to the complexity of the dependencies within the equations, for the simulation the stress $T^{b->c}$ was incrementally increased from T^b to T^c while calculating $S^{b->c}$, $Y^{b->c}$, and $\xi^{b->c}$ for each iteration. This was done due to the cosine function within $\xi^{b->c}$ which created a divergent graph when the $S^{b->c}$ was incrementally increased instead of $T^{b->c}$. Once the SMA has fully transformed to the martensitic phase, at point c, the stress and strain is calculated as:

$$T^c = C_M(\theta - M_f) \quad \text{Eq. (3.15)}$$

$$S^c = \frac{C_M(\theta - M_f)}{Y_M} + S_L \quad \text{Eq. (3.16)}$$

The new martensite finish temperature at stress T^c, M_f* is:

$$M_f^* = \theta = M_f + \frac{T^c}{C_M} \quad \text{Eq. (3.17)}$$

From point's c to d, the SMA is unloaded back to zero stress, and the stress-strain relationship is simply a linear relationship defined as:

$$T^{c\to d} = Y_M(S^{c\to d} - S_L) \quad \text{Eq. (3.18)}$$

At point d, the stress $T^d = 0$ and the strain $S^d = S_L$. The final step from point d to e is when the temperature, θ, is raised to above A_f at zero stress and then cooled back to the original θ which brings the graph back to point a. This shown in the stress-strain graph as a line across the x-axis from S_L to S=0.

The actual constants needed for these calculations, such as C_M, S_L, Y_M, and Y_A, were not provided for the Nitinol wire that was purchased from Amazon.com so a simulation of the stress-strain curve for this material is not possible unless extensive testing is conducted to define

each material property. The data sheet for Flexinol provides useful properties such as density, specific heat, melting point, etc., however it does not specify transformation temperatures, Young's moduli, or coefficients of stress influence. These properties were found in the literature, and are listed below (Choon et al., 2007):

- Young's Moduli: $Y_M = 33$ GPa, $Y_A = 70$ GPa
- Coefficients of Stress Influence: $C_M = 9.1$ MPa/°C, $C_A = 10.8$ MPa/°C
- Transformation Temperatures: $A_s = 52.54$°C, $A_f = 60.90$°C. $M_s = 44.78$°C, $M_f = 32.48$°C.

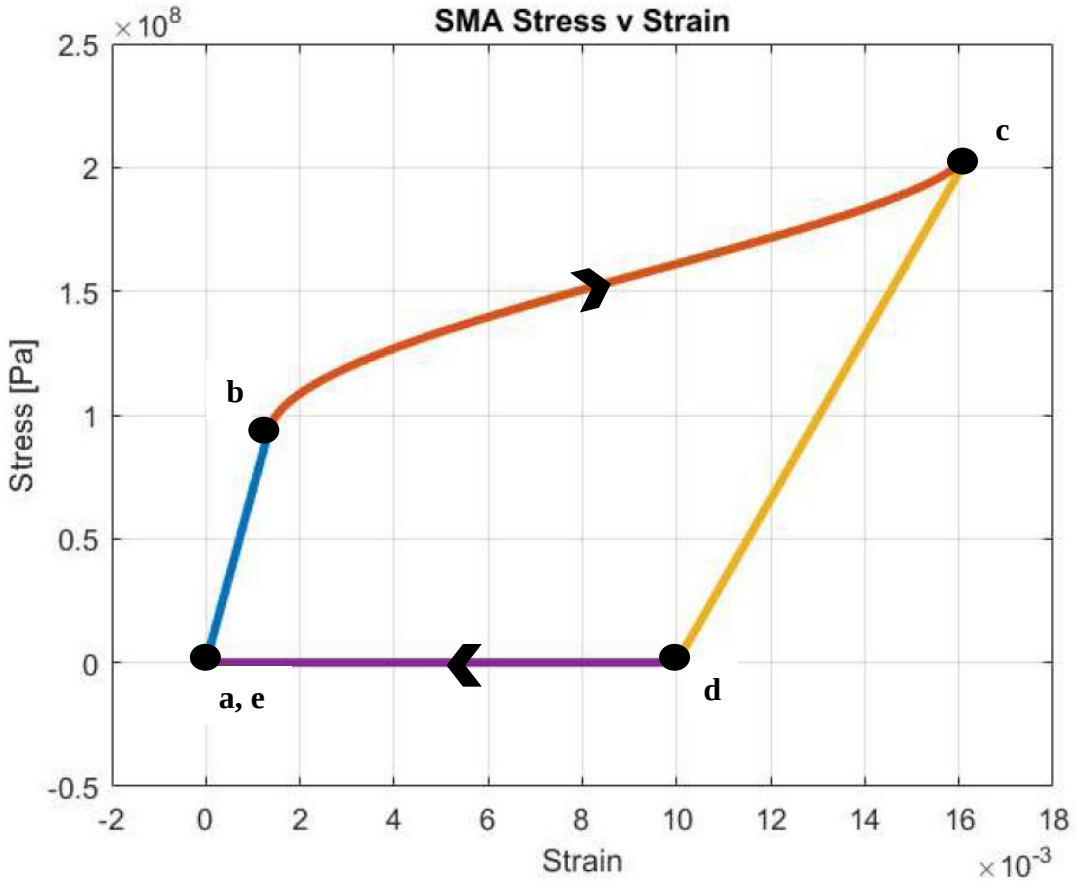

Figure 3.11: Simulated SMA Stress-Strain Curve.

The temperature for this simulation was arbitrarily chosen to be 55°C since it is between M_s and A_f. The graph of this simulation is shown below in Figure 3.11. A full MATLAB code for this simulation can be found in Appendix B. This graph is the expected response of a Flexinol

wire at 55°C. This simulation can be repeated for other SMA materials as long as the above constants are known for the specific material.

3.4.2 Pull-Force Test

The Nitinol that was ordered from Amazon.com was said to have several pounds of

Table 3.1: Flexinol Data (Dynalloy, Inc., 2020).

Diameter Size inches (mm)	Resistance ohms/inch (ohms/meter)	Pull Force* pounds (grams)	Cooling Deformation Force* pounds (grams)	Approximate** Current for 1 Second Contraction (mA)	Cooling Time 158°F, 70°C "LT" Wire *** (seconds)	Cooling Time 194°F, 90°C "HT" Wire *** (seconds)
0.001 (0.025)	36.2 (1425)	0.02 (8.9)	0.008 (3.6)	45	0.18	0.15
0.0015 (0.038)	22.6 (890)	0.04 (20)	0.016 (8)	55	0.24	0.20
0.002 (0.050)	12.7 (500)	0.08 (36)	0.032 (14)	85	0.4	0.3
0.003 (0.076)	5.9 (232)	0.18 (80)	0.07 (32)	150	0.8	0.7
0.004 (0.10)	3.2 (126)	0.31 (143)	0.12 (57)	200	1.1	0.9
0.005, (0.13)	1.9 (75)	0.49 (223)	0.20 (89)	320	1.6	1.4
0.006 (0.15)	1.4 (55)	0.71 (321)	0.28 (128)	410	2.0	1.7
0.008 (0.20)	0.74 (29)	1.26 (570)	0.50 (228)	660	3.2	2.7
0.010 (0.25)	0.47 (18.5)	1.96 (891)	0.78 (356)	1050	5.4	4.5
0.012 (0.31)	0.31 (12.2)	2.83 (1280)	1.13 (512)	1500	8.1	6.8
0.015 (0.38)	0.21 (8.3)	4.42 (2004)	1.77 (802)	2250	10.5	8.8
0.020 (0.51)	0.11 (4.3)	7.85 (3560)	3.14 (1424)	4000	16.8	14.0

lifting force, however this does not provide a concrete number. Dynalloy provides pull-force values for their Flexinol wires, and these can be seen in the chart in Table 3.1 (Dynalloy, Inc., 2020).The Flexinol wires only go up to a diameter of 0.51 mm, whereas the Nitinol from Amazon.com has a diameter of 1 mm. A representation of the Flexinol pull force data can be seen in Figure 3.12. Using the MATLAB curve fitting tool, the following fitted curve equation was generated:

$$Pull\ Force = 0.3718 * e^{6.056D} \quad \text{Eq. (3.19)}$$

Using Equation (3.19) provides a pull force of 158 lbs for a wire diameter of 1 mm. This is an unrealistic number for a 1 mm diameter Nitinol wire, and this means that the exponential fit is an

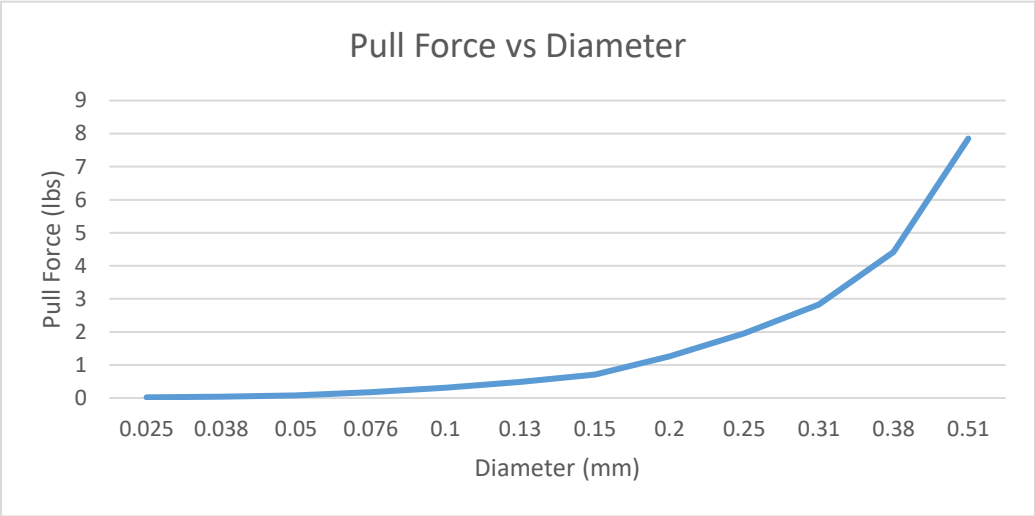

Figure 3.12: Flexinol Pull Force vs Diameter.

incorrect model and/or the Nitinol from Amazon.com has differing physical properties than the Flexinol due to differences in manufacturing.

To determine the pull force of the Nitinol from Amazon.com, a SMA spring-bias setup can be used. This configuration is used in some SMA applications to provide a bias force to the SMA after actuation in order to reset the pre-strain. Figure 3.13 shows a set-up of the experiment where the black wire is the SMA. The SMA wire will be electrically activated using a current dependent on its physical properties, whose relationship will be defined in Section 3.5, and the

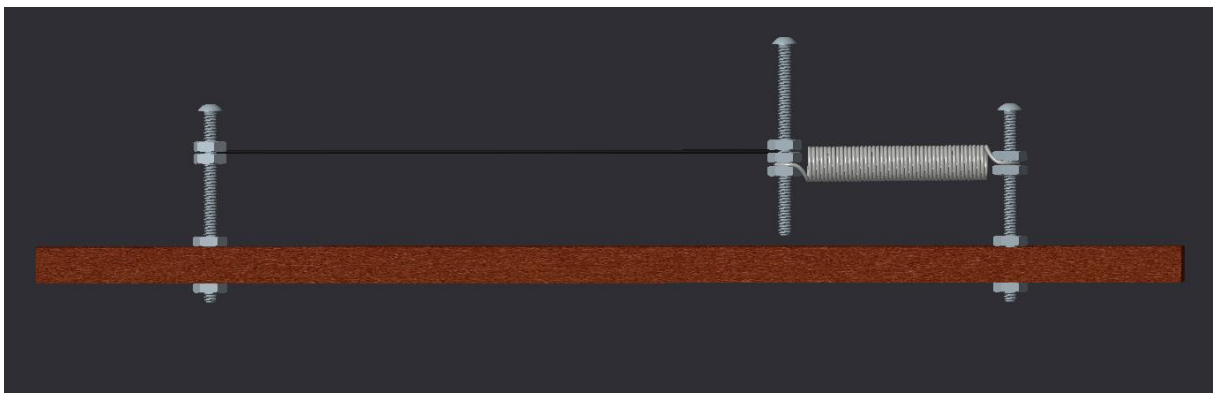

Figure 3.13: SMA Pull Force Test Setup.

resulting contraction will cause the spring, with a known spring constant, k, to extend a specific distance, x. Since the SMA and spring are in equilibrium, the SMA pull force can be calculated using Hooke's law, $F_s = -kx$, where $F_{SMA} = F_s$.

3.4.3 Angle Recovery Test

The Angle Recovery test was designed to test the actuation ability of the SMA wires. Looking at the Temperature vs Strain characteristics of Flexinol in Figure 3.14, it is apparent that the strain recovery rate is highest shortly after A_s and slows down towards the limit of strain recovery.

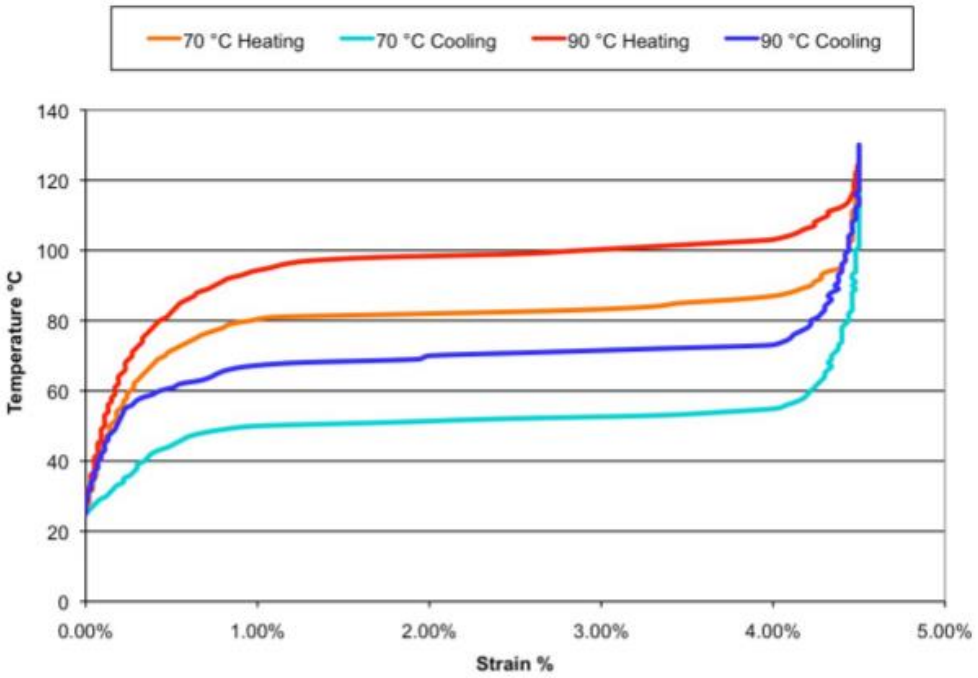

Figure 3.14: Flexinol Temperature vs Strain Characteristics (Dynalloy, Inc., 2020).

This sluggish response towards the end of the heating cycle means that the SMA may not fully sweep through the full 45° stroke. The 1% pre-strain that is included in the deployed configuration in order to sense compressive loads should combat this behavior since the end of deployment occurs before the end of strain recovery.

The Angle Recovery test is set up by fixing one end of the cubic truss along the Y-axis such that the hinge axis is coincident with the Z-axis at the origin, and bending the free end to the pre-defined 45° angle. The Z-axis is parallel to the gravitational force. The SMAs will then be heated and the angle recovery will be recorded. The pre-strain of the wire will be used as the independent variable by using different SMA mounts on the joint to incorporate varying lengths of SMA wires and to tune the r value. Multiple mounting configurations can be manufactured

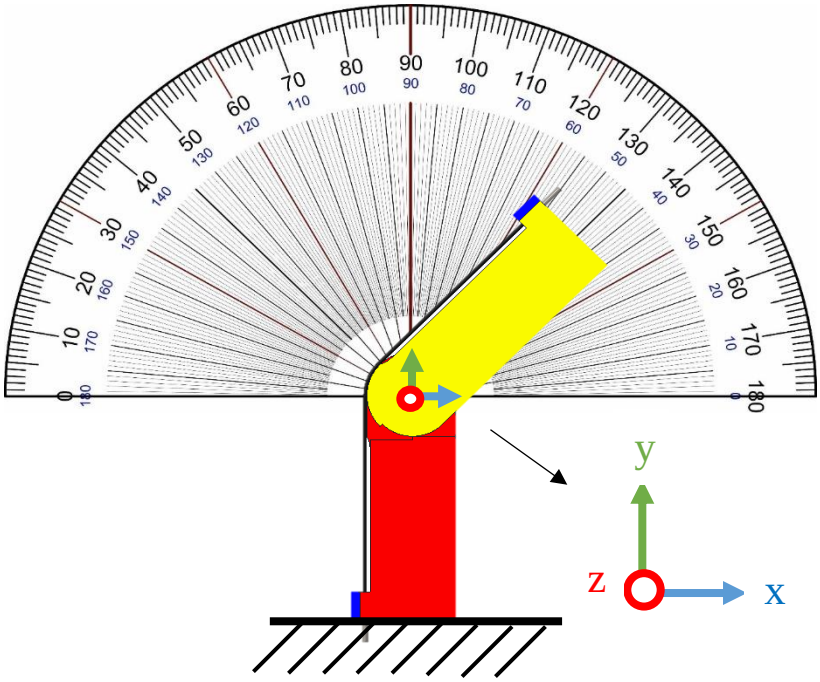

Figure 3.15: SMA Angle Recovery Test.

easily due to the accessibility of 3D printers at the ISA lab. Figure 3.15 shows a representation of how the test will be set up.

3.4.4 Torque Balance Test

An alternate variation of the Angle Recovery test includes the tape spring version of the cubic truss hinge joint. If the deployed pre-strain is not enough to sweep across 45°, then a secondary Torque Balance test will be set-up that tests the plastic moment of the SMA wires vs the torque of the tape spring. This test was inspired by the test whose results are shown in Figure

2.16. The set-up for this test will be similar to that shown above in Figure 3.15, however an I-bolt will be screwed into the free end of the joint which will be attached to a force gauge that is held tangent to the circle of deployment. This set-up can be seen in Figure 3.16.

The first recording from the force gauge will only be of the tape spring with no SMA wires attached. This will provide the moment of the tape spring at a 45° angle. The SMA wires

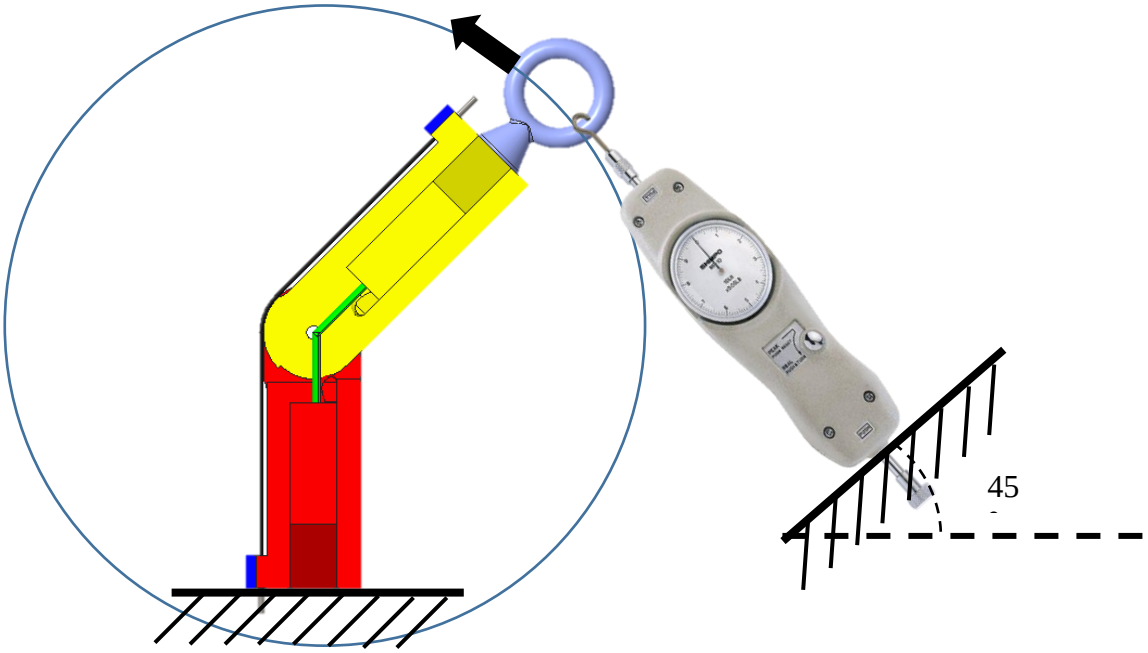

Figure 3.16: Torque Balance Test using Force Gauge.

will be added one at a time and placed back into the 45° configuration to record the new force which will provide the necessary data for the plastic moment added from each SMA wire. Once the force gauge reads 0, the plastic moment of the SMA wires will have overcome the deployment torque of the tape spring. Judging from the graph shown in Figure 2.16, the tape spring's moment should not overcome the plastic moment of the SMAs until the end of deployment, which solves the end of deployment problem due to the SMA's slowing strain recovery rate.

3.4.5 Sensing Test

The SMA cubic truss hinge joint will undergo incremental loading in order to validate the sensing function of the SMA wires. A hanging mount will be used for the cubic truss joint and weights will be attached via an I-bolt. A representation of this set-up can be seen in Figure 3.17 where P_{HW} represents the load from the hanging weights.

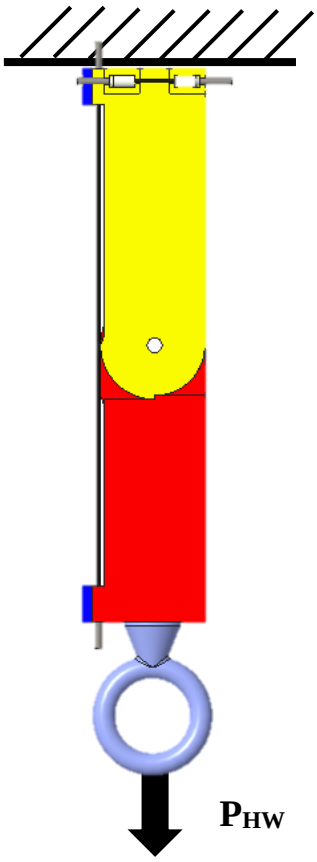

Figure 3.17: SMA Cubic Truss Joint for Sensing Test with Hanging Weight Load.

A pre-validated strain gauge will be attached to the cubic truss joint as a confident source of strain measurement, while the variation in ER from the SMA wires will be used to calculate the strains using the relationship introduced in Equation (2.5). A 200 mm length SMA wire with a maximum strain of 6% provides a maximum $\Delta L = 12$ mm. Using a diameter of 1 mm, the resistivity and Poisson's Ratio provided by the Flexinol data sheet, and the relationship from Equation (2.5), the following graph in Figure 3.18 was created.

In the sensing test, an elongation of 12 mm is unrealistic, however this relationship shows that at a low elongation of ~1 mm, or ~0.5% strain, the ER should vary by ~1%. Since Equation

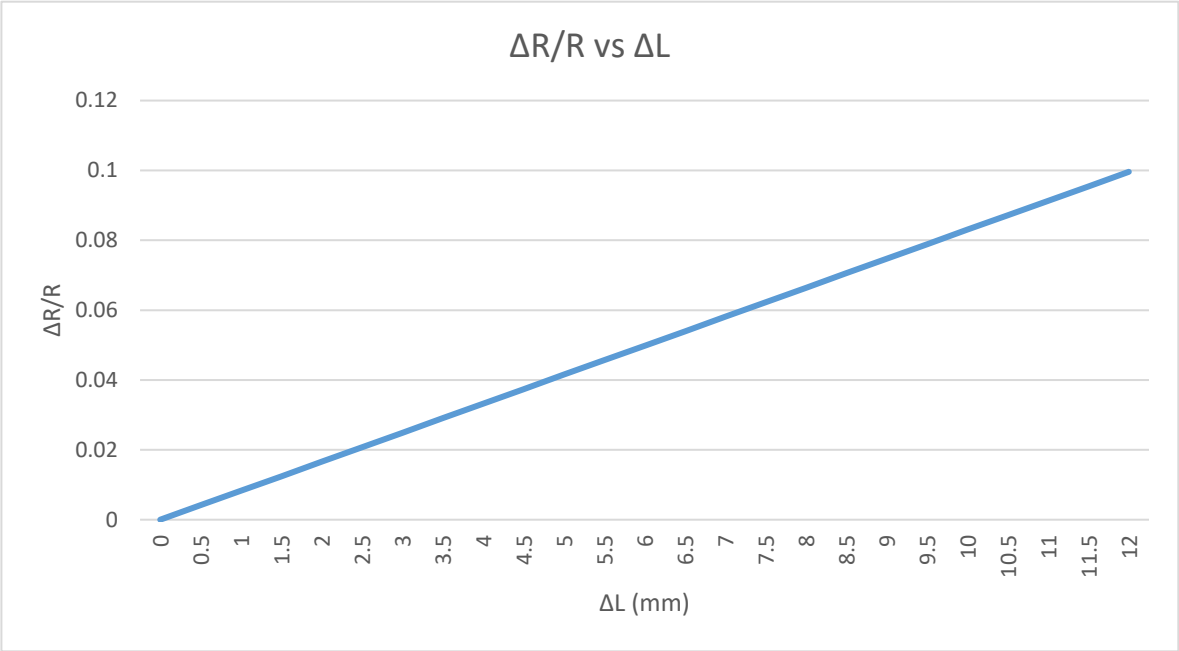

Figure 3.18: Variation of ER vs ΔL.

(2.5) does not take the piezo-resistive effect into consideration, this relationship is only an approximation. In reality, the ER change will not be perfectly linear and the piezo-resistive effect will be examined in the sensing test results. This test is meant to be conducted on 3D printed materials such as PLA plastics which have a moduli of ~3.5 GPa, which is much smaller than the ~350 GPa modulus of carbon composites (*Comparison of typical 3D printing materials*, 2005). For this reason lighter weights will be used for the 3D printed test than future tests using carbon composite models. It is difficult to predict the required loads to produce the desired strains because of the interaction between the 3D printed plastic, the SMA wires, and all the connection points between the hinges, I-bolt, SMA wires, etc. If a homogenous PLA plastic part is considered, the ultimate tensile strength (UTS) of PLA is provided as 36 MPa. Using an approximate cross-sectional area of the cubic truss joint of 750 mm^2, a load of 27 kN or ~6000 lbs is required to reach the UTS. This load is unrealistic due to the differences between a

homogenous plastic part and a 3D printed mechanism. The 3D printer settings, including orientation of the layers as well as the infill percentage, can majorly affect the strength of printed parts, as well as the tolerances of the connection points.

Using the hanging weights at the ISA lab, the cubic truss joint will be loaded at 10 lb intervals and the strain will be compared between the SMA wires and the strain gauge. A physical marking will be made at the unloaded and loaded configurations to quantify any strains at the connection points that will not be recorded by the strain gauge which is solely reading strains in the PLA material.

3.5 Electronics

In this section the author will discuss the electrical requirements for actuating the SMA hinge joint. The exact properties of the sourced SMA are unknown so values from an alternative manufacturer will be used for approximations. The control of the electrical power through ER measurements to determine phase transformation will be shown. The differences in electrical requirements due to the specific circuitry will be calculated. The requirements for the circuits for both heating and sensing will be outlined.

3.5.1 Joule Heating

Joule heating will be used to raise the temperature of the SMA wire in order to activate the austenitic phase transformation and thus actuate the wire. The current necessary to reach A_f can be calculated using Equation (2.16). Considering the Nitinol from Amazon.com, the diameter of the SMA is 1mm and the resistivity is not given. The Flexinol data sheet gives an approximate resistivity, ρ, value for Nitinol of 80 micro-Ohms*cm for martensite and 100 micro-Ohms*cm for austenite (Dynalloy, Inc., 2020). The heat transfer coefficient is calculated using the thermal wizard mentioned in Section 2.3.1. Considering the fluid to be air at 20°C, and given

wire diameter of 1 mm, wire length of 200 mm, and average wire temperature of 50°C, the heat transfer coefficient is h = 25.06 W/m^2-°C. Plugging these values into Equation (2.16) provides a current of 2.15 A. A time estimate for heating to 80°C using 2.15 A can be calculated using Equation (2.17). The density, specific heat, and latent heat of Nitinol can all be found on the data sheet for Flexinol from Dynalloy and are 6.45 g/cm^3 , 0.2 cal/g*°C, and 5.78 cal/g respectively (Dynalloy, Inc., 2020). Converting these to SI units provides: 6450 kg/m^3 , 837 J/kg*K, and 24.7 J/kg. Plugging all these values into Equation (2.17) provides a time of 115 seconds. It is important to note that the authors that developed this estimate made many assumptions and explicitly said it is an order of magnitude estimates.

Leaving a 2.15 A current on for 115 seconds may have unintended consequences for the integrity of the SMA, especially with the unreliability of the time calculation. The Flexinol data sheet provides a chart, shown in Table 3.1, which contains a list of currents necessary to contract SMAs of multiple diameters in one second each (Dynalloy, Inc., 2020). Plotting the data from this chart provides the graph in Figure 3.19.

It can be observed that the trend is exponential and at half a millimeter diameter the current is already at 4 A. It is not necessary to contract the SMA very quickly in one second for the deployment of the modular trusses, so the heating process can be conducted over a longer period of time and therefore require less current. Most ISA procedures move very slowly to minimize any chance of collision or unwanted inertial loads transferred into the structure, which means that longer heating processes can be just as, if not more, viable for this application.

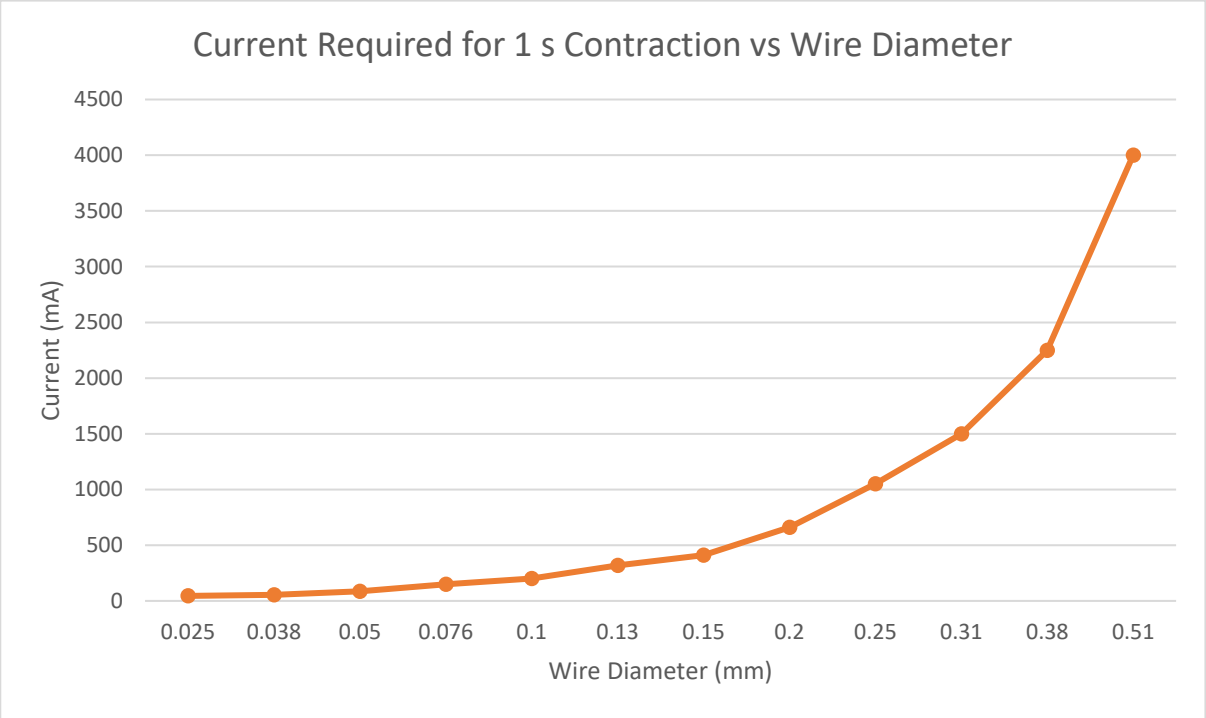

Figure 3.19: Current required for 1 s contraction vs SMA wire diameter.

3.5.2 Current Source (DC vs PWM)

Direct Current (DC) sources have been proven to be dangerous to SMA materials due to how easily DC can overheat the material. Capacitors can be used to provide an impulse current of large magnitude that can rapidly finish the phase transformation of the SMA. Equation (2.18) was used to determine the energy required for full phase transformation and from the study these equations originated from, the energy required was more easily provided by a set of capacitors than a traditional power source. The energy required for transformation is the driving variable to

determine the necessary current for transformation. The material constants for Equation (2.18) can be derived from the information on the Flexinol data sheet. Converting the constants to SI units provides a density of 6450 kg/m^3 , specific heat of 837 J/kg*K, and latent heat of transformation of 24180 J/kg. The change in temperature, ΔT, is from ambient, 20°C, to A_f , which was found to be 60.9°C, which gives 40.9°C. Using a 1 mm diameter and a length of 200 mm makes a volume of $1.57*10^{-7}$ m^3, and this calculates to a SMA mass of 0.00101 kg. Plugging these values into Eq. (2.18) gives an energy of transformation of 59 J. The rate at which this energy is provided gives the power, and for the study these equations were pulled from the authors used an objective response rate of 10 ms, which would require a power of 5.9 kW in this application. This fast of a response time is not necessary for the SMA cubic truss joint, so a response time of a second or even 10 seconds can be used. It can be argued that having a response time of 10 ms can be harmful for the SMA mechanism, since that speed will add impulsive loads to the structure. The direct Ohmic heating equation for power is:

$$P = RI^2 \qquad \text{Eq. (3.20)}$$

Considering a 10 s response time requires a power of 5.9 W, and with an ER of 0.204 Ohms, the required current would be ~5 A. Considering a 60 s response time requires a power of 0.983 W which requires a current of ~2 A. In the source study, a power of 26.2 kW was desired and this required a current greater than 3204 A. Each capacitor that was used could store 200 J of energy and 3 capacitors were necessary to satisfy the study's requirements. The power required for the SMA cubic truss joint does not necessitate a capacitor, however providing the necessary current for a long period of time may be dangerous to the SMA without proper control.

Referencing the methods introduced in Section 2.3.1, the electrical current source for this application follows a step-wise model. Using Figure 2.22 as reference, the SMA will begin in

100% martensite at the top left of the graph. As the high current is applied, the temperature will increase thus causing the phase transformation which signifies moving down the right side of the graph. Once the ER reaches that of the austenitic phase, it will be known that the temperature has crossed A_f. Including a safety margin in this design causes a step-wise graph, where when the ER crosses below a threshold, the current is dropped to a safe value that can be maintained without overheating the SMA. For applications that require multiple actuations, this creates a current response similar to a PWM signal. The SMA cubic truss joint will not be heated multiple times, so it can be possible to simply monitor the ER of the SMA to determine the temperature during deployment. From the results of the energy of transformation equation, 5 A over 10 seconds, or 2 A over 60 seconds should complete the phase transformation. The 2 A current for 60 seconds relates well to the current requirement solved for in Section 3.5.1, where the order of magnitude time estimate is close to 60 seconds. The response of the actuator can be tested by applying 2 A to the fully martensitic SMA, and monitoring the ER until it reaches that of the austenitic phase, which nominally should take 60 seconds.

A separate approach is to use a PWM signal to reduce the chance of overheating. Using a PWM power source can more reliably heat an SMA, especially for applications where time is not a major limiting factor. Using the method proposed by Furst & Seelecke, (2012) may be beneficial for controlling the power inputted into the SMA. Using a ~1 kHz frequency with a varying duty cycle dependent on the measured ER, the average current is tuned to provide constant power. This approach uses the same principle of ER measurement to tell SMA phase as the previous approach. In lab testing, a PWM current signal can be created using a signal generator, power source, and comparator. Lab testing can determine the proper duty cycle for a 2 A amplitude current source such that the SMA does not overheat, but does complete phase

transformation. Having a pre-defined duty cycle will simplify the heating procedure. For a structure that relies on a large number of similar modules, the reduction of complexity for one module has a multiplicative benefit over the entire system. The simplest solution that requires the least resources would be to provide a DC over a period of time and use the already built in sensing function to monitor the ER in order to tell when the phase transformation has completed, however since the equations only provide information for ideal situations, a PWM signal with a pre-defined duty cycle can more efficiently and safely heat the SMA.

Lab testing will be conducted on the SMA by applying a 2 A amplitude PWM current while monitoring the ER until it reaches the austenitic ER, which for a 1 mm diameter SMA with a length of 200 mm is 0.255 Ohms. The phase transformation should also be visually apparent when the SMA cubic truss joint has swung through its 45° stroke. If it is observed that the SMA is overheating too quickly, the duty cycle of the PWM signal will be decreased.

3.5.3 Circuit Designs

3.5.3.1 Heating

A signal generator, power source, and comparator can be used in order to create the PWM current signal. For 2 A at 60 s, the required power is 0.983 W, and the voltage will be 0.45 V. Using a comparator to compare the signal generator ramp function voltage with the analog input of 0.45 V, when the analog input is higher than the ramp function, the current will be at a high 2 A, and when the input is lower than the ramp function, the current will go to 0 A. Normally the input voltage would be controlled by a potentiometer, which controls the duty cycle, however for this application the shape and amplitude of the ramp function will have to be changed in order to specify the duty cycle.

A more portable method of creating a PWM signal would be using an Arduino. An example of an Arduino based PWM circuit for a DC motor can be seen in Figure 3.20 (J., n.d.).

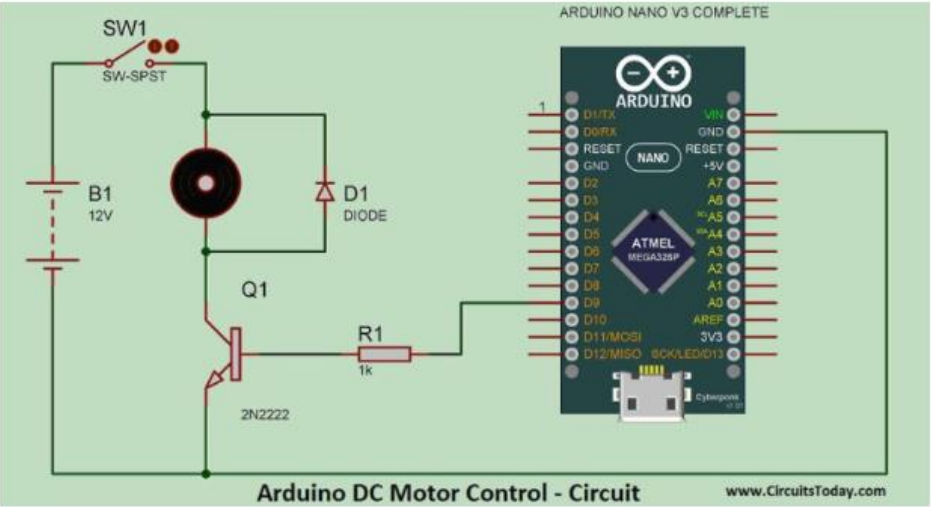

Figure 3.20: Circuit Diagram of Arduino Based PWM Signal Generator (J.,n.d.).

This design requires the Arduino, a transistor, resistor, diode, power adapter, and DC motor. Replacing the power adapter with the power source in the lab and the DC motor with the SMA, the Arduino can be programmed to provide a PWM current signal to the SMA. The duty cycle of the signal is expressed as a ratio of the time on over the time period. By increasing or decreasing the duration of time on, the duty cycle will increase or decrease respectively. Due to the high currents necessary as input into the SMA, the transistor and diode will have to have high current capacities or the amplitude of the current will have to decrease, therefore increasing the heating time.

In terms of wiring of the multiple SMA wires, the decision is between mounting in parallel or in series. Figure 3.21 shows examples of 5 SMA wires mounted in each configuration.

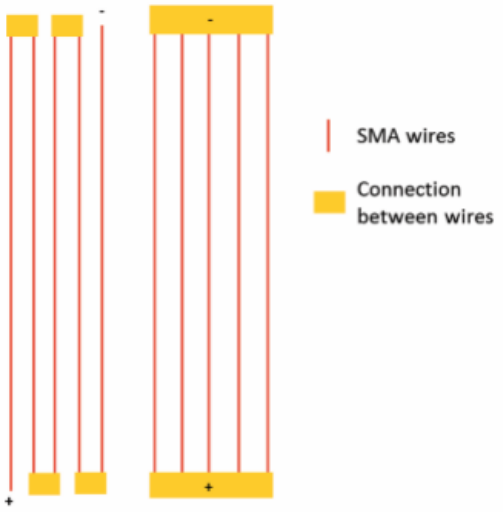

Figure 3.21: Multiple SMA wires mounted in (Left) Series (Right) Parallel (Britz et al., 2018).

Wiring in series requires the input voltage be increased due to the voltage drop after each wire, however this requires a lower current. For example, Britz et al., (2018) used an SMA wire with a 0.25 mm diameter and a length of 100 mm which had an ER of 1.85 Ohms and required 1050 mA and a voltage of 1.94 V to heat in 1 s. For the SMA wires in series, this voltage sums to a total of 9.7 V. In parallel, the voltage would be set at 1.94 V, however the current required is a sum of each wire, which for 5 wires means a total current of 5.25 A. For the SMA cubic truss joint, a maximum of 4 wires can be used. If the maximum number of wires are used; in series this would increase the voltage to 1.8 V while keeping the current at the fixed 2 A, and in parallel the current would jump to 8 A while the voltage stayed at 0.45 V. Wiring the SMAs in parallel provides more even heating and makes the mechanism mechanically redundant if one wire is damaged at some point in the modules lifetime. The number of wires needed will be dependent on the results of the aforementioned tests, however the current requirements of

multiple wires in parallel may necessitate a reduction in the amplitude of the current source. This would increase the heating time, but again, that is not a major limiting factor for this application.

The specific circuit components, as well as the current amplitude and heating time will be dependent on the power source and circuit components available in the lab, as well as the response of the SMA after preliminary heating tests. If the SMA is overheating, the duty cycle of the PWM signal will be decreased and the current amplitude can also be adjusted.

3.5.3.2 Sensing

The sensing function of the SMA is simply to read the change in ER of the material. Due to the simplicity of the function, the circuit will only involve providing a small current to the SMA and monitoring the change in voltage as the ER of the SMA varies with strain. A baseline ER will be defined which takes into account the 1% pre-strain included for monitoring of compressive loads. For lab testing, the SMA will be attached to a multimeter which has the ability to read the ER without any additional features. In-situ, an on-board computer located centrally on the PA will monitor the ER across the SMAs. No additional features will be required on the individual module once the truss has been electrically and mechanically connected to the PA.

Chapter 4: Conclusion

4.1 Review

SMAs are a unique class of material that can be utilized in a variety of applications. Their multi-use functionalities were portrayed in this paper for the use of deployment and sensing using a single SMA mechanism. The benefits SMAs provide to a system are aligned with the PA paradigm. Their ability to actuate a module using two to three orders of magnitude less mass than a traditional actuator has a multiplicative reduction in parasitic mass across the entire PA.

Using the relationship between ER and martensite fraction also provides position control to the actuation and further automates the structure. Not only do SMAs provide self-sensing actuation and a higher force-to-weight ratio than traditional actuators, SMAs can also switch functions to a strain sensor without the integration of additional sensing elements.

Current space missions are restricted in size by the dimensions of the payload fairing that will launch the system. The PA paradigm aims to overcome these restrictions by utilizing ISA of unit truss modules to build large scale space assemblies. The truss modules are designed to be packaged down so that the maximum number of modules can fit within a payload fairing. Over multiple frequent and inexpensive launches, these modules will be sent into space to be deployed and assembled into any configuration necessary for the specific mission. SMAs allow the modules to deploy without external assistance, thus increasing the efficiency of the robotic agents that can solely focus on assembling the PAs.

As space structures move towards all carbon composite designs, SMAs can be integrated both as external and internal features, not only to serve as a deployment actuator and a strain sensor, but also as a means of self-rehabilitation of damaged structural components. The flexibility of integration for SMAs in different environments allows them to be viable in many disciplinary fields, however the commercial availability of these unique materials are fixed to a specific subset, mainly Nitinol and its alloys. With further experimentation and advancement of manufacturing procedures, SMAs with different compositions have the potential to be applied to a variety of environments and engineering applications.

In this paper, the author designed a novel mechanism, capable of functioning as both an actuator and sensor, to be used in the creation of an autonomous truss module that will be deployed and assembled into a PA. In accordance with the PA paradigm, SMAs supplement the

modularity of the current truss structures by providing high force-to-weight actuation, thus creating an autonomous structure that minimizes the parasitic mass that normally comes with conventional autonomous deployment mechanisms. The complementary sensing function further reduces parasitic mass and increases autonomy of the structure by providing a continuing function for the SMA integrated truss joint and providing valuable strain gauge information.

4.2 Future Work

Moving forwards, all of the aforementioned tests will be conducted to characterize the sourced SMA materials and observe their response in terms of actuator and sensor capabilities. The first step after testing on 3D printed materials is to produce a more reliable model of the truss joints using metal or composite materials. Scaling up the truss models to their appropriate in-situ size will provide more surface area for mounting on the joints as well as customization of the pre-strains in the SMA wires. Once the SMA mechanism has been validated for the cubic truss joint, an analogous mechanism will be applied to the tri-truss model. One of the future goals is to create a tri-truss that is fully integrated with SMA wires for actuation and sensing functionalities. More information on the future work, including the acquisition of testing materials, can be found in Appendix C.

Incorporating pseudoelastic SMAs is an option for further study. This effect can provide strain energy for actuation and higher sensitivity sensing, however there are special considerations for using the pseudoelastic effect. The SMA must be above the austenitic finish temperature in order to exhibit this effect, and for externally mounted wires this can be difficult, especially in the space environment. Specific SMAs will have to be identified that will remain austenitic at room temperature for lab testing, and that will remain austenitic at the ambient temperature in LEO for a space module. Since there is no heating process necessary for

recovering strain with pseudoelastic SMAs, the design will require launch locks to hold the strain energy. Some sources that investigated pseudoelasticity for self-sensing include the works by Li et al., (2005), Senf et al., (2017), and Mäder et al., (2017).

It will be helpful to simulate SMAs in a FEM software. The simulations will be useful in predicting the response under specific loads. Simulating the complex thermo-mechanical relationship of SMAs requires a model that takes into account the apparent inelastic strain recovery through the martensitic to austenitic phase transformation. This will allow for simulations of more robust and scaled up truss designs.

One of the potential substitutions for strengthening the joints is a carbon composite coilable boom which provides strain energy when folded. Since this composite boom acts as both the structural member and the bending feature, SMAs can be mounted within the hollow interior where their plastic moment will overcome the strain energy of the composite until the SMA is heated and then deploys similar to the SMATSH. Once in the deployed configuration, since the SMA is mounted on the interior of the structural member, it will be within the load path and therefore sense any tensile or compressive stresses acting on the composite. Further analysis of this structure will prove useful in converting the truss modules to fully comprise of carbon composite materials, as well as creating a more robust SMATSH system.

The ultimate vision for this project is to create a space-rated autonomous truss modules that can be tested in-situ. The use of stronger materials and predictive simulation tools will help the development of the hinge joints and integration of the SMAs. Specific SMAs with transformation temperatures suited to the space environment will be identified and tested, and a mounting system that includes shielding for the SMAs will be designed. The final envisioned

space-rated autonomous truss modules will be the building blocks for large scale assemblies that will further improve on in-space operations.

REFERENCES

Amazon.com. (2020). *Nitinol Shape Memory Alloy (SMA) pre-Trained Magic Muscle Wire (1.0mm (0.04"), 80°C (176°F), 10).* Retrieved 2020, from https://www.amazon.com/gp/product/B07N4JJPYB/ref=ox_sc_act_title_2?smid=ATAKSNAY2PYHR&psc=1

Angioni, S. L., Meo, M., & Foreman, A. (2010). Impact damage resistance and damage suppression properties of shape memory alloys in hybrid composites—a review. *Smart Materials and Structures*, *20*(1), 013001.

Auricchio, F., & Sacco, E. (1997). A one-dimensional model for superelastic shape-memory alloys with different elastic properties between austenite and martensite. *International Journal of Non-Linear Mechanics*, *32*(6), 1101-1114.

Auricchio, F., Fugazza, D., & DesRoches, R. (2007). A 1D rate-dependent viscous constitutive model for superelastic shape-memory alloys: formulation and comparison with experimental data. *Smart Materials and Structures*, *16*(1), S39.

Bao, M. (2005). *Analysis and design principles of MEMS devices*. Elsevier.

Benafan, O., & Gaydosh, D. J. (2019). Scale-up of NiTiHf shape memory alloy tubes with high torque capability. *Smart Materials and Structures*, *28*(8), 085035.

Bettini, P. A. O. L. O., Riva, M. A. R. C. O., Sala, G. I. U. S. E. P. P. E., Di Landro, L., Airoldi, A. L. E. S. S. A. N. D. R. O., & Cucco, J. (2009). Carbon fiber reinforced smart laminates with embedded SMA Actuators—Part I: embedding techniques and interface analysis. *Journal of materials engineering and performance*, *18*(5-6), 664-671.

Bhaskar, J., Sharma, A. K., Bhattacharya, B., & Adhikari, S. (2020). A review on shape memory alloy reinforced polymer composite materials and structures. *Smart Materials and Structures*.

Britz, R., Welsch, F., Kirsch, S. M., Simone, F., Schmidt, M., Motzki, P., & Seelecke, S. (2018, June). SMA Wires Bundles-Mechanical and Electrical Concepts. In *ACTUATOR 2018; 16th International Conference on New Actuators* (pp. 1-4). VDE.

Choon, T. W., Jamian, S., & Ghazali, M. I. Thermo-Mechanical Properties of Shape Memory Alloy.

Choon, T. W., Salleh, A. S., Jamian, S., & Ghazali, M. I. (2007). Phase transformation temperatures for shape memory alloy wire. *World Academy of Science, Engineering and Technology*, *25*(304).

Comparison of typical 3D printing materials. (2015). Retrieved 2020, from http://2015.igem.org/wiki/images/2/24/CamJIC-Specs-Strength.pdf#:~:text=Young%E2%80%99s%20Modulus%20%28GPa%29%201%3A%20Maker

bot%2C%20PLA%20100%2020,32.1%204%3A%20Ultimaker2%2C%20PLA%20150%2020%203%2027.2

Comparison: Webb vs Hubble Telescope - Webb/NASA. (n.d.). Retrieved 2020, from https://jwst.nasa.gov/content/about/comparisonWebbVsHubble.html

Cui, Di, Gangbing Song, and Hongnan Li. "*Modeling of the electrical resistance of shape memory alloy wires.*" Smart Materials and Structures 19, no. 5 (2010): 055019.

Doggett, W. R., Dorsey, J., Teter, J., Paddock, D., Jones, T., Komendera, E. E., & Mikulas, M. (2018). Persistent Assets in Zero-G and on Planetary Surfaces: Enabled by Modular Technology and Robotic Operations. In *2018 AIAA SPACE and Astronautics Forum and Exposition* (p. 5305).

Doggett, W., Dorsey, J., Jones, T., Mikulas, M., Teter, J., & Paddock, D. (2019). TriTruss: A New and Novel Structural Concept Enabling Modular Space Telescopes and Space Platforms.

Dynalloy, Inc. (2020). *Technical Charactersitics of Flexinol Actuator Wires*. Retrieved 2020, from https://www.jameco.com/Jameco/Products/ProdDS/357835.pdf

Featherstone, R., & Teh, Y. H. (2004, June). Improving the speed of shape memory alloy actuators by faster electrical heating. In *Proceedings of the Ninth International Symposium on Experimental Robotics*.

Fragnito, M., & Vetrella, S. (2002). A space release/deployment system actuated by shape memory wires. *Acta Astronautica*, *51*(11), 761-770.

Furst, S. J., & Seelecke, S. (2012). Modeling and experimental characterization of the stress, strain, and resistance of shape memory alloy actuator wires with controlled power input. *Journal of Intelligent Material Systems and Structures*, *23*(11), 1233-1247**.**

Hartl, D. J., & Lagoudas, D. C. (2007). Aerospace applications of shape memory alloys. *Proceedings of the Institution of Mechanical Engineers, Part G: Journal of Aerospace Engineering*, *221*(4), 535-552.

Huang, W. M., Ding, Z., Wang, C. C., Wei, J., Zhao, Y., & Purnawali, H. (2010). Shape memory materials. *Materials today*, *13*(7-8), 54-61.

Huang, W., Pellegrino, S., & Bashford, D. P. (1996, June). Shape memory alloy actuators for deployable structures. In *Spacecraft Structures, Materials and Mechanical Engineering* (Vol. 386, p. 53).

Ikuta, Koji, Masahiro Tsukamoto, and Shigeo Hirose. "*Mathematical model and experimental verification of shape memory alloy for designing micro actuator*." In [1991] Proceedings. IEEE Micro Electro Mechanical Systems, pp. 103-108. IEEE, 1991.

J. (n.d.). *DC Motor Speed Control Using Arduino & PWM with program and circuit*. Retrieved 2020, from https://www.circuitstoday.com/dc-motor-speed-control-arduino-pwm

Jani, J. M., Leary, M., Subic, A., & Gibson, M. A. (2014). A review of shape memory alloy research, applications and opportunities. *Materials & Design (1980-2015), 56*, 1078-1113.

Jeong, J. W., Yoo, Y. I., Shin, D. K., Lim, J. H., Kim, K. W., & Lee, J. J. (2014). A novel tape spring hinge mechanism for quasi-static deployment of a satellite deployable using shape memory alloy. *Review of Scientific Instruments*, *85*(2), 025001.

Koncar, V. (2018). *Smart Textiles for In Situ Monitoring of Composites*. Woodhead Publishing.
Li, Hui, Chen-Xi Mao, and Jin-Ping Ou. "*Strain self-sensing property and strain rate dependent constitutive model of austenitic shape memory alloy: experiment and theory*." Journal of materials in civil engineering 17, no. 6 (2005): 676-685.

M. Simulation (2014) Website: thermal wizard. https://thermal.mayahtt.com/tmwiz/convect/natural/horiz-cylinder/horiz-cylinder.htm

Ma, N., Song, G., & Lee, H. J. (2004). Position control of shape memory alloy actuators with internal electrical resistance feedback using neural networks. *Smart materials and structures*, *13*(4), 777.

Mäder, Thomas & Navarro, Iñaki & Senf, Björn & Wolf, Peter & Hamm, Martin & Zoch, Martin & Drossel, Welf-Guntram. (2017). Shape memory strain gauges. 10.5162/sensor2017/D4.1.

Mäder, Thomas, Inaki Navarro y de Sosa, Björn Senf, Peter Wolf, Martin Hamm, Martin Zoch, and Welf-Guntram Drossel. "*Highly Elastic Strain Gauges Based on Shape Memory Alloys for Monitoring of Fibre Reinforced Plastics.*" In Key Engineering Materials, vol. 742, pp. 778-785. Trans Tech Publications Ltd, 2017.

Nagai, H., & Oishi, R. (2006). Shape memory alloys as strain sensors in composites. *Smart materials and structures*, *15*(2), 493.

Nexmetal Co. (2020). *NITI • NITINOL SMA MUSCLE WIRE SHAPE MEMORY ALLOY*. Retrieved 2020, from https://nexmetal.com/collections/nitinol-wire/products/nitinol-memory-wire?variant=16787624708

Oishi, R., & Nagai, H. (2005). Strain sensors of shape memory alloys using acoustic emissions. *Sensors and Actuators A: Physical*, *122*(1), 39-44.

Pick, D. (n.d.). Shape Memory Alloys Achieve High Force and Precision. Retrieved 2020, from https://www.kiniticsautomation.com/technology/shape-memory-alloys-achieve-high-force-and-precision/

Qiu, J., Tani, J., Osanai, D., & Urushiyama, Y. (2001, March). High-speed actuation of shape memory alloy. In *Smart Structures and Devices* (Vol. 4235, pp. 188-197). International Society for Optics and Photonics.

Rao, A., Srinivasa, A. R., & Reddy, J. N. (2015). *Design of shape memory alloy (SMA) actuators* (Vol. 3). Berlin: Springer International Publishing.

Senf, Björn, Thomas Mäder, Iñaki Navarro y de Sosa, André Bucht, Marcus Knobloch, David Löpitz, and Welf-Guntram Drossel. "*Sensing and actuating functions by shape memory alloy wires integrated into fiber reinforced plastics*." In 1st CIRP conference on composite materials parts manufacturing, pp. 249-253. 2017.

Shahinpoor, M. (2005). *U.S. Patent No. 6,837,620*. Washington, DC: U.S. Patent and Trademark Office.

Song, G., Mo, Y. L., Otero, K., & Gu, H. (2006). Health monitoring and rehabilitation of a concrete structure using intelligent materials. *Smart materials and structures*, *15*(2), 309.

The Launch - Webb/NASA. (n.d.). Retrieved 2020, from https://jwst.nasa.gov/content/about/launch.html

Uchil, J. (2002). Shape memory alloys—characterization techniques. *Pramana*, *58*(5-6), 1131-1139.

Van Humbeeck, J. (1999). Non-medical applications of shape memory alloys. *Materials Science and Engineering: A*, *273*, 134-148.

Wei, Z. G., Sandstrom, R., & Mlyazaki, S. (1998). Review shape-memory materials and hybrid composites for smart systems. *Journal of Materials Science*, *33*(3), 743-3.

Xu, Y., Otsuka, K., Nagai, H., Yoshida, H., Asai, M., & Kishi, T. (2003). A SMA/CFRP hybrid composite with damage suppression effect at ambient temperature. *Scripta materialia*, *49*(6), 587-593.

Zarinejad, M., & Liu, Y. (2010). Dependence of transformation temperatures of shape memory alloys on the number and concentration of valence electrons. *Shape Memory Alloys: Manufacture, Properties and Applications*, 339.

APPENDICES

Appendix A: Matlab Code for Martensite Fraction vs Temperature

```
As = 53;
Af = 61;
Ms = 45;
Mf = 33;
aM = pi/(Ms-Mf);
aA = pi/(Af-As);

theta1 = [Ms:Af];
Mfrac1 = 0*theta1;
plot(theta1,Mfrac1,'LineWidth',3)
hold on

theta2 = [Mf:Ms];
Mfrac2 = 0.5*(cos(aM*(theta2-Mf))+1);
plot(theta2,Mfrac2,'LineWidth',3)

theta3 = [Mf:As];
Mfrac3 = 1+(0*theta3);
plot(theta3,Mfrac3,'LineWidth',3)

theta4 = [As:Af];
Mfrac4 = 0.5*(cos(aA*(theta4-As))+1);
plot(theta4,Mfrac4,'LineWidth',3)
hold off
title('SMA Martensite Fraction v Temperature')
xlabel('Temperature [\circ C]')
ylabel('Martensite Fraction')
xlim([30 65])
ylim([-0.25 1.25])
grid on
```

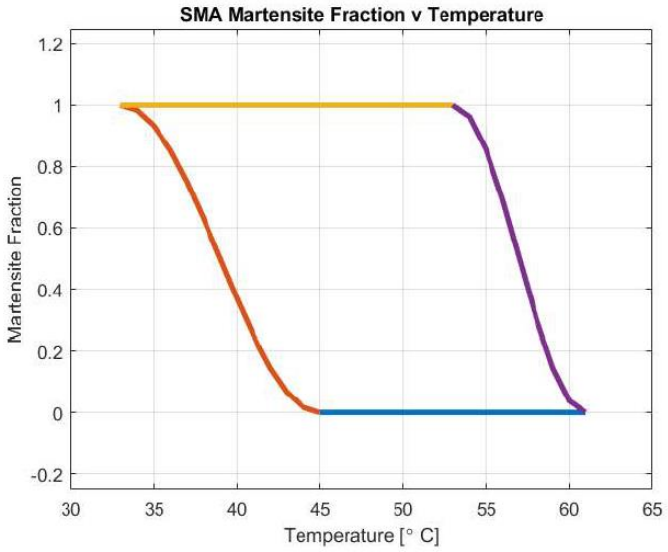

Published with MATLAB® R2016b

Appendix B: Matlab Code for SMA Stress vs Strain

```
Sl = 0.01;
YM = 33*10^9; %Pa
YA = 70*10^9; %Pa
am = pi()/12.3;%1/deg C
cm = 9.1*10^6; %MPa/deg C

Sab = 0:130; %*10^-5
Tab = YA*(Sab*10^-5); %Pa
plot((Sab*10^-5),Tab,'LineWidth',3)
hold on

Mfrac(1) = 0;
Y(1) = YA;
for i = 1:114
    Sbc(i) = Sl*(Mfrac(i)) + (((i+90)*10^6)/Y(i));
    Mfrac(i+1) = 0.5*(cos(am*(55-32.48)-(am/cm)*((i+90)*10^6))+1);
    Y(i+1) = Mfrac(i)*YM + (1-Mfrac(i))*YA;
end
Tbc = [91:204]; %*10^6
plot(Sbc,(Tbc*10^6),'LineWidth',3)

Scd = 1000:1620;%*10^-5
Tcd = YM*((Scd*10^-5)-Sl);
plot((Scd*10^-5),Tcd,'LineWidth',3)

Sde = 0:1000;%*10^-5
Tde = 0*Sde;
plot((Sde*10^-5),Tde,'LineWidth',3)
hold off
title('SMA Stress v Strain')
xlabel('Strain')
ylabel('Stress [Pa]')
xlim([-0.002 0.018])
grid on
```

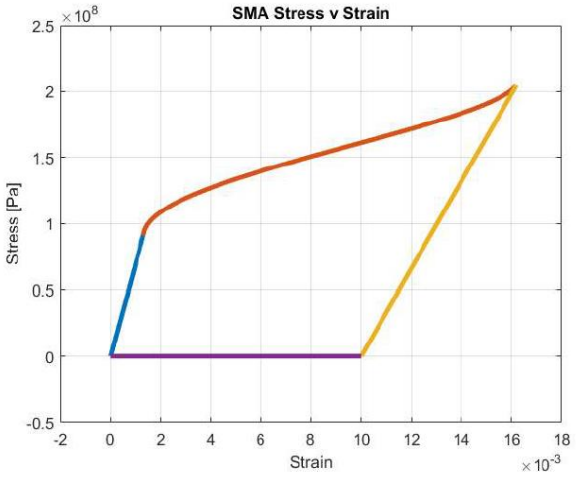

Published with MATLAB® R2016b

Appendix C: Plan Moving Forwards

AC.1 Materials

The SMA that was acquired before the COVID-19 quarantine started was “Nitinol Shape Memory Alloy (SMA) pre-Trained Magic Muscle Wire (1.0mm (0.04"), 80°C (176°F), 10)” from Amazon.com. This SMA did not provide a data sheet and the only known transformation temperature is A_S at 80°C. This SMA came as a bundle of 10 feet. The wire can be cut with a good pair of shears. The website for the previous Amazon purchase is: https://www.amazon.com/gp/product/B07N4JJPYB/ref=ox_sc_act_title_2?smid=ATAKSNAY2PYHR&psc=1

Many of the simulations done in this paper were using Flexinol data values. Flexinol is a Nitinol variant from Dynalloy, Inc. Flexinol is used in many academic studies and has much more information available both from the Dynalloy website and from the literature. It may be useful to acquire and test Flexinol so that the simulations can be matched to the test results. The Dynalloy provides crimping services to segment the Flexinol wires as well as provide electrical connections that can be soldered to. The Dynalloy website where Flexinol can be purchased is: https://www.dynalloy.com/index.php

Testing pseudoelastic SMAs is an option moving forwards as it provides strain energy and higher sensitivity strain sensing, however would require launch locks and an SMA that is fully austenitic at ambient temperature. For lab testing, a pseudoelastic SMA can be sourced from McMaster and Amazon, and may be available from Dynalloy, however the manufacturer would have to be contacted for custom SMA wires. The McMaster website for both Shape Memory Nitinol and Pseudoelastic (Superelastic) Nitinol: https://www.mcmaster.com/shape-

memory-wire/. There are other commercial manufacturers that can be used, most will provide Nitinol variants such as: https://www.fwmetals.com/products/actuator-wire/

There are differing wire diameters available from each source, it is good to note that as diameter increases the wire's ER decreases, so the required electrical current to heat to the specific temperature will increase. As of now the tests are designed for ~2A current over 60 seconds, however for shorter heating times, ~10s, a larger current, such as ~5A, may be necessary. A power source capable of providing these currents may be loaned from Dr. Travis Turner at NASA LaRC. In order to create the PWM current source, a signal generator can be used in the lab. A more portable method will be using an Arduino to define the time on over the time period in order to define the duty cycle of the PWM current source. An example of how to produce a PWM signal using an Arduino can be found here: https://www.circuitstoday.com/dc-motor-speed-control-arduino-pwm

The Teflon insulation, derived from polytetrafluoroethylene (PTFE), is available in both sheets and tubes from McMaster-Carr, however due to the small diameter of the sourced SMA, finding tubing for 0.5 mm to 1 mm wires can be difficult. A separate solution is using Teflon sheets at the interfaces between the wires and the 3D printed plastic. The Teflon can be attached to the 3D printed part using a 2-part epoxy or adhesive such as Permabond TA4610. Alternate insulating materials can also be used since the current maximum A_f does not exceed 100°C. Alternate options can be explored on McMaster-Carr here: https://www.mcmaster.com/about-plastic.

The PTFE/Teflon insulation options from McMaster-Carr can be found here: https://www.mcmaster.com/ptfe, and more information on Permabond TA4610 can be found here: https://www.permabond.com/wp-content/uploads/2016/04/TA4610_TDS.pdf.

Some of the tests will require mounts to be built, the structure of which can be created using 80/20 components. There are many 80/20 components in the ISA lab from previous builds that can be recycled and used to build the mounts for these tests, however due to current quarantine restrictions the exact components that are available are unknown. If there is need for additional 80/20 hardware to be bought, the necessary components can be searched and ordered from here: https://8020.net/.

AC.2 Testing

These tests are planned to be conducted at the ISA lab at NASA LaRC, however due to the current COVID-19 pandemic the tests may need to be relocated to the National Institute of Aerospace (NIA) or elsewhere if a suitable location is available.

One of the important set-up requirements is to impart a 1% pre-strain on the SMA during the initial mounting onto the joint. If the original length of the SMA is 200 mm, the SMA will have to be stretched 2 mm before mounting. This can be manually achieved in the martensitic phase by mounting one end of the SMA on one side of the joint, and then stretching the SMA by hand into the second mounting position that is 202 mm away from the first. Once mounted, the SMA can be heated to the austenitic phase to induce a recovery stress which will remain once the SMA has cooled back to the martensitic phase.

AC.2.1 Material Property Tests

The specific SMA that is used, whether it comes with a data sheet or not, will need to be tested for its material properties. The main property that will be used is the SMAs ER in both the austenitic and martensitic phase. These parameters will be used for actuation to tell when the transformation to austenite is complete, and also to set a baseline martensitic ER for the piezo-resistive sensing technique.

The stress-strain curve of the SMA will also be useful in understanding the materials loading characteristics. The loading can be conducted on a MTS Universal Testing Machine with a load cell and a LVDT. The moduli of the SMA can be tested in both the austenitic phase and martensitic phase. The strength of the material can be determined through this testing. If the SMA is to be thermally cycled, it is good to note that loading an SMA will increase its transition temperatures, these equivalent transition temperatures can be calculated from Equation 2.3.

AC.2.2 Pull-Force Test

This test is to characterize the axial pull force of the SMA wire and can be seen set up in Figure 3.13. Dynalloy provides a Table which includes Pull Force values for differing diameters of Flexinol, shown in Table 3.1, however these will still need to be tested in the case there are differences due to manufacturing. There are springs in the lab that have been used in previous works, however if a spring is to be ordered, many can be found on McMaster-Carr. The mount for this test can be any thickness of plywood, as long as there are screws that can fully pass through and be locked on the other end with a nut. The recommended thickness is 0.5 to 0.75 inches, as these can be easily found at a hardware store or on McMaster-Carr: https://www.mcmaster.com/plywood. The necessary screws, nuts, and alligator clips can be sourced from the lab. The screws can be any size as long as they fit through the plywood and allow enough space below to be locked with a nut and above to have the SMA wound around and locked with nuts. In order to measure the distance travelled, markings can be made directly on plywood using a pencil or a piece of paper can be mounted to the plywood prior to each actuation to mark the beginning and ending points of the spring.

AC.2.3 Angle Recovery Test

This test will be used to record the actuation ability of the SMA wires. Figure 3.15 shows a representation of the set-up that will be used for this test. The red end of the joint will be 3D printed to include a threaded hole on the X-Z plane so that it can be mounted onto a piece of plywood. A piece of paper with a printed protractor can be used to record the beginning state and end state for each test. Nominally at the start of the test the yellow end of the joint will be at a 45° and at the end of the test the yellow end will be at 90°. The marker must be placed at the NA of the X-Y plane cross-section. This can be achieved by either including a threaded hole on the X-Z plane of the yellow side of the joint, or directly 3D printing a feature on the joint.

In order to control this actuation, the ER of the SMA wires will have to be monitored during the heating process. Due to the 1% strain that is present in the deployed configuration, the 45° sweep should be completed before the SMA is fully austenitic. The current applied to the SMAs in lab testing will be controlled both through visual inspection and ER measurements. Once the joint is fully deployed or the ER of an SMA wire equals the measured ER of the austenitic phase, from the material property tests, the current can be shut off. If it is shown that the joint does not reach the fully deployed configuration before the austenitic ER is reached or the recovery stresses cause damages to the joint, then the pre-strain can then be altered by changing the ‘r’ value from the design introduced in Figure 3.6 and using the relationship represented in Figure 3.7.

AC.2.4 Torque Balance Test

This test has a very similar set-up to the Angle Recovery test, however it includes a force gauge and the tape spring strain energy member in the joint. In order to set-up the test shown in Figure 3.16, a 45° angle bracket must be used for mounting the force gauge. Using plywood and

existing 80/20 hardware in the lab, a mount can be created to hold the joint and force gauge at a fixed position. The size of the mount will depend on the force gauge that is being used.

If a force gauge cannot be sourced from the lab, alternatives can be found online from many manufacturers. Grainger force gauges can be found here: https://www.grainger.com/category/test-instruments/nonelectrical-properties-testing/force-gauges. McMaster-Carr force gauges can be found here: https://www.mcmaster.com/tension-gauges/measures~tension/. The force gauges will not require a high load capacity since the moment of the tape spring will appear as a diminished force at the end of the moment arm, which in the current design is ~100 mm from the hinge axis. The moment of the tape spring will be the measured force multiplied by the length of the moment arm. The addition of each SMA wire will reduce the apparent moment, and the incremental reduction will provide the moment added from each wire.

If the 80/20 components become unavailable, there are many alternatives for brackets that can create the desired 45° angle. The mount can be created using two pieces of plywood and 45° brackets such as these found at Amazon.com: https://www.amazon.com/Degree-Bracket-Connection-Aluminum-Profile/dp/B07FZ7KN12/ref=asc_df_B07FZ7KN12/?tag=bingshoppinga-20&linkCode=df0&hvadid=&hvpos=&hvnetw=o&hvrand=&hvpone=&hvptwo=&hvqmt=e&hvdev=c&hvdvcmdl=&hvlocint=&hvlocphy=&hvtargid=pla-4583863989065710&psc=1. McMaster-Carr also provides angled brackets available here: https://www.mcmaster.com/45-degree-brackets/.

The necessary eye bolt can be found in the lab, however eye bolts can also be easily found online such as at McMaster-Carr found here: https://www.mcmaster.com/eyebolts.

AC.2.5 Sensing Test

This test will require a hanging mount so that the joint can be configured as shown in Figure 3.17. This mount can be created using 80/20 hardware where the yellow end of the joint will require a threaded hole on the X-Z plane to attach a screw and 'T-nut' which is used to attach to the 80/20 hardware. A threaded hole on the yellow end will be used to attach an eye bolt on which the hanging weights will be loaded.

In the lab there is weight hanger and multiple 10 lb weights that can be used for this test. Since the first iterations of this test will be conducted using 3D printed plastic parts, the strength of the joint is currently unknown due to the print settings such as layer orientation and infill percentage. For future tests with stronger materials, larger weights may need to be bought, or the test can be conducted on a UTM with an LVDT and load cell. If more or heavier weights must be ordered, they can be bought from McMaster-Carr: https://www.mcmaster.com/hanging-weights.

AC.2.6 Further Testing

Once the above tests have been completed, the results will prompt further iterations of each test such as changing the mounting and pre-strain for the Angle Recovery test or using higher quality materials and heavier weights for the sensing test. The higher quality materials can be stronger plastics, which can be printed in the lab, or metals which can be 3D printed from outside sources such as https://www.xometry.com/ or https://www.protolabs.com/.

Throughout the testing process, the heating time will be recorded for each test to hone in on the optimal heating time for each specific SMA. Due to the variability of the wires from the heat treatment and composition differences, the self-sensing function of the SMA wires is required for position/temperature control during actuation/heating. Different methods of heating, as were discussed in Section 2.3.1, can be employed and tested to find the optimal heating

method. This will require some trial and error due to the variability of each wire, however monitoring the ER of the SMA during heating will provide a safety feature to prevent overheating while the heating method is perfected.

Another option for SMA integration into the truss modules is utilizing the pseudoelastic effect for higher sensitivity sensing and strain energy for deployment. After obtaining pseudoelastic SMAs from the aforementioned sources, the new SMAs can be used in two configurations. The first configuration solely uses pseudoelastic SMAs that would require launch locks to hold back the strain energy of the wires until actuation is necessary. After deployment, the SIM would revert to austenite and the wires would provide higher sensitivity sensing than martensitic SMA wires. The second configuration uses both the SME and the pseudoelastic effect, but requires two sets of wires. In this configuration the circuitry for both wires would be persistent rather than switching between actuator and sensor functionalities. This would require one set of SMA wires utilizing the SME for actuation and one set of pseudoelastic wires for sensing. This does create parasitic mass by fixing each set of wires to one particular function, however the benefits of using both the SME and pseudoelasiticty may outweigh the detriments of the low parasitic mass added by the SMA wires. The previously designed tests can be modified to test the pseudoelastic pull force, angle/strain recovery, and sensing capabilities.

The strain energy member that is currently being used for the SMATSH design is a steel tape spring, however a carbon composite coilable boom is being investigated for use by the aforementioned tri-truss trade study team. This lightweight carbon composite can be modified to use in this design as a substitution for the hinge joints. Due to the hollow interior, the SMAs can be mounted within the composite member to allow for internal actuation. These carbon

composites are specifically made at NASA LaRC and can be sourced by contacting Juan Fernandez or Julia Cline.

If both the actuation and sensing capabilities are validated on the hinge joint, then integration into the full truss can begin. This will start with the cubic truss, where the joint will be attached to the cubic truss node and the strut member that will be packaged. A special strut length setter will have to be made to account for the length added by the joint itself. The designer of the original length setter, John Teter, can be contacted for assistance with creating the new one.

After validation with the cubic truss hinge joint, integration into the tri-truss hinge joint will begin. Due to the slightly different geometry, it would be wise to conduct the validation experiments again as the mounting of the SMAs can change their behavior. The tri-truss has more complicated dynamics since the entire truss must be actuated at once rather than a single strut, this means that each joint must actuate at the same time or the truss may experience unwanted internal loads that could potentially damage the structure. Once each joint has been tested, the full tri-truss model will be built.

A space rated SMA integrated truss is the ultimate manufacturing goal of this project. Although this is far off in the development process, it would be helpful to identify the necessary materials for the LEO environment. The first step is finding an SMA whose transformation temperatures are in the operable range in space and can still provide recovery stress for actuation and piezo-resistive response for sensing. The full list of known SMAs found in the work of Zarinejad & Liu (2010) is a good starting point, however it may be necessary to outsource the creation of a custom SMA with the operating temperatures and recovery stresses pre-indicated for the manufacturer.